NANOCRYSTAL QUANTUM DOTS AS BUILDING BLOCKS FOR ARTIFICIAL SOLIDS AND THEIR APPLICATIONS IN OPTOELECTRONIC DEVICES

A Dissertation
Presented to the Faculty of the Graduate School
of Cornell University
In Partial Fulfillment of the Requirements for the Degree of
Doctor of Philosophy

by
Joshua Jongwoo Choi
August 2012

NANOCRYSTAL QUANTUM DOTS AS BULDING BLOCKS FOR ARTIFICIAL SOLIDS AND THEIR APPLICATIONS IN OPTOELECTRONIC DEVICES

Joshua Jongwoo Choi, Ph. D.
Cornell University 2012

Nanocrystal quantum dots exhibit size-dependent optoelectronic properties and provide intriguing scientific and technological opportunities. Most proposed technologies based nanocrystals depend on macroscopic functional assemblies of nanocrystals in which the nanocrystals interact with each other to give rise to new collective properties - also called as artificial solids. As in the analogous atomic crystals, the optoelectronic properties of artificial solids are governed by (1) the energy levels of nanocrystals, (2) electronic coupling between nanocrystals, and (3) the symmetry of the nanocrystal superlattice. These issues add many levels of complexity to the design of artificial solids and, for the successful development of nanocrystal based technologies, it is crucial to gain deep understanding on the structure-property relationship of nanocrystals on multiple length scales.

In this dissertation, I will present studies that show insights into the three governing factors of the optoelectronic properties of artificial solids mentioned above. (1) Nanocrystal energy levels: a direct correlation between interfacial energy level offsets between lead chalcogenide nanocrystals and ZnO layers with photovoltaic device performance is presented. Based on obtained insights on the size dependent photovoltaic properties of lead chalcogenide nanocrystals, first demonstration of solution processed nanocrystal tandem solar cells was achieved. (2) Inter-nanocrystal electronic coupling: rates of photogenerated exciton dissociation in nanocrystal assemblies as a function of inter-nanocrystal spacing are probed. The results show that excitons dissociate via tunneling induced delocalization among neighboring nanocrystals. Based on insights obtained from this work, drastically improved performance of solution processed nanocrystal infrared light emitting diodes is demonstrated. (3) Nanocrystal superlattice symmetry: interaction between ligand molecules on the surface of nanocrystals play critical roles in self-assembly process. Differences in the coverage of surface ligands bound to nanocrystals can be exploited to tune the shape of nanocrystal interaction potential during the self-assembly. Denser ligand coverage causes nanocrystals to interact as spheres and face-centered cubic structure is formed. In contrast, sparse ligand coverage amplifies the aspherical shape of the core crystallite and can cause non-close packed structures such as body-centered cubic.

BIOGRAPHICAL SKETCH

Joshua Jongwoo Choi was born in Seoul, Korea in 1982 and immigrated to the United States in 1998. For undergraduate education, he went to Cooper Union to study chemical engineering. During the undergraduate years, he became deeply fascinated by the concepts of nanotechnology. Upon obtaining his B.E. degree in 2006, despite the opportunity to work in an oil refinery, he chose to attend graduate school to gain deeper understanding in physics required to appreciate nanotechnology more as well as practical skills such as photolithography techniques to eventually get a job in the field of nanotechnology. (Cooper Union is a high quality institution but offered neither graduate level physics courses nor clean room facilities because it is a small-sized primarily undergraduate institution.) He went to Cornell University to study Engineering Physics and immensely enjoyed taking various advanced physics courses and a hands-on microelectronics fabrication course. After working on surface enhanced Raman scattering of organic molecules on nanoporous gold thin films under supervision of Prof. Christopher "Kit" Umbach, he obtained M.Eng. in 2007. Despite the options of working in the microelectronics industry, he again made the decision to stay in academia (turned out to be a very good choice!) - he remained at Cornell University to start in the Applied Physics Ph.D. program in 2007 under joint supervision of Prof. Tobias Hanrath and Prof. Frank Wise and has been studying properties of nanocrystal quantum dots and their applications in optoelectronic devices. He has immensely enjoyed the time at Cornell University and nanomaterials continue to fascinate him. He plans to stay in the research career path and continue making contributions.

Joshua is married to Ji Kim, an artist, whom he met at Cornell University and looks forward to expanding the family.

To my wife, parents and father-in-law for their love and support

ACKNOWLEDGMENTS

First and foremost, I thank my advisors Prof. Tobias Hanrath and Prof. Frank Wise for providing support, inspiration, guidance, deep insights and bigger perspectives on science throughout my graduate training. I especially thank Tobias for mentoring me in every aspect of what it means to become a scientist starting from just a curious student and his patient support throughout the years. The insights and perspectives Tobias and Frank have shared with me throughout my graduate training have become treasures for me and will continue to guide my scientific career. I also thank Prof. Christopher "Kit" Umbach for his guidance as a committee member.

I was extremely fortunate to work with superb senior graduate students and postdocs whom were happy to teach me and collaborate. I would like to give special thanks to Dr. Yee-Fun Lim whom has taught me how to proceed and persevere through the process of developing novel solar cell architectures. His insights and presence in the lab enabled me to march on when my first project was stuck for many weeks due to short-circuited devices. The picture Yee-Fun and I later took together at the hibachi place to celebrate the publication of that project always reminds me of his help. I would also like to thank Dr. Byung-Ryool (Yul) Hyun whom I could always count on to challenge whatever crazy research ideas I think of. His extensive experience on practical research issues, deep insights on science, curiosity and willingness to discuss all kinds of research ideas made him one of the people I seek first for discussion. I thank Dr. Adam Bartnik for showing me that the pedagogical, caring and extremely smart senior student that every junior student dreams of exists in reality.

I also thank my collaborators whom have made vital contributions to my projects and helped me to stretch my knowledge and experience. I give special thanks to Dr. Detlef Smilgies at CHESS whom has provided the world class X-ray scattering experiment

capabilities and scientific insights. I thank Dr. Jacek Jasieniak for his insights on nanoparticle synthesis and device physics. I thank Prof. Liangfeng Sun for the interesting and enjoyable collaboration we did on the nanocrystal LED project. I thank Dr. Justin Luria and Prof. John Marohn for providing their expertise on electric force microscopy. I thank Dr. Clive Bealing, Ananth Kaushik, Prof. Paulette Clancy and Prof. Richard Hennig for providing computational expertise. I thank Dr. Kevin Hughes and Prof. James Engstrom for providing XPS expertise. I thank Dr. Mitk'El Santiago-Berrios and Prof. Héctor Abruña for providing electrochemistry expertise.

I would like to thank the junior graduate students and undergraduate students whom I have worked with and learned much from - Kaifu Bian, William Baumgardner, Kevin Witham, David Stachnik, Jun Yang, Dave Moore, Mathew Oh, Rachel Hoffman and Whitney Wenger. I thank Kaifu for all the hardcore and yet fun CHESS shifts he has done with me. I also give special thanks to Rachel and Whitney for allowing me the privilege of working with top-notch undergraduate students as themselves.

Beyond the professional interactions, I thank Simon Lefrancois and Dr. Yee-Fun Lim for their friendship and support. All the good food, drinks, talks, work-outs, conspiracy theories, political discussions, hiking trips, trips to great places like NYC, Boston, Toronto, Montreal, San Francisco and Hawaii I shared with them have rejuvenated and sustained me through the graduate school years.

Finally, I dedicate this dissertation to my wife, parents and father-in-law whose support has made all this possible. I am especially indebted to my wife whose presence, love, support and encouragement have sustained me through the ups and downs of going through the Ph.D. program. I am forever grateful to her.

TABLE OF CONTENT

CHAPTER 1

INTRODUCTION

1.1 Definition of Nanocrystal Quantum Dots

Nanocrystal quantum dots (NQDs) are semiconductor crystals with the size on the order of the Bohr radius of the exciton, typically few to tens of nanometers, that exhibit properties that depend on the size of NQDs. One example of the size dependent properties of NQDs is the tunable energy gap - the energy gap of the NQDs can be tuned throughout the IR and visible wavelengths simply by changing the NQD size (Figure 1.1). To understand the size dependent optoelectronic properties of NQDs, we will have to put the size of NQDs in perspective with respect to other well-understood material systems such as molecules and macroscopically sized crystals. Considering the typical size of the unit cell in semiconductor crystals, a NQD has only about 10 unit cells across its diameter and a few hundred to a few thousand atoms in its volume. In such a regime, it becomes unclear whether to classify NQDs as molecules or crystals – unlike molecules, adding or subtracting a single atom from NQDs does not significantly change their properties and, unlike in macroscopic crystals, their energy levels are discrete with optical transitions that follow molecule-like selection rules [1, 2]. Indeed, NQDs can be considered to be an intermediate between molecules and crystals, borrowing characteristics from both sides. Both views of approaching NQDs as larges molecules and small crystals are useful for understanding the size dependent optoelectronic properties of NQD and will be discussed in next section.

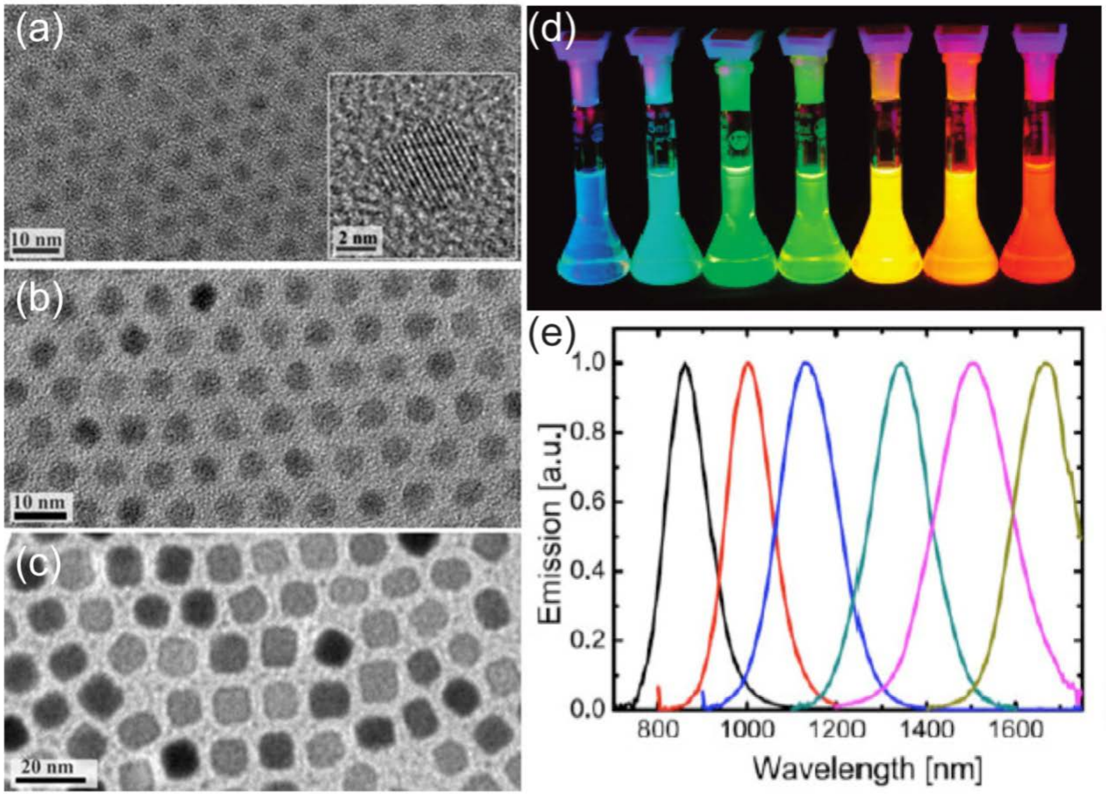

Figure 1.1: Size tunability of NQDs (a)-(c) Transmission electron microscope (TEM) images of size tuned PbSe NQDs. Size dependent photoluminescence wavelength from (d) CdSe/ZnS core-shell NQDs (Adapted from ref. [3] Copyright 2010 American Chemical Society) and (e) PbSe NQDs.

1.2 Origin of Size Dependent Optoelectronic Properties of NQDs

1.2.1 NQDs as Large Molecules: “Bottom-up” Approach

Looking at NQDs as large molecules to understand size dependent optoelectronic properties is often called as 'bottom-up' approach because the electronic structure of the NQDs are constructed by combining the atomic orbitals of constituent atoms. This approach is based on the Linear-Combination-of-Atomic-Orbitals (LCAO) method in chemistry or tight-binding model in solid state physics and provides both qualitative and quantitative understanding on size dependent electronic structure of NQDs.

Using the LCAO method, the overall orbitals of the molecule can be constructed starting from individual atomic orbitals. (Figure 1.2) Consider the simplest case of a molecule formed by two atoms. The valence atomic orbital of one of the atoms will combine with the valence atomic orbital of the other atom to form a bonding orbital and an anti-bonding orbital, forming the highest occupied molecular orbital (HOMO) and lowest unoccupied molecular orbital (LUMO) of the molecule respectively. The number of molecular orbitals formed due to the combination of the atomic orbitals will be the same as the total number of atomic orbitals combined and the degree of separation in energy between the bonding and the anti-bonding orbitals will depend on the strength of coupling between the atoms. Now imagine coupling three or more atoms to form a larger molecule where the combination of higher number of atomic orbitals will result in higher number of molecular orbitals that are placed closer to each other in energy. Continuation of this process will result in ‘energy bands’ of macroscopic crystals where molecular energy levels that are so close in energy to be distinguished experimentally. NQDs are in the intermediate regime between the molecule and macroscopic crystal cases where there are discrete energy levels near the energy gaps and addition or subtraction of more than few tens of atoms result in significant changes in their electronic structure.

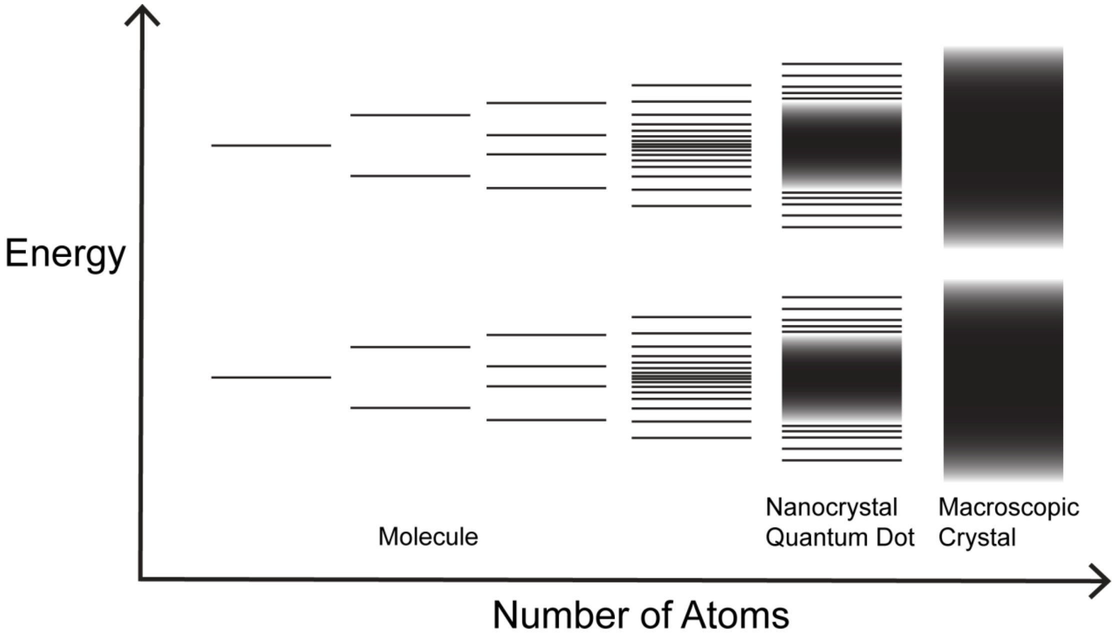

Figure 1.2: NQDs as large molecules based on the Linear-Combination-of-Atomic-Orbitals method. Molecules with small number of atoms show discrete energy levels. As the number of coupled atoms increase, energy levels become more densely packed, eventually forming bands in macroscopic crystals. NQDs are intermediate between these two extreme cases and show discrete energy levels near the energy gap whose locations in energy depend on the NQD size.

With this picture, we can now appreciate the origin of the size dependent optoelectronic properties of NQDs - subtraction of atoms, or reduction in NQD size, will increase the energy gap of NQDs and narrow the density of states into discrete states. Beyond providing the qualitative understanding, the molecular picture of NQDs is powerful in the sense that it can give highly accurate quantitative information on various aspects relevant to optoelectronic properties of NQDs such as detailed energy level locations, density of states and oscillator strength of optical transitions. However, calculations that involve hundreds and thousands of coupled atoms require large computing power [4, 5].

1.2.2 NQDs as small crystals: “Top-down” Approach

Similar to the molecular view of NQDs, approaching NQDs as small crystals with 'top-down' perspective can give both qualitative understanding and quantitative information on optoelectronic properties of NQDs. This approach is based largely on three approximations - nearly free electron, effective mass approximation and 'envelope functions' originating from infinite potential well boundary conditions.

For the nearly free electron model with infinite periodic potentials, which describes macroscopically sized crystals, the Hamiltonian is:

$$H = -\frac{\hbar}{2m}\nabla^2 + \mathrm{V}(\mathbf{r}) \qquad (1.1)$$

where V(**r**) is the periodic potential over the lattice constant of the crystal and thus V(**r**) = V(**r**+**R**) for all lattice vectors **R**. The periodic condition implies that the wavefuntions $\psi(\mathbf{r})$ and $\psi(\mathbf{r}+\mathbf{R})$ should only have the phase difference and they can be chosen to have the form of a plane wave multiplied by a function with the periodicity of the lattice (the Bloch theorem):

$$\psi_{\boldsymbol{k}}(r) = e^{i\boldsymbol{k}\cdot\boldsymbol{r}} u_{\boldsymbol{k}}(\boldsymbol{r}) \tag{1.2}$$

The plane wave term, $e^{i\boldsymbol{k}\cdot\boldsymbol{r}}$, represents the phase of the wavefunction while $u_{\boldsymbol{k}}(\boldsymbol{r})$ describes the response of the electron to the periodic potential of the lattice. These wavefunctions are called the Bloch wavefunctions and can successfully describe the electronic structure of the macroscopic crystals including the band gaps. The effective mass approximation is then used to simplify the Hamiltonian by including the effect of periodic potential into the effective mass tensor, m^*. The effective mass can be obtained from the curvature of the band structure near the band edge and contains information on how the electron will response to an external force in the periodic potential landscape. The effective mass approximation renders the Hamiltonian to be in the same mathematical form with the free electron with eigenfunctions that I define as 'envelope function', $\psi_{env}(\boldsymbol{r})$, with reasons that will be apparent shortly later.

$$H\psi_{env}(\boldsymbol{r}) = -\frac{\hbar}{2m^*}\nabla^2\psi_{env}(\boldsymbol{r}) \tag{1.3}$$

With the simplified Hamiltonian, I will account for the small size of NQDs and the confinement of the electron within the NQDs by imposing boundary conditions of infinite potential well such that the envelope wavefunctions vanish at the boundary. Thus, the envelope functions are simply the solutions to the particle in an infinite potential well problem. Notably, the solution for the total wavefunction in the NQD is akin to replacing the phase term of the Bloch wavefunction that describes an infinite sinusoidal wave with an envelope function term which describes a localized wave packet:

$$\psi_{total}(r) = \psi_{env}(\boldsymbol{r})u_{\boldsymbol{k0}}(\boldsymbol{r}) \tag{1.4}$$

Where **k0** is at the band extremum where the effective mass approximation is taken. In the case of NQDs that typically have quasi-spherical shape, the spherical infinite potential barrier boundary condition is employed and the eigenfunctions can be described as the product of spherical harmonics, $Y_l^m(\theta, \phi)$, and radial Bessel function, $R(r)$:

$$\psi_{env}(\boldsymbol{r}) = Y_l^m(\theta, \phi)R(r) \tag{1.5}$$

and as with any quantum confined wavefunctions, discrete energy levels arise and the energy levels that correspond to wavefunctions with larger number of nodes will be at higher energy. Thus, in this case of the spherical infinite well with diameter D, the energy levels of the envelope functions (confinement energy) are found by identifying the roots of the radial Bessel function, $\chi_{n,l}$, where n is the principal quantum number and the l is the azimuthal quantum number:

$$E_{n,l} = \frac{2\hbar^2\chi_{n,l}^2}{m^*D^2} \tag{1.6}$$

First of all, we can now see where the size tunable energy gap of NQDs originates from - as the diameter of the NQD gets smaller, the confinement energy will be larger with $1/D^2$ dependence and the energy levels will be more separated. Moreover, we can appreciate why NQDs are often referred to as 'artificial atoms' - the azimuthal quantum numbers, l = 0, 1, 2, 3, is also expressed as S, P, D, F respectively and due to the atomic like envelope wavefunctions and, for example, the envelope wavefunction with the lowest energy level from the first root, $\chi_{1,0}$ (n = 1, l = 0), has the symmetry of the 1S orbital in the hydrogen atom. (Figure 1.3)

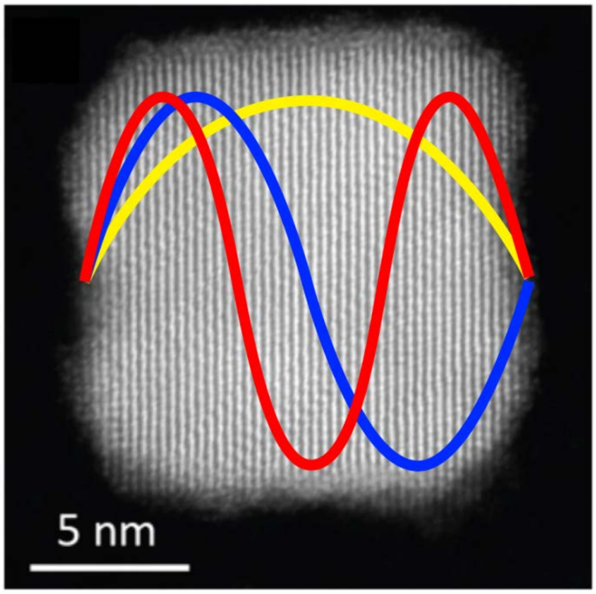

Figure 1.3: Colored lines representing one dimensional envelope wavefunctions (yellow = S, blue = P, red = D) overlaid on top of high resolution TEM of a PbSe NQD. (Image credit: W. Baumgardner and L. Fitting-Kourloutis, unpublished results)

The envelope function theory (also called as $\boldsymbol{k} \cdot \boldsymbol{p}$ theory) is based on this ‘top-down’ approach and has been surprisingly successful in quantitatively predicting electronic structure and optical properties of NQDs despite its simplicity of calculation compared to ‘bottom-up’ approached and the unrealistic assumption of infinite potential well at the boundary of NQD [6].

The goal of this section was to provide a basic and intuitive picture of the origin of size dependent energy gap of NQDs and has focused on the spatial confinement energy only. However, to fully account for experimentally observed size dependent energy gap of NQDs, other effects such as Coulomb interaction energy between electron and hole and the 'dielectric confinement energy' caused by contrast in dielectric constant between the NQD and the surrounding need to be considered [2]. These issues will be discussed more in detail in section 1.5.1 along with various experimental methods that can determine the energy level locations of NQDs as a function of the NQD size.

1.3 Experimental realization of NQDs

I will now briefly discuss how real NQD systems are experimentally prepared. Research on the controlled synthesis of NQDs in laboratory settings has been ongoing since 1970s. Initial progress came from the high vacuum techniques such as molecular beam epitaxy [7, 8] or embedding NQDs in solid hosts such as glass [9, 10] but the impact of these methods on the NQD research field was limited due to several restrictions such as necessary fixation of NQDs on specific substrate or host materials and complex experimental set-ups with high cost and low through-put. In 1993, a ground-breaking paper on the synthesis of II-VI NQDs based on simple wet-chemistry from organometallic precursors – so called ‘hot-injection method’ - enabled an explosive expansion in research activities on NQDs [11]. The ‘hot-injection method’ allows robust, simple, low-cost and scalable synthesis of NQDs with high degree of control over the size of NQDs. The TEM images of NQDs synthesized through the hot-injection method (Figure 1.1 and Figure 1.3) show good monodispersity and size-tunability. During the subsequent two decades, further advancement on the hot-injection method have resulted in application of the method for wider array of compositions (II-VI, IV-VI and III-V systems) and exquisite shape control (tetrapods, rings, rods, sheets and etc) of NQDs [12-19].

All of the studies discussed in this thesis used quasi-spherical lead salt (IV-VI) NQDs prepared through the hot-injection method and a brief explanation on how the hot-injection method works in synthesizing NQDs is needed here. The hot-injection synthesis is based on the classical La Mer and Dinegar's studies [20] on colloidal particle nucleation and growth in which quick burst of nucleation events are temporally separated by controlled growth of the nuclei. (Figure 1.4) The reaction is initiated by quick injection of cold solution of precursors into a hot solvent in the presence of surfactant ligand molecules (typically long alkyl chain molecules such as oleic acid). The injection then causes a cascade of events - (1) thermal decomposition of precursor reagents and rapid increase in concentration of "monomer" accompanied by a sudden drop in reaction temperature to the point of supersaturation of monomers, (2) a quick burst of nucleation events that cause the monomer concentrations to drop below the saturation point, (3) growth of the nuclei into NQDs by attachment of remaining monomers or through Ostwald ripening process in which the smaller NQDs dissolve due to their higher surface energy and gets absorbed into bigger NQDs [21] (4) quenching of the reaction either by depletion of monomers and end of ripening process or kinetically stopping the reaction by dropping the reaction solution temperature.

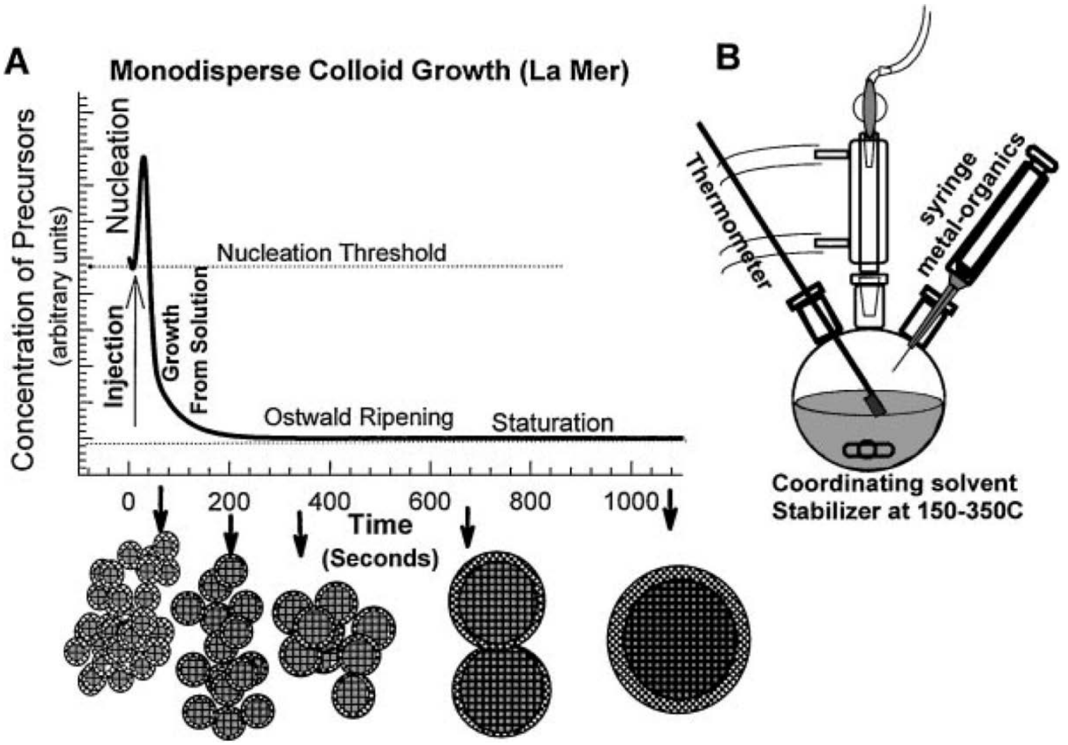

Figure 1.4: Hot-injection synthesis method of colloidal NQDs. (A) Concentration of precursor profile illustrates the nucleation and growth steps of NQDs. (B) Schematic of hot-injection synthesis method apparatus. (Adapted from ref. [22] Copyright 2000 Annual Reviews)

The resultant NQDs typically have quasi-spherical shaped crystal with nanoscale facets surrounded by the surfactant ligand molecules. A cartoon of a PbS NQD with oleic acid surface ligand molecules are shown in Figure 1.5 as an example. The ligand molecules play crucial role in colloidal stabilization and maintenance of the nanoscale size of NQDs in solution by providing steric repulsion that blocks van der Waals attraction between the crystal cores from causing the NQDs to aggregate. Also, the ligand molecules lower the surface energy of the NQDs and passivate surface dangling bonds that may behave as charge trap states. Therefore, they play critical roles in determining the shape, size and optoelectronic properties of NQDs. The control over the size and shape of NQDs using the hot-injection method can be achieved by tuning the concentrations of precursors and ligand molecules as well as the reaction temperature. Experimental details on exact procedure for synthesis of lead salt NQDs used for studies in this thesis are given in chapter 2.

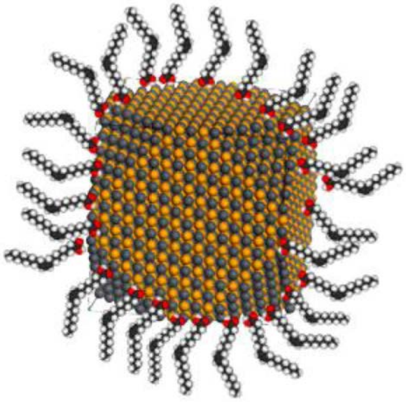

Figure 1.5: A cartoon of lead salt NQDs with oleic acid surface ligand molecules. The dark gray balls stand for lead atoms and orange balls stand for either sulfur, selenium or tellurium atoms. In this cartoon, the lead salt NQDs are taken to have the cuboctahedron shape with six (100) faces and eight (111) nanoscale facets. (Image credit: T. Hanrath)

1.4 Potential Applications of NQDs

Now that we are familiar to a certain extent with the origin of size dependent optoelectronic properties of NQDs and how real NQDs systems can be prepared with simple, robust and high-throughput fashion, I will discuss the possible technological applications of NQDs in this section. As technological materials, NQDs have garnered intense interests due to several reasons – (1) the tunable energy gap of NQDs that covers the range of infrared to visible wavelengths provides intriguing opportunities for optoelectronics and telecommunication applications. (2) Low-cost, high-throughput and low-temperature synthesis and thin film processing methods allow roll-to-roll fabrication of devices that can enable economically-viable wide-spread deployment of the NQD thin film devices. (3) Novel phenomena that occur in NQDs due to quantum confinement such as enhanced multiple exciton generation [23], phonon bottleneck [24] and narrowing of density of states provide unique opportunities for NQDs as high performance materials for various applications. These reasons render NQDs as potentially transformative next generation materials for various technologies such as solar cells [25-32], light emitting devices (LEDs) [33-36], photodetectors [37-39], field effect transistors [40], thermoelectric [41], and fluorescent biomarkers [42] and world-wide active research efforts focused on realization of these applications are currently underway. In this thesis, I present fabrication and characterization of novel NQD solar cell and LED devices and, in next section, I will discuss physical and electronic aspects of NQD thin films relevant for the device applications.

1.4.1 Basic principles of solar cells

The solar cell application of NQD is one of the main topics in studies reported in this dissertation and the basic principles of solar cells and metrics for device performance evaluation is briefly discussed in this sub-section. In short, solar cells are the devices that converts photon energy into electricity by separating the photogenerated electron and holes into external circuit (the photovoltaic effect). To achieve the charge separation, the solar cell device must have built-in asymmetry that drives electron and hole into different directions. The asymmetry for the charges can be introduced by creating interfaces of different material combinations such as n-type/p-type semiconductors and semiconductor/metal. Electrically, the asymmetry manifests itself by the rectification behavior of a diode - current through the device is allowed only in one direction after a certain threshold voltage (in an ideal diode). In a real diode device, the current density versus voltage curve, also called as J-V curve, typically looks like the black line in Figure 1.6 (taken from actual NQD solar cell device).

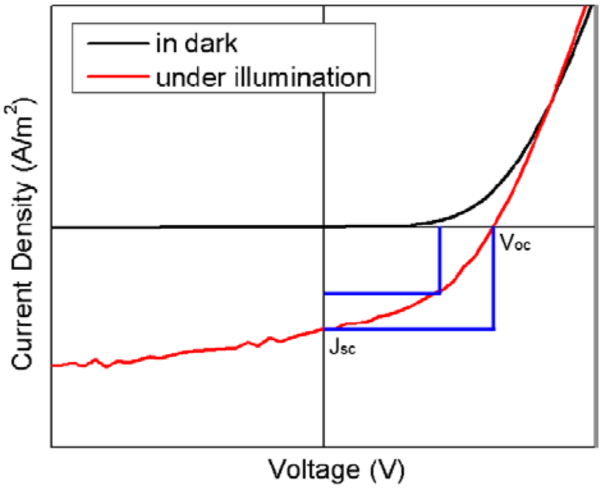

Figure 1.6: J-V curves of NQD solar cell in dark (black) and under light illumination (red).

A solar cell relies on this asymmetry and electrical rectification behavior to achieve the separation of photogenerated electrons and holes. Thus, without light illumination, the solar cell behaves simply as a diode (the black line in Figure 1.6) and, under light illumination, the photovoltaic effect produces the additional current from the photogenerated charges (photocurrent) and shifts the J-V curve of the diode (the red line in Figure 1.6). Thus, solar cells under illumination produces non-zero current density at zero bias due to the photocurrent - the current density from the device at bias zero is called as the "short circuit current", J_{sc}. To produce power, which is the product of voltage and current, voltage also needs to be considered - power production will occur only when the solar cell is operating in the fourth quadrant. The J-V curve shown in Figure 1.6 illustrates, as voltage across the device is increased, solar cells will eventually produce less current density to the point that it will become zero at a certain voltage called the "open circuit voltage", V_{OC}. In an ideal case, the reduction in the current density will occur in an infinitely abrupt fashion such that the maximum power is equal to the area of the rectangle created by vertical and horizontal lines that cross the V_{oc} and J_{sc} (the bigger rectangle in Figure 1.6). However, in actual an device, the reduction in current density occurs more gradually and the maximum attainable power (the area under the small rectangle in Figure 1.6) is always smaller than the ideal case. The point in the J-V curve that produces the largest area rectangle is called the maximum power point and the ratio between the rectangular area formed by this point versus the rectangular area for the ideal case is defined as the 'fill factor', FF. The fill factor thus indicates the 'idealness' of the solar cell and is affected by various carrier recombination processes in the device.

The three factors, J_{sc}, V_{oc} and FF, defined above are the key parameters used for characterizing the performance of the solar cell. The power conversion efficiency (η) of the solar cell is defined to be the maximum fraction of incident optical power converted into electrical power and is expressed as:

$$\eta = \frac{J_{sc}V_{oc}FF}{P_{optical}} \tag{1.7}$$

where $P_{optical}$ is the incident optical power. Thus, the goal of solar cell research and engineering is to increase J_{sc}, V_{oc} and FF of the solar cell through improvement in materials and device structure.

1.5 NQDs Artificial Solids: Energy levels, Electronic Coupling and Self-

assembled Structures

Most proposed NQD-based technologies discussed in the previous section depend on functional assemblies in which the constituent NQDs interact with each other and macroscopic external contacts. The properties of NQD assemblies depend not only on the properties of the individual NQDs but also on the properties arising from interactions between the NQDs in the assembly. Thus, it is crucial to understand, and ultimately control, the collective optoelectronic properties of NQD assemblies arising from electronic interaction among NQDs for successful development of NQD optoelectronic device applications. In contrast to the rapidly growing knowledge base on the optoelectronic properties of individual NQDs as function of their composition, size and shape, the understanding on the structure-property relationship in NQD assemblies is far less developed and currently is the knowledge frontier of the NQD field with potentially huge scientific and technological impact.

NQDs assemblies can be regarded as ‘artificial solids’ composed of NQD ‘artificial atoms’ because of their tunable properties [43-47]. Analogous to atomic crystals that I discussed in section 1.2.1, the electronic structure of NQD assemblies can be constructed using LCAO method by combining orbitals of individual NQDs. Thus the energy level locations, the degree of electronic coupling and the geometry of the coupling direction between the orbitals will critically influence the resultant electronic structure of NQD assemblies. Therefore the three major factors that govern collective optoelectronic properties of NQD assemblies are (1) NQD energy levels, (2) electronic coupling between NQDs and (3) the symmetry of the assembly structure. In this thesis, studies related to the effect of all three factors are presented and background information will be presented in this section.

1.5.1 NQD Artificial Solids: Energy Levels

As discussed in section 1.2, due to the atom-like discrete energy levels of NQDs that are tunable by simply changing the size, NQDs are sometimes called as 'artificial atoms.' Knowing the location of energy levels of NQDs with respective to the vacuum energy, also called as 'absolute energy levels', is critically important for science and technological application of NQDs - the optoelectronic properties of the NQD assemblies will strongly depend on the locations and offset of energy levels in constituent individual NQDs. Moreover, the energetic offset between the energy levels of NQDs and other materials such as another NQD, molecules, polymers and metal oxides serves as the driving force, $-\Delta G$, for the electron transfer reaction [48]. Therefore, to rationally design devices such as solar cells that require asymmetric direction of charge transfer, well-characterized absolute energy level locations of NQDs are essential.

There are several experimental methods to measure the absolute energy levels of NQDs - cyclic voltammetry (CV) [49-52], ultraviolet photoelectron spectroscopy (UPS) [33] and X-ray absorption spectroscopy (XAS) [53]. CV is an electrochemical method that employs three electrodes - working, reference and counter electrodes - and solution with electrolytes. The NQDs are either dissolved in the solution or deposited as a thin film on the surface of the working electrode. During measurements, voltage across the working electrode and the reference electrode is swept while current is being detected - the counter electrode serves as the current dump to block high current at the working electrode surface that may give inaccurate measurements. As the NQDs get reduced and oxidized by injection/extraction of electron into their energy levels, a peak in current will be detected. The voltages at which the peaks are detected are then recorded and are converted to absolute energy level locations based on calibration of the experimental set-up with a robust and well-known standard redox couple. In this thesis, CV is employed to measure the absolute energy levels of PbSe NQDs and the detailed experimental procedures will be provided in chapter 3. UPS relies on photoelectric effect by detecting kinetic energy spectra of electrons ejected from NQDs by ultraviolet photons. Thus, UPS can map out the valence band structure of NQDs. Complimentary to UPS, XAS can map out conduction band structure by using synchrotron based X-ray photons to directly probe vacant states [53].

The valence and conduction band edges, or HOMO-LUMO levels in case of NQDs, measured by above mentioned three methods correspond to ionization energy (IE) and electron affinity (EA) of the material. The gap in energy between IE and EA is called as 'transport gap', E_{trans}, because the electrical transport of charges in the material occur through the states with these energy levels. As explained in section 1.2, the energy gap of NQDs can be tuned by changing the amount of extra kinetic energy arising from the quantum confinement effect - $E_e^{quantum}$ and $E_h^{quantum}$ for electron and hole respectively. To fully account for experimentally measured size dependent energy gap of NQDs, various Coulomb interaction energies need to be considered in addition to the quantum confinement energy. The types of Coulomb interactions to be considered will depend on types of experimental measurements. For example, in experimental methods such as CV, the NQDs are charged through injection/extraction of an electron and the Coulomb interaction between the charge and the image charge due to polarization of the surrounding needs to be considered. For a charge residing in the higher dielectric constant region, the interaction of the charge with its image charge is repulsive. Usually the NQDs have higher dielectric constant than their surrounding and therefore additional confinement energy is resulted for the charge in NQDs. I will define this energy the 'dielectric confinement energy' with notations $E_e^{dielectric}$and $E_h^{dielectric}$ for electrons and holes respectively. Thus, by accounting for both the quantum and dielectric confinement effects, the transport gap of NQD, E_{trans}^{NQD} , can be considered as [54]:

$$E_{trans}^{NQD} = E_{trans}^{bulk} + E_e^{quantum} + E_h^{quantum} + E_e^{dielectric} + E_h^{dielectric} \qquad (1.8)$$

where E_{trans}^{bulk} is the transport gap of the bulk material.

It should be noted that all CV, UPS and XAS methods need careful experimental designs - different results can be obtained depending on the choice of electrode, solvent, electrolytes, substrates and etc. Moreover, all three methods can be time-consuming. Thus, another approach is often taken to obtain information on the HOMO-LUMO energy level locations of NQDs - starting from 'optical energy gap', $E_{optical}^{NQD}$, measured with absorption spectroscopy and theoretically approximation can give the absolute HOMO-LUMO energy level locations [2, 55]. This approach is much easier and faster due to the simplicity and robustness of absorption spectroscopy but the drawback is that approximation is needed to account for the difference between the optical gap, $E_{optical}^{NQD}$, and the transport gap, E_{trans}^{NQD}. The optical gap is coined the term because it is measured by absorption spectroscopy where a photon is absorbed to create a electron-hole pair (exciton) in the NQD. Compared to the case of the NQD injected with a charge, the presence of both the electron and hole in optically excited NQD gives rise to additional Coulomb interaction energies - direct Coulomb interaction between the electron-hole pair, $E_{e,h}^{direct}$ and interaction between one charge and the image charge of the other charge due to the dielectric contrast between NQD and the surrounding, $E_{e,h}^{dielectric}$. Thus the transport gap can be expressed in terms of optical gap by accounting for these two interactions:

$$E_{trans}^{NQD} = E_{optical}^{NQD} + E_{e,h}^{direct} + E_{e,h}^{dielectric} \tag{1.9}$$

To approximate the $E_{e,h}^{direct}$and $E_{e,h}^{dielectric}$ in NQDs as a function the NQD size, theoretical approach based on effective mass approximation has been developed [2, 55]:

$$E_{trans}^{NQD} = E_{optical}^{NQD} + 1.786\frac{e^2}{4\pi\varepsilon_{NQD}\varepsilon_0 R} + \frac{e^2}{4\pi\varepsilon_0 R}\left(\frac{1}{\varepsilon_{sur}} - \frac{1}{\varepsilon_{NQD}}\right) \tag{1.10}$$

where e is the elementary charge (C), $\varepsilon_{\mathrm{NQD}}$ is the dielectric constant of the NQD, ε_0 is the vacuum permittivity (F/m) and $\varepsilon_{\mathrm{sur}}$ is the dielectric constant of the surrounding of NQD. This method has been employed successfully in several studies and will be used in the studies reported in this thesis [29, 56].

1.5.2 NQD Artificial Solids: Electronic Coupling

Analogous to atomic molecules where mixing of atomic orbital results in bonding and anti-bonding orbitals, electronic coupling between NQDs will result in delocalized orbitals for the collection of NQDs. Unlike bonds in atomic molecules that have fixed bond distance and strength, the degree of inter-NQD coupling can be tuned, opening up the possibility of manipulating optoelectronic properties of NQD 'molecules' and assemblies. By modeling NQDs assemblies as finite potential wells and using the Wentzel-Kramers-Brillouin (WKB) approximation, one finds that the coupling energy, $\mathrm{E_{coupling}}$, between the wavefunctions describes overlaps between exponentially decaying wavefunctions under a potential barrier [57]:

$$\mathrm{E_{coupling}} \approx \exp\left(-2\frac{\sqrt{2\mathrm{m}^{*}\Delta\mathrm{E}}}{\hbar}\Delta\mathrm{x}\right) \tag{1.11}$$

Where m^{*} is the electron effective mass in the surrounding of NQDs, ΔE is the potential barrier height and Δx is the edge-to-edge distance between NQDs. This indicates that the inter-NQD coupling strength will increase exponentially with decrease in the distance between NQDs and square root of the effective mass and potential barrier height. Therefore, unlike the bonds in atomic molecules that have fixed bond length and strength, the 'artificial bonds' in NQD molecules and assemblies can be tuned by manipulating the medium between the NQDs.

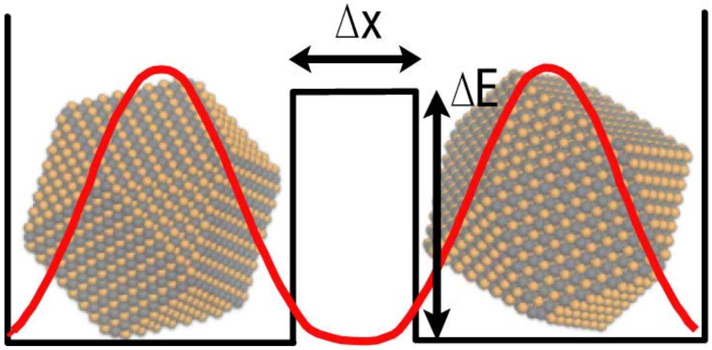

Figure 1.7: An illustration of electronic coupling between NQDs modeled by double finite potential wells. The tunneling induced overlap between wavefunctions gives rise to the coupling.

Within this context, the NQD community has made significant progress on reducing the distance and height of the potential barrier with goals of achieving strong inter-NQD electronic coupling required for device applications. Much of the progress came through utilization of short molecules as spacers between NQDs. In early pioneering studies, exchanging trioctylphosphine oxide ligands on the surface of CdSe NQDs with 1,4-phenylenediamine was found to increase the conductivity of the NQD assembly by 1000-fold [58]. Similarly, treating PbS NQDs, with oleic acid as original surface ligands, with hydrazine molecules have shown to decrease inter-NQD surface-to-surface spacing from 1.1 nm to 0.3 nm and thus greatly increase the electronic coupling between the NQDs [40]. As a result, along with other effects such as lowering the charging energy and doping the NQD array, the conductance through the

NQD array was increased 10 orders of magnitude and high mobility of 2 $cm^2 V^{-1} s^{-1}$ was achieved. Subsequently, a variety of short organic bridge molecules such as ethanedithiol [28, 59-61], benzenedithiol [27] and mercaptopropionic acid [62, 63] and many others have been employed to enhance the performance of NQD solar cells, LEDs, photodetectors and FETs. Recently, a new paradigm of using inorganic spacers has been introduced - employing molecular metal chalcogenide complex bridges [64], which lower both the potential barrier height and the distance. This research direction has resulted in mobility as high as 16 $cm^2 V^{-1} s^{-1}$ in $In_2Se_4^{2-}$ passivated CdSe NQD thin films [65]. Other short inorganic bridges such as anions [66], atoms [32, 67] and thiocyanate [68, 69] also have been introduced and show much promise. In chapter 5 and 6 of this thesis, studies that illustrate the critical role of inter-NQD spacing on excited state dynamics in NQD assemblies and NQD light-emitting diode device performance will be presented.

1.5.3 NQD Artificial Solids: Self-assembled Structures

As the electronic structure of atomic crystals depend on the symmetry and crystallographic direction of the lattice, the structure of NQD assemblies will influence how the ortbitals of individual NQDs couple with each other. Unlike atomic crystals that have fixed lattice symmetry at given temperature and pressure, the structure of NQD assemblies can be manipulated by utilizing entropic, electrostatic, van der Waals and magnetic forces during self-assembly [70-73]. Therefore, NQD assemblies can be considered as 'artificial solids' with tunable structures that give rise to properties that depend on the symmetry of the assemblies. Controlling and characterizing the structure of the NQD assembly is thus crucial in gaining fundamental insights into tunable collective properties of the NQD ensemble as well as a critical requirement for the development of NQD based technologies.

Challenges to building the foundational understanding of mechanisms governing NQD assembly formation arise primarily from the inherent complexity of the self-assembly process. Various interactions between the NCs, the surface-bound ligands and the surrounding solvent need to be considered [70-73]. In studies presented in this thesis, I show the significance of a molecular-level understanding of the role of ligand-ligand and ligand-solvent interactions in the NQD self-assembly process - NQD superlattice self-assembly resides naturally at the intersection of molecular crystal growth and the assembly of micrometer-sized colloids and various interactions of ligands have major influence during the NQD assembly process. To characterize the structure of NQD assemblies, which have a few nanometer scale spacings, I employed X-ray scattering techniques and introduction on the structural characterization of materials with X-ray is needed here.

The oscillating electric field of the incident X-ray waves will accelerate the electrons within the atoms in the sample. The accelerated charges will then emit radiation at the same frequency as the incident X-ray waves – in other words, the X-ray waves are elastically scattered by the electrons in the sample. The scattering by the protons in the atomic nuclei can safely be ignored due to their heavy mass compared to electrons and thus small intensity of scattered wave. In crystal lattices where the atoms are placed in a periodic fashion, the scattered waves can either constructively or destructively interfere with each other. To describe the interference between scattered X-ray waves, the atoms in periodic lattice can be thought to be residing on the sets of parallel planes (lattice planes) separated by distance, d, that the X-ray waves are reflected from. The waves will constructively interfere with each other when the path length difference between the waves reflected from different planes is integer multiples of the wavelength and thus the waves are in phase. The Bragg's Law describes this condition:

$$n\lambda = 2d\sin\theta \tag{1.12}$$

where n is an integer, λ is the wavelength of the incident X-ray and θ is the angle between the incident ray and the scattering plane. With a fixed wavelength for the incident X-ray, when spacing between the lattice planes and the orientation of the crystal satisfy the Bragg condition, the scattered X-ray will produce peaks with strong intensities (Bragg peaks) at various angles with respect to the direction of the incident wave. (Figure 1.8) The locations of the Bragg peaks at the detector therefore reflect, with a known detector-to-sample distance, the spacing between the lattice planes and their orientations with respect to the incident beam. Moreover, the collection of Bragg peaks from different sets of lattice planes with different orientations will reveal the symmetry of the crystal lattice structure. Therefore, by analyzing the scattered beam locations and intensities, the crystal structure such as the symmetry of the lattice, spacing between lattice planes and the orientation of the crystal with respect to the incident beam can be characterized.

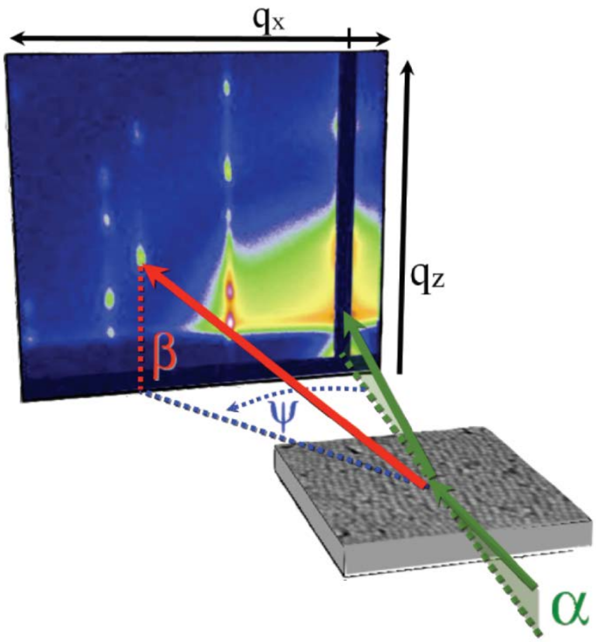

Figure 1.8: Experimental configuration of grazing incidence small-angle X-ray scattering. The thin film sample on a substrate is placed at a known distance from a two-dimensional X-ray detector. The α, β, ψ are incident, in-plane and exit angles respectively. (from ref. [74] Copyright 2009 American Chemical Society)

Among various X-ray scattering techniques, grazing-incidence small-angle X-ray scattering (GISAXS) has emerged as a powerful tool for the structural characterization of nanostructured thin films [74, 75]. GISAXS reveals not only the symmetry of the nanostructures but also their orientational ordering with respect to the substrate. In the structural analysis of NQD thin films, well-defined GISAXS scattering peaks indicate NQD assemblies with specific orientations with respect to the substrate (Figure 1.8), while ring-like scattering features indicate random or polycrystalline orientation of the grains of NQD assemblies.[76-78] In addition to GISAXS, grazing incidence wide-angle X-ray scattering (GIWAXS) can be used to probe the atomic lattice symmetry, spacing and orientation within the NQD. Note that, according to the Bragg's Law, as the angle, θ, becomes larger with fixed wavelength, the probed spacing becomes smaller. With X-ray wavelength of ~1 Å, GISAXS detects scattered peaks at angle around ~1 degree and thus probes ~5 nm distances that correspond to typical spacing between lattice planes in NQD assemblies whereas GIWAXS detects scattered peaks at angles above ten degrees and probes ~5 Å distances that correspond to spacing between atomic lattice planes within NQDs. The combination of GISAXS/GIWAXS therefore is a powerful tool to generate detailed information about the symmetry and orientation of individual NQDs as well as their assembled structures and will be used for studies presented in this thesis.

1.6 Theoretical Framework for Charge Transfer in NQD Systems

In this section, I will discuss theoretical framework that describes charge transfer in NQD systems. Understanding charge transfer mechanisms and dynamics have major scientific and technological consequences for NQDs – we will see in this section, charge transfer rates are dependent on (1) energy level offsets (discussed in section 1.5.1), (2) electronic coupling (discussed in section 1.5.2) and (3) the structural and material aspects of the surrounding (discussed in section 1.5.3). Therefore, charge transfer rates serve as a crucial observable to probe the effect of three major factors mentioned above on the optoelectronic properties of NQDs and are heavily studied in various NQD systems [60, 79-82]. Furthermore, the charge transfer in NQD systems is a key process in device applications of NQDs and better fundamental understanding will enable successful development of NQD technologies.

Among theoretical frameworks, Marcus theory has been widely successful in describing charge transfer in molecular systems.[83] For NQD systems, only a few reports have systematically studied charge tranfer in the context of Marcus theory and the applicability of the theory for NQDs is still being investigated in various systems and regimes.[80, 82, 84-87] [88-90] Here I present a brief introduction on Marcus theory and how energy level offsets, electronic coupling and the surrounding affect the charge transfer rate.

In non-adiabatic regime with weak electronic coupling between the donor and acceptor, the electron transfer rate can be expressed as Fermi's Golden Rule:[91]

$$\mathrm{k_{ET}} = \frac{2\pi}{\hbar}|\mathrm{H_{DA}}|^2(\mathrm{FCWD}) \tag{1.13}$$

that separates contributions from electronic ($\mathrm{H_{DA}}$) and nuclear wave functions (FCWD). $\mathrm{H_{DA}}$ describes coupling between electronic wavefunctions whereas FCWD is Franck-Condon weighted density of states that describes overlap of nuclear wavefunctions of the reactant and the product - the reorganization of bond lengths and angles required for the charge transfer from donor to acceptor to occur. I will first discuss the simplest case of charge transfer between a single reactant state to a single product state, between NQDs with discrete energy levels for example, and move onto a case where the charge transfer to a continuum of product states with distribution in energy.

Between a single reactant state to a single product state, the electronic wavefunction coupling term, H_{DA}, is often approximated with tunneling formula with exponential dependence on distance between the donor and the acceptor, D_{DA}, due to exponential drop-off of the wavefunctions.

$$\mathrm{H_{DA}} = \mathrm{H_{DA}^{o}} \exp[-\beta \mathrm{D_{DA}}] \tag{1.14}$$

where H^{o}_{DA} is the electronic coupling with $D_{DA} = 0$ and β is the attenuation rate that depends on the medium between the donor and the acceptor.

For the Franck-Condon weighted density of state, FWCD, Marcus derived the expression:[48, 92-95]

$$\mathrm{FCWD} = \frac{1}{\sqrt{4\pi\lambda k_B T}} \exp\left[-\frac{\lambda + \Delta G^{o}}{4\lambda k_B T}\right] \tag{1.15}$$

where λ is the reorganization energy, ΔG^{o} is the standard free energy of the electron transfer reaction, k_B is the Boltzmann constant and T is temperature. The reorganization energy accounts for all the structural changes (bond length, bond angles, molecular orientations) of both the reactants and the solvent molecules during the charge transfer. The driving force for the reaction, ΔG^{o}, originates from the difference between energy levels in the donor and the acceptor.

I now discuss the case of charge transfer from a reactant state to a continuum of product states with distribution in energy.[96-98] The total charge transfer rate will be the sum of charge transfer rates to all possible acceptor states:

$$k_{ET} = \frac{2\pi}{\hbar}\int_{-\infty}^{\infty} dE\ \rho(E)|H_{DA}(E)|^2 \frac{1}{\sqrt{4\pi\lambda k_B T}} \exp[-\frac{(\lambda + \Delta G^o - E)^2}{4\lambda k_B T}] \qquad (1.16)$$

where $\rho(E)$ is the density of states, combining bulk and surface states, at energy E and the average electronic coupling term, $H_{DA}(E)$, is now a function of energy where a distribution of coupling may occur. This expression indicates that the details of the acceptor material can significantly alter the charge transfer dynamics - the details of electronic structure, crystal facets and surface structures of the acceptor material will cause different $\rho(E)$ and $H_{DA}(E)$ and thus different charge transfer rates from system to system. For nanomaterials with ill-defined surface structures, challenges associated with characterization of the surface structure render predictions difficult to make.

1.7 Organization of the Dissertation

The overarching theme of this dissertation is to present studies that show insights into the three governing factors (energy levels, coupling and structure) of the optoelectronic properties of artificial solids discussed in section 1.5 and the solar cell and LED applications of lead salt NQDs. In chapter 2, I begin with experimental details on how to synthesize lead salt NQDs and deposit NQD thin films for devices. In chapter 3 and 4, I will discuss the topic of NQD energy levels – studies on the effect of NQD size on its energy levels and photovoltaic device behavior will be presented. In chapter 5 and 6, the topic of inter-NQD electronic coupling will be discussed - I probed rate of photogenerated exciton dissociation in NQD assemblies as a function of inter-NQD spacing and its effect on LED performance. In chapter 7, I will discuss how to control the symmetry of NQD superlattices - interaction between ligand molecules on the surface of NQD play critical roles in self-assembly process. Finally, in chapter 8, I will discuss the outlooks and future directions based on the insights obtained throughout the studies reported in this dissertation.

BIBLIOGRAPHY

[1] A. L. Efros, A. L. Efros, Sov. Phys. Semicond. **16**, 772 (1982).

[2] L. E. Brus, The Journal of Chemical Physics. **80**, 4403 (1984).

[3] D. V. Talapin, J.-S. Lee, M. V. Kovalenko, E. V. Shevchenko, Chemical Reviews. **110**, 389 (2010).

[4] J. M. An, A. Franceschetti, S. V. Dudiy, A. Zunger, Nano Lett. **6**, 2728 (2006).

[5] A. Franceschetti, Physical Review B. **78**, 075418 (2008).

[6] I. Kang, F. W. Wise, Journal of the Optical Society of America B. **14**, 1632 (1997).

[7] P. Bhattacharya, S. Ghosh, A. D. Stiff-Roberts, Annual Review of Materials Research. **34**, 1 (2004).

[8] R. Dingle, W. Wiegmann, C. H. Henry, Physical Review Letters. **33**, 827 (1974).

[9] N. F. Borrelli, D. W. Smith, Journal of Non-Crystalline Solids. **180**, 25 (1994).

[10] A. Lipovskii, E. Kolobkova, V. Petrikov, I. Kang, A. Olkhovets, T. Krauss, M. Thomas, J. Silcox, F. Wise, Q. Shen, S. Kycia, Applied Physics Letters. **71**, 3406 (1997).

[11] C. B. Murray, D. J. Norris, M. G. Bawendi, J. Am. Chem. Soc. **115**, 8706 (1993).

[12] L. Manna, E. Scher, A. Alivisatos, J. Am. Chem. Soc. **122**, 12700 (2000).

[13] J. Hu, L.-s. Li, W. Yang, L. Manna, L.-W. Wang, A. P. Alivisatos, Science. **292**, 2060 (2001).

[14] S. Kan, T. Mokari, E. Rothenberg, U. Banin, Nat. Mater. **2**, 155 (2003).

[15] L. Manna, D. J. Milliron, A. Meisel, E. C. Scher, A. P. Alivisatos, Nat Mater. **2**, 382 (2003).

[16] Y. Yin, R. M. Rioux, C. K. Erdonmez, S. Hughes, G. A. Somorjai, A. P. Alivisatos, Science. **304**, 711 (2004).

[17] K.-S. Cho, D. V. Talapin, W. Gaschler, C. B. Murray, J. Am. Chem. Soc. **127**, 7140 (2005).

[18] A. Houtepen, R. Koole, D. Vanmaekelbergh, J. Meeldijk, J. Am. Chem. Soc. (2006).

[19] C. Schliehe, B. H. Juarez, M. Pelletier, S. Jander, D. Greshnykh, M. Nagel, A. Meyer, S. Foerster, A. Kornowski, C. Klinke, H. Weller, Science. **329**, 550 (2010).

[20] V. K. LaMer, R. H. Dinegar, J. Am. Chem. Soc. **72**, 4847 (1950).

[21] Y. De Smet, L. Deriemaeker, E. Parloo, R. Finsy, Langmuir. **15**, 2327 (1999).

[22] C. Murray, C. Kagan, M. Bawendi, Annu. Rev. Mater. Res. **30**, 545 (2000).

[23] A. J. Nozik, M. C. Beard, J. M. Luther, M. Law, R. J. Ellingson, J. C. Johnson, Chemical Reviews. **110**, 6873 (2010).

[24] A. Pandey, P. Guyot-Sionnest, Science. **322**, 929 (2008).

[25] A. J. Nozik, Physica E: Low-dimensional Systems and Nanostructures. **14**, 115 (2002).

[26] I. Gur, N. A. Fromer, M. L. Geier, A. P. Alivisatos, Science. **310**, 462 (2005).

[27] G. I. Koleilat, L. Levina, H. Shukla, S. H. Myrskog, S. Hinds, A. G. Pattantyus-Abraham, E. H. Sargent, ACS Nano. **2**, 833 (2008).

[28] J. M. Luther, M. Law, M. C. Beard, Q. Song, M. O. Reese, R. J. Ellingson, A. J. Nozik, Nano Letters. **8**, 3488 (2008).

[29] J. J. Choi, Y.-F. Lim, M. B. Santiago-Berrios, M. Oh, B.-R. Hyun, L. Sun, A. C. Bartnik, A. Goedhart, G. G. Malliaras, H. c. D. Abruna, F. W. Wise, T. Hanrath, Nano Letters. **9**, 3749 (2009).

[30] K. S. Leschkies, T. J. Beatty, M. S. Kang, D. J. Norris, E. S. Aydil, ACS Nano. **3**, 3638 (2009).

[31] A. G. Pattantyus-Abraham, I. J. Kramer, A. R. Barkhouse, X. Wang, G. Konstantatos, R. Debnath, L. Levina, I. Raabe, M. K. Nazeeruddin, M. Gra?tzel, E. H. Sargent, ACS Nano. **4**, 3374 (2010).

[32] J. Tang, K. W. Kemp, S. Hoogland, K. S. Jeong, H. Liu, L. Levina, M. Furukawa, X. Wang, R. Debnath, D. Cha, Nat Mater (2011).

[33] V. L. Colvin, M. C. Schlamp, A. P. Alivisatos, Nature. **370**, 354 (1994).

[34] S. Coe, W.-K. Woo, M. Bawendi, Bulovi, Vladimir, Nature. **420**, 800 (2002).

[35] N. Tessler, V. Medvedev, M. Kazes, S. Kan, U. Banin, Science. **295**, 1506 (2002).

[36] K.-S. Cho, E. K. Lee, W.-J. Joo, E. Jang, T.-H. Kim, S. J. Lee, S.-J. Kwon, J. Y. Han, B.-K. Kim, B. L. Choi, J. M. Kim, Nat Photon. **3**, 341 (2009).

[37] S. A. McDonald, G. Konstantatos, S. Zhang, P. W. Cyr, E. J. D. Klem, L. Levina, E. H. Sargent, Nature Materials. **4**, 138 (2005).

[38] G. Konstantatos, I. Howard, A. Fischer, S. Hoogland, J. Clifford, E. Klem, L. Levina, E. H. Sargent, Nature. **442**, 180 (2006).

[39] V. Sukhovatkin, S. Hinds, L. Brzozowski, E. H. Sargent, Science. **324**, 1542 (2009).

[40] D. V. Talapin, C. B. Murray, Science. **310**, 86 (2005).

[41] R. Y. Wang, J. P. Feser, J.-S. Lee, D. V. Talapin, R. Segalman, A. Majumdar, Nano Lett. **8**, 2283 (2008).

[42] P. Alivisatos, Nature Biotechnology. **22**, 47 (2003).

[43] G. Markovich, C. P. Collier, S. E. Henrichs, F. o. Remacle, R. D. Levine, J. R. Heath, Acc. Chem. Res. **32**, 415 (1999).

[44] O. Lazarenkova, A. Balandin, J. Appl. Phys. **89**, 5509 (2001).

[45] F. Remacle, R. Levine, ChemPhysChem. **2**, 20 (2001).

[46] K. Beverly, J. Sample, J. Sampaio, F. Remacle, J. Heath, R. Levine, PNAS. **99**, 6456 (2002).

[47] T. Hanrath, Journal of Vacuum Science & Technology A: Vacuum, Surfaces, and Films. **30**, 030802 (2012).

[48] R. A. Marcus, Annual Review of Physical Chemistry. **15**, 155 (1964).

[49] J. Heinze, Angewandte Chemie International Edition. **23**, 831 (1984).

[50] C. Wang, M. Shim, P. Guyot-Sionnest, Science. **291**, 2390 (2001).

[51] S. N. Inamdar, P. P. Ingole, S. K. Haram, Chem. Phys. Chem. **9**, 2574 (2008).

[52] M. Soreni-Harari, N. Yaacobi-Gross, D. Steiner, A. Aharoni, U. Banin, O. Millo, N. Tessler, Nano Lett. **8**, 678 (2008).

[53] J. C. Fuggle, J. E. Inglesfield, Unoccupoed Electronic States, Springer-Verlag, Berlin (1992).

[54] A. Franceschetti, A. Zunger, Physical Review B. **62**, 2614 (2000).

[55] L. E. Brus, The Journal of Chemical Physics. **79**, 5566 (1983).

[56] B.-R. Hyun, A. C. Bartnik, L. Sun, T. Hanrath, F. W. Wise, Nano Letters. **11**, 2126 (2011).

[57] R. E. Chandler, A. J. Houtepen, J. Nelson, D. Vanmaekelbergh, Physical Review B. **75**, 085325 (2007).

[58] D. Yu, C. Wang, P. Guyot-Sionnest, Science. **300**, 1277 (2003).

[59] J. J. Choi, Y.-F. Lim, M. B. Santiago-Berrios, M. Oh, B.-R. Hyun, L. Sun, A. C. Bartnik, A. Goedhart, G. G. Malliaras, H. D. Abruna, F. W. Wise, T. Hanrath, Nano Letters. **9**, 3749 (2009).

[60] J. J. Choi, J. Luria, B.-R. Hyun, A. C. Bartnik, L. Sun, Y.-F. Lim, J. A. Marohn, F. W. Wise, T. Hanrath, Nano Letters. **10**, 1805 (2010).

[61] J. M. Luther, M. Law, Q. Song, C. L. Perkins, M. C. Beard, A. J. Nozik, ACS Nano. **2**, 271 (2008).

[62] D. A. R. Barkhouse, R. Debnath, I. J. Kramer, D. Zhitomirsky, A. G. Pattantyus-Abraham, L. Levina, L. Etgar, M. Gratzel, E. H. Sargent, Advanced Materials. **23**, 3134 (2011).

[63] L. Sun, J. J. Choi, D. Stachinik, A. Bartnik, B.-R. Hyun, G. G. Malliaras, T. Hanrath, F. Wise, Nature Nanotechnology (2012).

[64] M. V. Kovalenko, M. Scheele, D. V. Talapin, Science. **324**, 1417 (2009).

[65] J. Lee, M. Kovalenko, J. Huang, D. Chung, T. Dmitri, Nature (2011).

[66] A. Nag, M. V. Kovalenko, J.-S. Lee, W. Liu, B. Spokoyny, D. V. Talapin, J. Am. Chem. Soc. **133**, 10612 (2011).

[67] H. Zhang, B. Hu, L. Sun, R. Hovden, F. W. Wise, D. A. Muller, R. D. Robinson, Nano Lett. **11**, 5356 (2011).

[68] A. T. Fafarman, W.-k. Koh, B. T. Diroll, D. K. Kim, D.-K. Ko, S. J. Oh, X. Ye, V. Doan-Nguyen, M. R. Crump, D. C. Reifsnyder, C. B. Murray, C. R. Kagan,

J. Am. Chem. Soc. **133**, 15753 (2011).

[69] W.-k. Koh, S. R. Saudari, A. T. Fafarman, C. R. Kagan, C. B. Murray, Nano Lett. **11**, 4764 (2011).

[70] K. J. M. Bishop, C. E. Wilmer, S. Soh, B. A. Grzybowski, Small. **5**, 1600 (2009).

[71] Y. Min, M. Akbulut, K. Kristiansen, Y. Golan, J. Israelachvili, Nat Mater. **7**, 527 (2008).

[72] M. P. Pileni, Accounts of Chemical Research. **41**, 1799 (2008).

[73] M. Grzelczak, J. Vermant, E. M. Furst, L. M. Liz-Marzan, ACS Nano. **4**, 3591 (2010).

[74] T. Hanrath, J. J. Choi, D.-M. Smilgies, ACS Nano. **3**, 2975 (2009).

[75] J. R. Levine, J. B. Cohen, Y. W. Chung, P. Georgopoulos, Journal of Applied Crystallography. **22**, 528 (1989).

[76] B. Smarsly, A. Gibaud, W. Ruland, D. Sturmayr, C. J. Brinker, Langmuir. **21**, 3858 (2005).

[77] B. Lee, I. Park, J. Yoon, S. Park, J. Kim, K.-W. Kim, T. Chang, M. Ree, Macromolecules. **38**, 4311 (2005).

[78] A. Gibaud, D. Grosso, B. Smarsly, A. Baptiste, J. F. Bardeau, F. Babonneau, D. A. Doshi, Z. Chen, C. J. Brinker, C. Sanchez, J. Phys. Chem. B. **107**, 6114 (2003).

[79] B.-R. Hyun, Y.-W. Zhong, A. C. Bartnik, L. Sun, H. D. Abruna, F. W. Wise, J. D. Goodreau, J. R. Matthews, T. M. Leslie, N. F. Borrelli, ACS Nano. **2**, 2206 (2008).

[80] I. n. Robel, M. Kuno, P. V. Kamat, Journal Of The American Chemical Society. **129**, 4136 (2007).

[81] W. A. Tisdale, K. J. Williams, B. A. Timp, D. J. Norris, E. S. Aydil, X. Y. Zhu, Science. **328**, 1543 (2010).

[82] K. Tvrdy, P. A. Frantsuzov, P. V. Kamat, Proceedings of the National Academy of Sciences. **108**, 29 (2011).

[83] D. M. Adams, L. Brus, C. E. D. Chidsey, S. Creager, C. Creutz, C. R. Kagan, P. V. Kamat, M. Lieberman, S. Lindsay, R. A. Marcus, R. M. Metzger, M. E. Michel-Beyerle, J. R. Miller, M. D. Newton, D. R. Rolison, O. Sankey, K. S. Schanze, J. Yardley, X. Zhu, J. Phys. Chem. B. **107**, 6668 (2003).

[84] B.-R. Hyun, Y.-W. Zhong, A. C. Bartnik, L. Sun, H. D. Abruna, F. W. Wise, J. D. Goodreau, J. R. Matthews, T. M. Leslie, N. F. Borrelli, ACS Nano. **2**, 2206 (2008).

[85] A. Kongkanand, K. Tvrdy, K. Takechi, M. Kuno, P. V. Kamat, Journal Of The American Chemical Society. **130**, 4007 (2008).

[86] B.-R. Hyun, A. C. Bartnik, J.-K. Lee, H. Imoto, L. Sun, J. J. Choi, Y. Chujo, T. Hanrath, C. K. Ober, F. W. Wise, Nano Letters. **10**, 318 (2009).

[87] E. Cánovas, P. Moll, S. A. Jensen, Y. Gao, A. J. Houtepen, L. D. A. Siebbeles, S. Kinge, M. Bonn, Nano Lett. **11**, 5234 (2011).

[88] R. Long, O. V. Prezhdo, J. Am. Chem. Soc. **133**, 19240 (2011).

[89] W. A. Tisdale, X. Y. Zhu, Proceedings of the National Academy of Sciences. **108**, 965 (2011).

[90] Y. Yang, W. Rodríguez-Córdoba, X. Xiang, T. Lian, Nano Lett. **12**, 303 (2012).

[91] J. J. Sakurai, Modern Quantum Mechanics, 1994.

[92] R. A. Marcus, The Journal of Chemical Physics. **24**, 966 (1956).

[93] R. A. Marcus, The Journal of Chemical Physics. **24**, 979 (1956).

[94] R. A. Marcus, The Journal of Chemical Physics. **43**, 679 (1965).

[95] R. A. Marcus, N. Sutin, Biochimica et Biophysica Acta (BBA) - Reviews on Bioenergetics. **811**, 265 (1985).

[96] Y. Q. Gao, Y. Georgievskii, R. A. Marcus, The Journal of Chemical Physics. **112**, 3358 (2000).

[97] Y. Q. Gao, R. A. Marcus, The Journal of Chemical Physics. **113**, 6351 (2000).

[98] S. Gosavi, R. A. Marcus, J. Phys. Chem. B. **104**, 2067 (2000).

CHAPTER 2

NANOCRYSTAL QUANTUM DOT SYNTHESIS AND THIN FILM DEPOSITION

In the first section of this chapter, the experimental details of the hot injection method to synthesize colloidal lead salt NQDs used in all of studies reported in this dissertation will be discussed. In second section, experimental details of the deposition of NQD thin films for optoelectronic devices (solar cells or LEDs) via spin-casting will be discussed. The experimental steps described in this chapter tend to be details that may be worthwhile only for beginners in the field (first year graduate students for example). Uninterested readers may skip this chapter as all of the following chapter contain essential experimental methods.

2.1 Synthesis of NQDs via hot-injection method and size determination

Methods for synthesis of lead salt (PbS and PbSe) NQDs used throughout the studies reported in this dissertation are based on modification of Murray’s original method reported in 2001 [1]. The brief introduction on the colloidal NQD synthesis mechanisms is given in section 1.3 of this dissertation. Because the presence of water or oxygen during the reaction causes different kinetics and yield of precursor conversion reactions [2] as well as oxidation of the precursor, they complicate the reaction mechanisms and often make the control of the size and shape control difficult. Thus the reactions are carried out using the standard Schlenk line air-free techniques to prevent oxygen and water to participate in the reaction.

2.1.1 Details of the reaction set-up

Schlenk line is simply a glass manifold that allows alternating connections between the reactor vessel (three neck flask in our method, shown in Figure 1.4B) and vacuum pump and inert gas flow (Figure 2.1). The vacuum is used to quickly remove the oxygen and water from the reaction flask and the Schlenk line as well as the gas species dissolved in the reactant solution (process called 'degassing'). The inert gas flow is used to back-fill the vessel after vacuuming and maintain the inert atmosphere by continuous flowing the gas. One of the ports of the Schlenk line gets connected to a vacuum pump with cold traps for protection of the pump and another port is connected to a inert gas (usually N_2) tank. The connections can be controlled by closing or opening the passage between the reaction flask to either vacuum or the inert gas flow using knobs (usually connected to teflon stoppers).

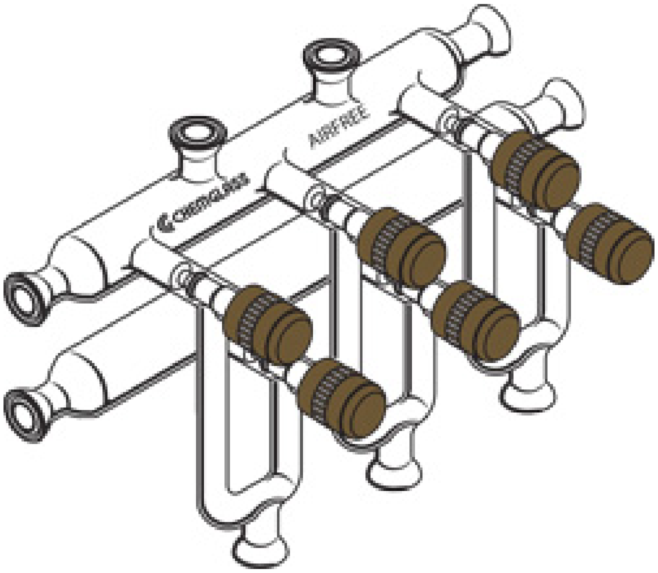

Figure 2.1: A cartoon of a typical Schlenk line. The various ports can be connected to vacuum pump, gas cylinders, reaction flasks and bubblers. The brown knobs connected to Teflon stoppers are used to regulate the connection pathways between the ports. (Copyright 2008, Chemglass Life Sciences)

One of the remaining ports of the Schlenk line is used for a vacuum gauge to monitor the pressure during vacuuming and refilling with inert gas. Lastly, one port is connected to a bubbler as the safety outlet - without the safety outlet, the high pressure of the gas tank may break the Schlenk line. A bubbler is a glass container with inert oil, such as mineral oil, inserted inside so that the oil blocks the passage between the inlet and the outlet of the bubbler. As the gas is forced to pass through the bubbler, it makes bubbles (and thus the term 'bubbler') that allow quick estimation of the inert gas flow rate and whether the pressure inside the Schlenk line is maintained higher than atmospheric pressure. During the maintenance of the inert atmosphere for the reaction, the gas flow is turned up enough to maintain higher than atmospheric pressure inside the reaction flask and the Schlenk line to account for any leaks in joints. If there are any leaks, higher pressure inside will ensure the leaks to be outward instead of inward. Consistent and yet not excessive bubbling throughout the entire duration of inert atmosphere for the reaction is desired to block leakage of oxygen or water into the reaction and waste of the inert gas. When switching between vacuum mode to inert gas flow mode, one should be extremely careful about properly opening and closing the knobs in appropriate configuration to block unfortunate incidents such as pulling vacuum on the bubbler that may cause the mineral oil to get sucked into the Schlenk line or breaking the Schlenk line by connecting it to high pressure gas cylinder with the every outlet knob closed.

For the three neck flask, the middle neck is usually connected to the Schlenk line through a condenser (Figure 1.4B) while the other necks are covered by rubber septa to ensure isolation from the atmosphere. The rubber septa serve as gateways for a temperature probe (by puncturing one of the septum with the probe) and syringe needles for reactant injection and product collection without causing the oxygen or water leak to inside. The flask is placed on a heating mantle and a stir plate. The heating mantle is connected to the temperature probe in a feed-back control loop for temperature regulation during the reaction. The stir plate rotates a magnetic stirrer placed inside the flask to ensure homogenous mixing of reactants. The power supplied to the heating mantle needs to be chosen to ensure adequate heat source to reach desired temperature without causing too much of temperature overshoot. The stirring speed of the magnetic stirrer needs to be controlled to ensure homogeneous mixing of the reactants without causing instability of the magnetic stirrer.

2.1.2 Synthesis of PbSe NQDs

PbSe NQDs used in this dissertation were prepared following the method reported by Yu et al. [3] The synthesis was carried out in a 100 mL three-necked flask under an inert nitrogen atmosphere using the Schlenk line. The reactants were used as purchased without any purification steps. Lead oxide (PbO) is used as the lead source. PbO is a yellowish red powder that tends to easily stick to the glass wall and so care must be taken to put all of the power on the bottom of the flask instead of flask neck and side walls where the reactant solution does not reach. The amount of PbO inserted into the flask should be measured by taking the weight of the plastic boat with the PbO before and after inserting the PbO into the flask to account for residual PbO stuck on the plastic boat. For non-coordinating reaction solvent, 1-octadecene (ODE) is used. For ligand molecules, oleic acid is used. Both ODE and oleic acid are viscous liquid at room temperature and synringe with a needle with large enough diameter should be used for transportation of the liquids. To measure the amount of ODE and oleic acid inserted into the reactor, a suggested method is first to put the liquid in a small vial and measure the reduction in mass of the vial plus the liquid after pulling desired amount into a syringe with previously measured mass. The liquid is then injected into the reaction flask and the mass of the syringe plus the residual liquid is measured. The amount of liquid inserted into the reaction flask can be calculated by subtracting the mass of residual liquid from the mass pulled out of the vial. After inserting a magnetic stirrer into the reactant solution, the reaction flask is sealed with rubber septa and connection to the Schlenk line. The vacuum pump and inert gas flow are then used to remove oxygen and water from inside the flask. The stir plate is turned on to vigorously stir the solution throughout the remainder of the reaction.

Upon heating (usually to 160 ^{o}C), reaction occurs between PbO and oleic acid such that each lead atom becomes coordinated with two oleate molecules, in which carboxylic acid group is deprotonated, while producing water. The water is removed through heating, degassing and inert gas flow. By this time the reactant solution should be colorless and clear. For the selenium precursor solution, elemental Se powder (black powder) is dissolved in trioctylphosphine (TOP) to make "TOP-Se" solution inside a glovebox by stirring until the solution becomes completely clear (this usually takes many hours and most people make the solution the night before). Shaking the solution vigorously can increase the speed of dissolution. However, the fast dissolution via shaking causes the TOP-Se solution to get hotter slightly and, for the consistent drop in temperature of the reaction solution upon injection of the TOP-Se into the lead-oleate solution, adequate wait time is needed until the TOP-Se solution cools back down to room temperature. The TOP-Se solution is then loaded into a syringe with a needle inside the glovebox, taken out of the glovebox and quickly injected into the lead-oleate solution. To minimize the exposure of TOP-Se to air, the syringe can be put into an air-tight plastic bag before being taken out of the glovebox. For injection of TOP-Se, the plastic bag and the rubber septum are punctured with the needle simultaneously.

In a typical synthesis, PbO (4 mmol) and various amount of oleic acid were dissolved in ODE to yield a precursor solution with [Pb] = 0.3 M and a molar Pb:oleic acid ratio between 1:2 to 1:6. The larger the amount of oleic acid, which coordinates Pb, smaller number of nuclei gets formed and larger amount of remaining precursors get slowly added onto the nuclei during the NQD growth stage. Thus, assuming that the reaction goes to completion (for PbSe case, it is not true due to low reactivity of TOP-Se [4] but the trend still holds), larger amount of oleic acid will result in smaller number of NQDs with larger diameter. The PbO, oleic acid and ODE solution was heated to 160^{o}C for 1 hour under flowing nitrogen to form lead oleate. In a glovebox, Se was dissolved in trioctylphosphine (TOP) to yield a 1 M stock solution. Small amount of diphenylphospine (4.5 mM) was added to the TOPSe solution to increase the yield due to higher reactivity of secondary phosphines compared to TOP [4, 5]. 12 ml of the 1 M TOP-Se solution was rapidly injected into the vigorously stirred, hot lead oleate solution. PbSe NQDs formed immediately after injection and their size was tuned through adjustments in temperature (120-180^{o}C) and reaction time (0.2-5 min). After the elapsed reaction time, the solution was quenched by transferring the flask to a water bath. Continuous stirring during the quenching step is important for achieving monodisperisty among NQD population.

After quenching, the product mixture is ready to be 'cleaned' to collect NQDs by separating them from the remaining reactants and by-products of the reaction [4, 6]. A small amount of hexane (~5 mL) is added to the product mixture and minimum amount of ethanol is added until the mixture becomes turbid due to flocculation of NQDs. The larger the NQD diameter, the smaller amount of ethanol is needed for flocculation. Ethanol should be added gradually only until the point of flocculation as adding too much ethanol strips off significant amount of ligands off of the NQD surface [7] and cause aggregation of NQDs. The mixture is then centrifuged to precipitate the NQDs to the bottom of the centrifuge tubes. The supernatant, which has most of the left-over reactant and by-product dissolved in, is discarded and the black NQD precipitate is cleaned two more times by re-dissolving in fresh hexane (~5 mL), adding ethanol to cause flocculation and centrifuging. After the washing step, the NQDs are stored in dry form inside a N_2 environment glovebox.

2.1.3 Synthesis of PbS NQDs

The PbS NQD synthesis method is based on the work by Hines and Scholes [8] and is very similar to the PbSe synthesis method described above. The synthesis was carried out in a 100 mL three-necked flask under an inert nitrogen atmosphere. In a typical synthesis, 3 mmol of PbO was mixed with oleic acid in a 1:2 to 1:25 molar ratio, depending on the desired NQD size. The PbS NQD reaction, unlike the PbSe NQD reaction, goes to completion as the reactivity of the sulfur source, *bis*(trimethylsilyl)sulfide (TMS), is much higher than TOP-Se. Thus, the size tuning of PbS NQDs is mostly achieved by tuning the lead to oleic acid ratio and injection temperature. After adding the PbO and oleic acid in the flask, an appropriate amount of ODE was added to make the total volume of solution 30 mL. The solution was degassed by heating to 150 ^{o}C for 1 hour under flowing nitrogen. In a glovebox, 378 µL of TMS was dissolved in 18 mL of ODE and stirred thoroughly. A 15 mL aliquot of the TMS solution was rapidly injected into a vigorously stirred, hot lead oleate solution held at a temperature between 90 and 150 ^{o}C (depending on desired NQD size). PbS NQDs formed immediately after injection and were collected after 1 minute of reaction. Following synthesis, the NQDs were cleaned three times by sequential precipitation with ethanol and redisperson in hexane.

2.1.4 Determination of NQD size

For determination of the NQD size, 'sizing curves' are used [9]. The sizing curves relate the location of the first exciton peak in the absorption spectra with the diameters measured by TEM. Once the validity of the sizing curves is confirmed, the determination of the NQD size is simply done by taking absorption spectra of the NQDs and locating the first excitonic peak (Figure 2.2). For PbSe NQDs, the sizing curve formula used throughout this dissertation is the one from Moreels *et al*. [9] that was obtained through fitting carefully obtained experimentally obtained sizing curve.

$$E_o^{PbSe} = 0.278 + \frac{1}{0.016d^2 + 0.209d + 0.45} \tag{2.1}$$

where E_o^{PbSe} is the energy gap of the NQD in eV and d is the mean NQD diameter in nm.

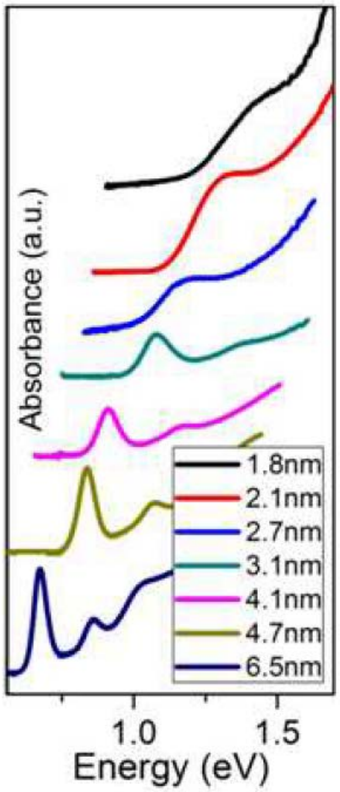

Figure 2.2: Absorption spectra of PbSe NQDs with different average diameters.

Similarly, for PbS NQD size determination, absorption spectrosopcy and the sizing curve formula obtained by fitting the $\boldsymbol{k} \cdot \boldsymbol{p}$ theory calculation [10] are used throughout this dissertation.

$$E_o^{PbS} = 0.41 + \frac{1}{0.0328d^2 + 0.2373d - 0.2049} \tag{2.2}$$

2.2 Lead salt NQD thin film deposition for optoelectronic devices

Pre-patterned ITO coated (~80 nm thick with sheet resistance of ~15 Ohm/square) glass substrates (25 mm x 25 mm x 1.1 mm) were purchased from Kintec, Hong Kong. If the substrates need to be labeled, diamond scribers are used to scratch labels on a corner of the substrate before the washing steps. The substrates are first cleaned by vigorous scrubbing for more than 30 seconds on each side with a swab soaked with detergent dissolved in water. Right after the scrubbing, before the water dries on the surface, the substrates are sonicated in a mild detergent and again in de-ionized water for 5 minute each. The substrates are then rinsed with flowing de-ionized water for 4 minutes. After the rinsing, the substrates are taken out of the water and quickly dried in a nitrogen stream to block slow evaporation of water that usually leaves dry mark features.

The cleaned substrates are treated with UV-ozone for 10 minutes to remove organic layers still stuck on the substrates. Most UV-ozone cleaners need some warm-up time and it is advisable to turn on the UV-ozone cleaner for a few minutes before the actual cleaning. Incomplete UV-ozone treatment will severely reduce the wetability of hydrophilic solution such as poly(3,4-ethylenedioxythiophene) poly(styrenesulfonate) (PEDOT:PSS) solution and results in film with inadequate quality for devices. The side of the substrate that NQDs will be deposited on should face upward toward the UV-ozone.

For devices that require PEDOT:PSS as hole transporting layer, PEDOT:PSS solution (purchased from H.C. Starck) was filtered through 0.45 μm Polyvinylidene fluoride (PVDF) syringe filter within a few minutes of the film deposition. (As time passes, PEDOT:PSS tend to aggregate again and filtering needs to be performed again after a few hours) The substrate should have been treated with UV-ozone not more than ~15 minutes before the PEDOT:PSS layer deposition to achieve good wetting. 200 µL of the PEDOT:PSS solution is dispensed on the substrate using an automatic pipette and then spin-casted at 6000 rpm for 1 minute. The deposited PEDOT:PSS was then baked on a hot plate at 170 ^{o}C for 4 minutes to remove residual water. This procedure typically results in smooth, ~30 nm PEDOT:PSS thin film.

For deposition of lead salt NQD thin films, I used ‘sequential spin-casting’ method. PbSe NQD in chlorobenzene solution (with typical concentration of 30 mg/mL) is prepared and filtered through 0.2 µm PVDF filter to remove dusts, particulates and aggregated NQDs. This filtering step is crucial in avoiding electrical shorts forming through the cracks in the NQD thin film - any aggregates or particulates will be orders of magnitude bigger than the NQD film thickess (~100 nm) and causes major irregularities that most likely result in cracks. The substrate for the NQD thin film is placed on top of a chuck in the spin-coater and vacuum on the backside of the substrate through the chuck is applied to fix the substrate on the chuck. A test spin run is advisable to check for the robustness of the substrate fixation on the chuck before dispensing solutions. Using an automatic pipette, 150 µL of the NQD/chlorobenzene solution is dispensed on the substrate and spin-casted typically at 1000 rpm for 1 minute. After the spin-coating the substrate should be uniformed coated with ~20 nm of NQD thin film. If any irregular features can be discerned by human eyes, that indicates deposition of particulates that adversely affect the film quality and device performance and it is advisable to prepare freshly filtered NQD solution and another cleaned substrate.

To replace bulky oleic acid that electrically insulates the NQD from each other and the surrounding, various short molecule ligand solution (0.1M of ethanedithiol (EDT) in acetonitrile solution for example) is dispensed on top of the deposited NQD film and left for ~30 seconds to allow more than adequate time for the ligand exchange reaction. The ligand solution also needs to be filtered through 0.2 µm PVDF filter right before usage to remove any particulates present in the solution. Depending on the wetability of the ligand solution, 300 ~ 500 µL of the ligand solution is needed to cover the entire 25 mm x 25 mm substrate surface with NQD film on top. Upon dispensing the ligand solution, the color of the NQD film changes slightly indicating changes in film thickness, optical properties and etc. Rapid, uniform and complete coverage of the NQD film by the ligand solution is expected to be beneficial by reducing inhomogeneous ligand exchange across the film. After the ligand exchange, the solution is removed from the substrate by spin-casting at 1000 rpm for 1 minute. Pure acetonitrile is then dispensed on top of the film and spun-cast to remove residual free standing ligand molecules. Lastly, pure chlorobenzene is dispensed on top of the film and spin-casted to further remove any remaining free standing ligand molecules as well as NQDs that have been properly ligand-exchanged. This completes one cycle of the ‘sequential spin-casting’. Additional cycles of depositions are performed to form crack-free PbSe NQDs films with desired thickness.

BIBLIOGRAPHY

[1] C. B. Murray, S. Sun, W. Gaschler, H. Doyle, T. A. Betley, C. R. Kagan, IBM Journal of Research and Development. **45**, 47 (2001).

[2] H. Liu, J. S. Owen, A. P. Alivisatos, J. Am. Chem. Soc. **129**, 305 (2006).

[3] W. W. Yu, J. C. Falkner, B. S. Shih, V. L. Colvin, Chemistry of Materials. **16**, 3318 (2004).

[4] C. M. Evans, M. E. Evans, T. D. Krauss, J. Am. Chem. Soc. **132**, 10973 (2010).

[5] J. Joo, J. M. Pietryga, J. A. McGuire, S.-H. Jeon, D. J. Williams, H.-L. Wang, V. I. Klimov, J. Am. Chem. Soc. **131**, 10620 (2009).

[6] J. S. Steckel, B. K. H. Yen, D. C. Oertel, M. G. Bawendi, J. Am. Chem. Soc. **128**, 13032 (2006).

[7] M. Law, J. M. Luther, Q. Song, B. K. Hughes, C. L. Perkins, A. J. Nozik, J. Am. Chem. Soc. **130**, 5974 (2008).

[8] M. A. Hines, G. D. Scholes, Advanced Materials. **15**, 1844 (2003).

[9] I. Moreels, K. Lambert, D. De Muynck, F. Vanhaecke, D. Poelman, J. C. Martins, G. Allan, Z. Hens, Chemistry of Materials. **19**, 6101 (2007).

[10] I. Kang, F. W. Wise, Journal of the Optical Society of America B. **14**, 1632 (1997).

CHAPTER 3

TUNABLE ENERGY LEVELS: EFFECT OF NQD ENERGY LEVEL LOCATIONS ON PHOTOVOLTAIC BEHAVIOR[1]

3.1 Introduction

Colloidal semiconductor nanocrystal quantum dots (NQDs) potentially offer major benefits as photovoltaic materials in next-generation solar cells. Synthetic adjustments in the NQD size, shape and composition provide control over electronic and optical properties [2-7]. Coupled with their high absorption cross section and low-cost solution based synthesis and processing, these materials hold enormous promise for the efficient solar energy conversion in inexpensive, thin film photovoltaic devices.

For their application in next-generation solar energy conversion technologies, the NQDs must be integrated into scalable, robust and low-cost device structures that electronically couple the photoactive nanostructures to an external circuit. The extraction of photogenerated charges from the point of generation to the external electrodes involves a series of complex sub-processes which are subject to various energetic, kinetic, and structural constraints. Recent intensive research efforts by several groups have attempted to resolve the charge extraction challenge in a variety of device architectures such as NQD Schottky devices [8-10], NQD bilayer devices

---

[1] The results presented in this chapter have been published in Ref [1].

[11, 12], NQD-polymer hybrid solar cells [13, 14] and NQD sensitized TiO_2 cells [15-18].

Rational progress towards more effective extraction of photogenerated charges across the various nanostructured interfaces will require better fundamental understanding of the NQD energy levels and interfacial charge transfer mechanisms. The challenge in probing the intrinsic characteristics of the NQD active layer stems from the fact that the integration of colloidal NQDs into working devices involves chemical and physical treatments that inevitably modify the NQD surface and related electrical [19, 20], optical [21], and structural [22] properties. Although photovoltaic test structures based on metal/NQD Schottky junctions have shown encouraging performance and provided initial insights into the extraction of photogenerated charges from NQDs [8-10], the direct metal/NQD contact introduces strong electronic perturbation to the NQD and hence partially obscures information about the intrinsic size dependent photovoltaic performance of the NQD active layer.

Here we report fabrication and characterization of NQD based solar cells that rely on an excitonic solar cell mechanism [23, 24] wherein photogenerated charges are extracted from the NQD layer into electron and hole transporting layers. We hypothesized that design of NQD excitonic solar cells would minimize the perturbation to the NQD energy levels and enable direct correlation between the electronic states of NQD and the photovoltaic device performance. Moreover, an excitonic solar cell structure may perform better than Schottky structure which are fundamentally limited by low device open circuit voltages (V_{oc}) constrained to about half the band-gap of the photoactive material [25]. Due to the fundamentally different charge separation mechanism, excitonic solar cells may allow higher open circuit voltages, in certain cases exceeding even the difference in workfunctions of the electrodes [26]. To test this hypothesis, we fabricated and tested excitonic solar cell structures comprised of NQD active layer sandwiched between an electron transporting layer formed with semiconducting nanoparticle film and an organic thin film as the hole transporting layer.

We focused on PbSe NQD as the active layer material since it provides an advantageous experimental testbed for the study of NQD based photovoltaics for a number of reasons. First, robust and precisely size-tunable synthesis methods [2, 4, 7] enable the NQD diameter to be adjusted in a range of 2 to 10 nm. Coupled with the large Bohr diameter of the exciton in PbSe (46 nm) [6], this synthetic tunability translates into control over the NQD energy gap from 1.4 to 0.4 eV - enabling solar energy conversion extended into the near infra-red region. Second, strong quantum confinement effects have a pronounced impact on the electronic coupling of proximate NQDs – a critical requirement for efficient charge transport from the point of photogeneration to the external electrodes. Chemical and physical treatments of PbSe NQD thin films that increase the electronic coupling between NQDs by displacing the long insulating alkyl ligands and bringing NQDs closer to each other have been shown to enhance the film conductivity by up to 10 orders of magnitude [19, 20]. Third, strong confinement effects influence fundamental photophysical interactions between incident photons and charges in NQDs and may allow generation of multiple excitons [27-29]. However, the efficiency, the fundamental mechanism and implications on solar cell performance of multiexciton generation are subject to continued debate [21, 30-35]. Lastly, recent progress towards processing PbSe NQD films with advanced control over surface chemistry and film morphology [19, 20] provides the experimental versatility in device design to tackle the stringent energetic, kinetic, and structural constraints to efficient charge separation and collection. In short, lead salt NQDs have established themselves, in a relatively short time, as one of the scientifically most intriguing and technologically highly promising material systems for NQD based photovoltaics.

3.2 Measurement of Absolute Energy Levels of PbSe NQDs

To access the full spectrum of PbSe NQD diameters and related energy gaps, we synthesized PbSe NQD by following two complementary methods. PbSe NQDs with diameters bigger than 2 nm were synthesized by following the hot injection method from Yu et al. [7] Small PbSe NQDs with diameters smaller than 2 nm were synthesized via the magic cluster synthesis reported by Evans et al. [2] NQD size and shape were determined by transmission electron microscopy (TEM) and the corresponding size-dependent optical energy gap was characterized with absorption spectroscopy (Details of the NQD synthesis and characterization are provided in the supplementary information in Appendix A).

In contrast to the progress in experimental and theoretical efforts to understand the electronic structure *within* the nanocrystal [36-38], the knowledge of *absolute* energy levels (*i.e.*, ionization energy and electron affinity relative to vacuum) and their strong correlation to chemical and physical properties of the interface is lagging behind. To address this gap, we integrated cyclic voltammetry and optical measurements to determine size dependent PbSe NQD energy levels. Details on the cyclic voltammetry measurements are provided in the supplementary information chapter (Appendix A). The measured PbSe NQD energy levels (black circles) match well with a theoretical model based on a 4-band **k·P** Hamiltonian with correction for dielectric effect (black lines) [15, 37, 39] as well as experimental result reported by Jiang et al. [14] Figure 3.1B shows the diameter dependent trend in NQD HOMO and LUMO levels and the agreement with the theoretical model.

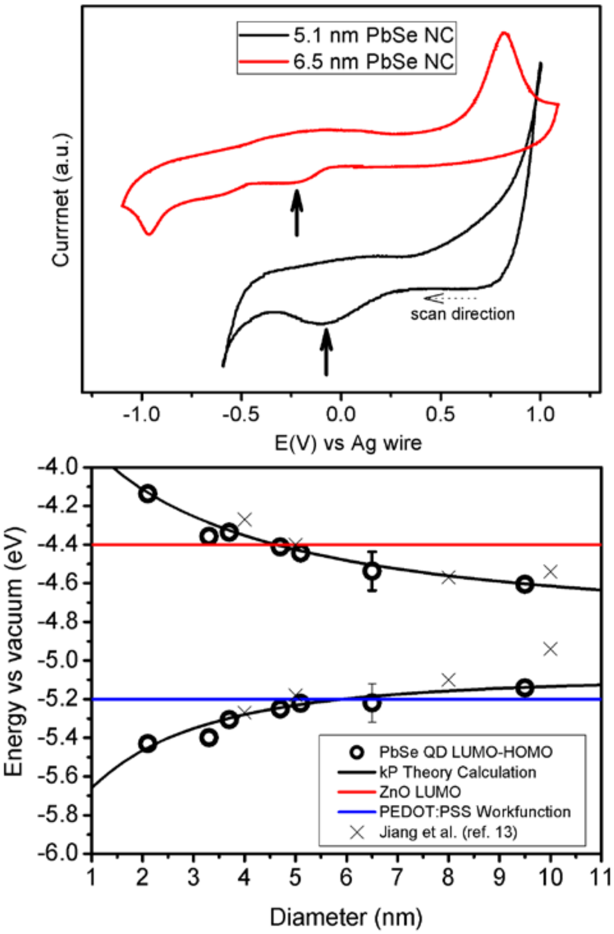

Figure 3.1: (A) Cyclic voltammogram from 5.1 and 6.5 nm PbSe NQDs. The first reduction peaks (pointed with arrows) was used to calculate the nanocrystal LUMO level. (B) Size dependent PbSe NQD energy levels measured by cyclic voltammetry (black dots). Measured energy levels show good fit with theoretical calculation (black line) and values from reference 13 (black axes). The red line shows ZnO LUMO level and the blue line shows the PEDOT:PSS workfunction.

3.3 Effect of NQD Energy Level Locations on Photovoltaic Behaviors

Next, we probed the effect of interfacial energy level offset on charge transport characteristics in photovoltaic test structures. We expected that the judicious choice of electrode material contacting the NQD should allow us to probe interfacial charge separation that is predetermined by the NQD diameter dependent energy level offset. Specifically, based on the NQD energy level trends in Figure 3.1, we designed test structures that can provide insights into two distinct performance domains. One, anticipated for small diameter NQDs, in which the interface energy level offset provides a positive driving force for charge transfer (akin to a type II heterojunction) and the other in which interface charge transfer is energetically unfavorable (akin to a type I heterojunction).

To test this hypothesis, we fabricated device structures comprised of variable-diameter PbSe NQD layer sandwiched between a semiconducting layer and an organic electrode layer with established energy levels. We chose ZnO, with LUMO of -4.4 eV [40] (red line in Figure 3.1B), as the electron collection layer and poly(3,4-

ethylenedioxythiophene):poly(styrenesulfonate) (PEDOT:PSS), with workfunction of -5.2 eV [41] (blue line in Figure 3.1B), as the hole collection layer. The energy levels shown in Figure 1, predicts the critical NQD diameter defining the transition between the two device performance domains to occur at approximately 4.5 nm. NQDs with a diameter below this threshold should experience an energy landscape favorable for photogenerated electrons to be transferred into the ZnO layer while holes are transferred into the underlying PEDOT:PSS layer. Conversely, devices prepared from larger NQDs (d > 4.5 nm) should not exhibit a photovoltage due to the lack of an energetic driving force for interface charge transfer.

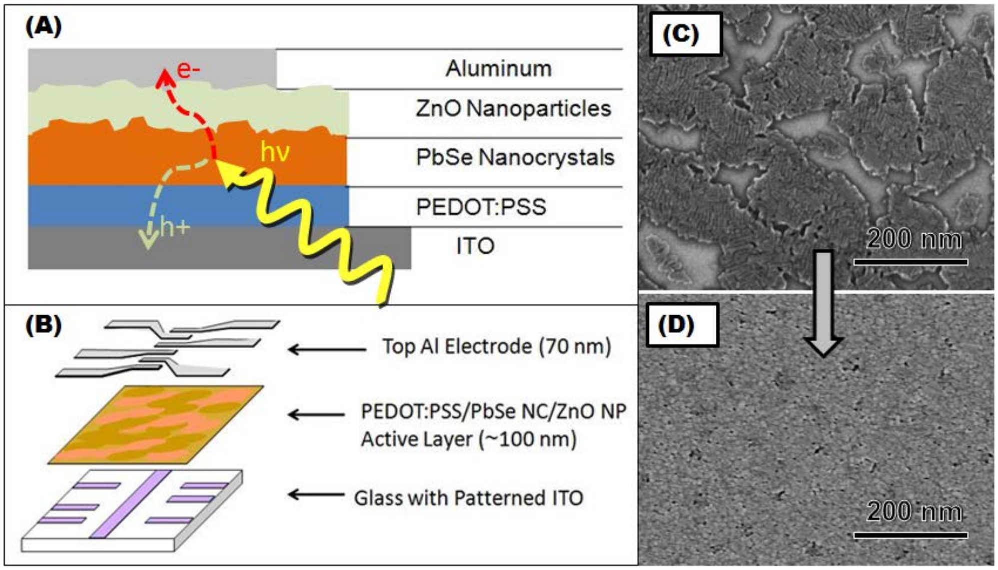

Figure 3.2: (A) PbSe NQD photovoltaic device structure that employs ZnO and PEDOT:PSS as electron and hole collection layers respectively. (B) The geometric pattern of our devices. Each sample has six working devices with area of 0.03 cm^2. (C) SEM image of PbSe NQD film from one cycle of 'sequential spin casting' shows

nanoscale cracks. (D) Three cycles of sequential spin-casting gave robust, crack-free PbSe NQD film.

Figure 3.2A shows the device configuration. Details of the device fabrication are given in the Appendix A. Briefly, starting with a cleaned, pre-patterned ITO substrate, we successively spin-coated PEDOT:PSS layer, PbSe NQD layers, ZnO nanoparticle layers followed by thermal evaporation of an aluminum top contact electrode to form an ohmic contact with ZnO [42] (Figure 2B). ZnO nanoparticles were prepared based on adaptation of method reported by Beek et al. [43] The long chain alkyl ligands coating the surface of the as-synthesized PbSe NQD were displaced by exposing the film to ethanedithiol (EDT). This chemical treatment accomplished dual goals of increased film conductivity [19, 20] and decreased solubility due to the removal of insulating and solubilizing oleate surface ligands. We exploited the insolubility of EDT treated PbSe NQD films in the processing of multi-layered device stacks. Specifically, we employed a 'sequential spin-casting' method to form PbSe NQD active layers based on repeated cycles of NQD spin-casting and EDT treatment (Appendix A). This approach provided robust, crack-free NQD active layer film and the experimental control required to fabricate the NQD film with carefully tuned thicknesses. Completed devices were tested under 100 mW/cm^2 AM1.5 illumination. To ensure consistency and reproducibility, we fabricated our test structures two to three times with six working solar cells on each device. Devices based on 1.2 nm PbSe NQD were fabricated only once. To focus on the intrinsic characteristics of the NQD active layer and to decouple effects of film thickness from the device V_{oc}, the present work concentrated on thin (40 - 50 nm) NQD active layers, well below the effective exciton diffusion length of about 100 nm recently reported by Nozik and co-workers. [9] To confirm that the photovoltage of our devices was not limited by diffusion through the active layer, we compared current-voltage characteristics of devices with 40- and 80 nm thick PbSe NQD films and found that V_{oc} is identical for both devices while the thicker 80 nm film gives slightly higher current density (Appendix A). The lack of a correlation between V_{oc} and film thickness used in our devices confirms that recombination in the thin NQD active layers of our test structure does not obscure the correlation between photovoltage and interfacial energy level offset.

Efficient transfer of photogenerated holes and electrons requires charge collection layers with good conductivity. The PEDOT:PSS, hole transport layer is already highly doped, but the as-deposited ZnO nanoparticle layer initially showed low conductivity. The conductivity of the ZnO nanoparticle layer can be easily improved through UV photodoping which is believed to passivate electron traps on the ZnO surface [44, 45]. We exploited the photodoping of ZnO to test the structural and electrical integrity of our device stack. Prior to UV exposure, the devices showed low current and low rectification, which indicates that direct metal/NQD Schottky contacts were successfully avoided (Appendix A) [8-10]. Conversely, cracks in the ZnO film and direct Al/ PbSe NQD contacts would have resulted in rectifying Schottky junctions with measurable photovoltage without UV exposure. In our test structure, rectification and photovoltage are only observed after the ZnO layer is ‘activated’ through photodoping. This observation confirms the role the ZnO layer in the extraction of photogenerated electrons from the PbSe NQD layer and allows us to directly attribute the measured open circuit voltages to the performance of the PEDOT:PSS/PbSe NQDs/ZnO device stack. Additional control experiments of devices fabricated without the ZnO electrode layer confirm the reduced V_{oc} of Schottky junction devices with direct NQD/metal contacts (Appendix A).

Having ruled out the possibility of major electronic perturbation to PbSe NQD associated with the Schottky junction, we can directly correlate the size-dependent energy levels with photovoltaic device performance. Figure 3.3 shows the photovoltaic performance of devices fabricated from PbSe NQD with diameter ranging from 1.2 nm to 6.5 nm. The current-voltage characteristics of the devices show two distinctive performance domains. Devices based on large (d > ~3.5 nm) PbSe NQD show negligible open circuit voltages (V_{oc}) and almost no rectification (Figure 3.3B). On the other hand, devices made with smaller (d < ~3.5 nm) PbSe NQD show strong rectification and a linear correlation between V_{oc} and NQD diameter. These two distinct J-V domains verify the role of tunable energy offsets at the PbSe NQD/ZnO and PbSe NQD/PEDOT:PSS interfaces in the photovoltaic effect of our devices. Importantly, the device data show cross-over between the two domains to occur at NQD diameter of approximately 4 nm. This threshold is generally consistent with the critical diameter (d ~4.5 nm) predicted by the CV data in Figure 3.1. Beyond experimental error inherent to the electrochemical, optical and photovoltaic measurements, we attribute the minor disagreement to possible shifts in energy level offset during device fabrication and the minimum energy level offset required to drive the interfacial charge transfer (*vide infra*). The relative contribution of each of these factors is currently under investigation.

The presence of two distinct device performance domains also confirms the absence of Schottky junction which, due to the metal induced depletion region, would have exhibited a linear trend in photovoltage for all NQD diameters [9]. Moreover, the absence of the Schottky junction is consistent with expectation that both PEDOT/PbSe nor PbSe/ZnO interfaces lack the number of free carriers to form a depletion region [46]. With similar reasoning, we do not consider the conventional p-n junction to be main source of the photovoltaic effect of our devices.

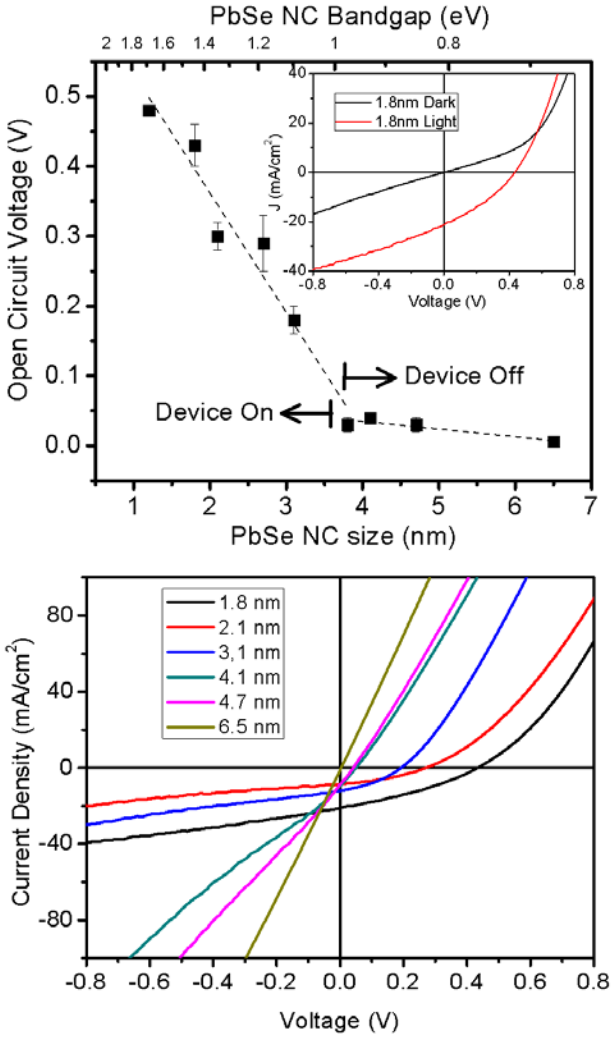

Figure 3.3: (A) Open circuit voltages from devices (V_{oc}) with various PbSe NQD sizes. Two distinctive domains are observed. Devices made from large (d > ~3.8 nm) NQDs show no appreciable photovoltaic effect whereas devices made from small (d < ~3.8 nm) NQDs show increasing V_{oc} with decreasing NQD size. The critical diameter (~ 4 nm), that defines the transition between the ‘linear’ and ‘off’ domains, agrees reasonably with the CV result. The linear fits (dotted lines) to the respective domains are used to gain information on the minimum interfacial energy level offset required for charge separation in our devices (more detailed discussion in the text). The inset shows J-V curve of the best performing device. (B) J-V curves of representative devices in 100 mW/cm^2 AM1.5 light, illustrating the trend of better rectification with smaller NQDs.

3.4 Discussion and Conclusion

Instead of Schottky or p-n junction, the underlying photovoltaic mechanism of our NQD-based photovoltaic devices is that of excitonic solar cell or the ‘kinetic model’ described by Gregg [23, 24]. The V_{oc} in our devices is manifestation of asymmetric kinetics of competing exciton dissociation processes at the PbSe NQD/ZnO and PbSe NQD/PEDOT interfaces. It has been measured that the rate of electron injection from NQD to electron acceptor, such as TiO_2, increases over several orders of magnitude faster with increasing energy level offset between the LUMO of NQD and the LUMO of electron acceptors [15, 47]. This trend is consistent with Marcus theory [48] which implies that logarithm of the electron transfer rate is a quadratic function with respect to the driving force, -Δ*G*. In our device, increasing energy level offsets between PbSe NQD/ZnO and PbSe NQD/PEDOT:PSS interfaces (-Δ*G* for electron transfer reaction in our device) is expected to lead to orders of magnitude faster rate of electron (hole) transfer into ZnO (PEDOT:PSS). Conversely, the transfer rate of the opposite charge is predicted to drop correspondingly. Taken together, we can explain the increasing V_{oc} of our devices with increasing interfacial energy level offset based on the differences in photoinduced chemical potential energy gradients generated by the highly asymmetric electron and hole transfer rates (Figure 3.4A). The direct correlation of V_{oc} and NQD-size tunable interfacial energy level offset (Figure 3.3A) suggests that the device V_{oc} is a linear function of logarithm of charge transfer rate. Further experiments to quantitatively relate asymmetric charge transfer rates with photovoltaic device performance are currently under way.

The critical NQD diameter defining the transition between the favorable and unfavorable energetic landscapes for interface charge transfer provides a direct metric for comparison of the electrochemical (Figure 3.1) and photovoltaic (Figure 3.3) measurements. Based on the intersection of linear fits to two distinct photovoltaic device performance domains in Figure 3.3, we determined the critical PbSe NQD diameter as 3.8 nm. The small discrepancy between the critical diameters determined by electrochemical and photovoltaic measurements suggests that the minimum energy level offset required for charge separation in excitonic NQD solar cells is small. Although an accurate assessment of the minimum energy level offset is, at present, blurred by experimental errors associated with the cyclic voltammetry, possible energy level shifts accompanying surface chemistry treatments during device processing and the inherent relative size distribution (~10%) of the NQD ensemble, we point out that the agreement of the two complementary approaches taken this work is consistent with predictions based on the small exciton binding energy prevailing in inorganic semiconductors [49]. By contrast, interfacial charge transfer across heterojunctions in organic photovoltaics is significantly influenced by strong exciton binding energies which typically require ~ 0.5 V interfacial energy level offset to accomplish exciton dissociation [50].

We fabricated a number of control devices to verify the excitonic solar cell mechanism and better understand the role of photoinduced chemical potential gradient at the ZnO/PbSe interface. In one configuration, we deliberately formed a Schottky junction by integrating 2.1 nm PbSe NQD into a ITO/ZnO/PbSe NQD/Al device stack. In the dark, this Schottky diode should exhibit forward rectification dominated by the PbSe NQD/Al heterojunction. On the other hand, under illumination, the device should exhibit asymmetric charge separation kinetics at the ZnO/PbSe NQD interface. Electron transfer from PbSe NQD to the underlying ZnO layer (instead of Al) should therefore lead to a photoinduced chemical potential energy gradient which reduces or even reverses the rectification of the device. Our test structures indeed show light induced polarity switch in diode rectification (Figure 3.4B). In dark, the device behaved like a forward diode with positive rectification ratio at +/- 1 V. When illuminated with 100 mW/cm^2 light, the rectification became nearly zero at +/- 1V. With increased light intensity of 150 mW/cm^2, the device then exhibited reverse diode behavior with negative rectification ratio at +/- 1 V. This rectification polarity switch was fully reversible by turning the light on and off. The light induced diode polarity switch confirms that the photoinduced electrochemical potential gradient at ZnO/PbSe NQD is significant enough to overcome the internal electric field imposed by the Schottky junction at NQD/Al interface and the electrode workfunction difference. Importantly, this control experiment testifies to the role of chemical potential energy gradient as one of the main driving forces of charge separation, in accordance with the kinetic model suggested by Gregg [23, 24], and serves as a strong evidence for excitonic solar cell mechanism of our devices – no other conventional device mechanisms can account for such behavior.

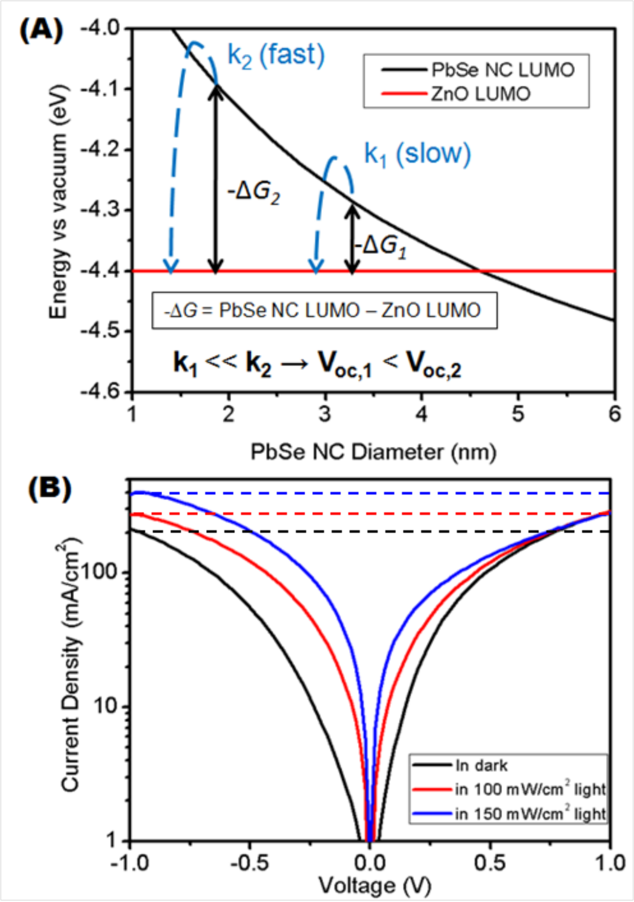

Figure 3.4: (A) Schematic illustrating the effect of interfacial energy level offset on electron transfer rates. According to Marcus theory, the interfacial energy level offsets, which are the driving force $-\Delta G$ of the electron transfer reaction, result in orders of magnitude difference in electron transfer rates. Open circuit voltages of our devices showed a direct correlation to magnitude of $-\Delta G$ as well as the sign of $-\Delta G$ (by device turning on and off at the critical NQD size of ~3.5 nm). (B) Light intensity dependent diode polarity switch in control devices based on ITO/ZnO/2.1 nm PbSe NQD/Al structure. The horizontal dotted lines were added to assist illustrating the rectification ratio at +/- 1 V. The polarity switch was fully reversible by turning light on and off.

The best performing device (with 2 nm PbSe NQD) showed V_{oc} = 0.44 V, J_{sc} = 24 mA/cm^2, fill factor = 0.32 and efficiency of 3.4 % under 100 mW/cm^2 AM1.5 illumination (Figure 3.3A inset). This was the highest efficiency obtained with PbSe NQD based photovoltaics at the time of publication of the paper and shows that designing excitonic solar cell device structure can improve lead salt NQD device performance significantly. We emphasize that the device structure has not yet been optimized for processing or structural aspects of the active layer. We also point out that the fitting of our best device J-V characteristics with generalized Shockley diode equation gives high ideality factor of 9 and low parallel resistance of 170 Ω cm^2. Such values are far from ideal diode characteristics, much worse than values typically obtained from organic excitonic solar cell materials [51], and indicate that our present devices suffer from significant leakage current. Moreover, we often observe crossing of the J-V curves in light with the dark J-V curves at low (< 0.5 V) voltages in our devices, indicating the presence dominant interfacial recombination [52]. Thus, there is much room for improvement in device performance beyond initial efficiency of 3.4% by optimizing structure and thickness of active layer while reducing leakage current and interfacial recombination. We also note that our choice of the PbSe NQD, ZnO and PEDOT:PSS was not motivated by achieving high efficiency but rather by designing test structures that enable systematic studies on the effect of interfacial energy level alignment type and offsets on the photovoltaic performance. With insight on the excitonic solar cell mechanism gained from this work, different combination of NQDs and charge transporting layer materials can be chosen to maximize the asymmetry in charge transfer rates and thereby achieve higher efficiency.

In conclusion, we have fabricated PbSe NQD based solar cells that operate on the excitonic solar cell mechanism. These structures allow probing of intrinsic electronic and photovoltaic properties of PbSe NQD. We demonstrated a direct correlation of NQD size tunable heterojunction energy level offsets with the photovoltaic device V_{oc} and illustrated excitonic solar cell behavior of our devices where kinetics of charge transfer mainly determine the device V_{oc}. Initial devices achieve high efficiencies, showing the potential of lead salt NQD photovoltaics. Going beyond the new insights gained from this work, deeper understanding of issues regarding the charge separation mechanism, effect of charge separation rates on device performance, role of NQD surface ligands and etc, may allow us to tap into the potential of NQD as next generation photovoltaic material and achieve efficient and inexpensive NQD based solar cells that are economically viable for wide spread deployment.

BIBLIOGRAPHY

[1] J. J. Choi, Y.-F. Lim, M. B. Santiago-Berrios, M. Oh, B.-R. Hyun, L. Sun, A. C. Bartnik, A. Goedhart, G. G. Malliaras, H. D. Abruna, F. W. Wise, T. Hanrath, Nano Letters. **9**, 3749 (2009).

[2] C. M. Evans, L. Guo, J. J. Peterson, S. Maccagnano-Zacher, T. D. Krauss, Nano Letters. **8**, 2896 (2008).

[3] A. G. Kanaras, C. Sonnichsen, H. Liu, A. P. Alivisatos, Nano Letters. **5**, 2164 (2005).

[4] C. B. Murray, C. R. Kagan, M. G. Bawendi, Annual Review of Materials Science. **30**, 545 (2000).

[5] D. V. Talapin, J. H. Nelson, E. V. Shevchenko, S. Aloni, B. Sadtler, A. P. Alivisatos, Nano Letters. **7**, 2951 (2007).

[6] F. W. Wise, Accounts of Chemical Research. **33**, 773 (2000).

[7] W. W. Yu, J. C. Falkner, B. S. Shih, V. L. Colvin, Chemistry of Materials. **16**, 3318 (2004).

[8] G. I. Koleilat, L. Levina, H. Shukla, S. H. Myrskog, S. Hinds, A. G. Pattantyus-Abraham, E. H. Sargent, ACS Nano. **2**, 833 (2008).

[9] J. M. Luther, M. Law, M. C. Beard, Q. Song, M. O. Reese, R. J. Ellingson, A. J. Nozik, Nano Lett. **8**, 3488 (2008).

[10] W. Ma, J. M. Luther, H. Zheng, Y. Wu, A. P. Alivisatos, Nano Letters. **9**, 1699 (2009).

[11] I. Gur, N. A. Fromer, M. L. Geier, A. P. Alivisatos, Science. **310**, 462 (2005).

[12] Y. Wu, C. Wadia, W. Ma, B. Sadtler, A. P. Alivisatos, Nano Letters. **8**, 2551 (2008).

[13] W. U. Huynh, J. J. Dittmer, A. P. Alivisatos, Science. **295**, 2425 (2002).

[14] X. Jiang, R. D. Schaller, S. B. Lee, J. M. Pietryga, V. I. Klimov, A. A. Zakhidov, Journal of Materials Research. **22**, 2204 (2007).

[15] B.-R. Hyun, Y.-W. Zhong, A. C. Bartnik, L. Sun, H. D. Abruna, F. W. Wise, J. D. Goodreau, J. R. Matthews, T. M. Leslie, N. F. Borrelli, ACS Nano. **2**, 2206 (2008).

[16] I. Robel, V. Subramanian, M. Kuno, P. V. Kamat, Journal of the American Chemical Society. **128**, 2385 (2006).

[17] P. Yu, K. Zhu, A. G. Norman, S. Ferrere, A. J. Frank, A. J. Nozik, The Journal of Physical Chemistry B. **110**, 25451 (2006).

[18] A. Zaban, O. I. Micic, B. A. Gregg, A. J. Nozik, Langmuir. **14**, 3153 (1998).

[19] J. M. Luther, M. Law, Q. Song, C. L. Perkins, M. C. Beard, A. J. Nozik, ACS Nano. **2**, 271 (2008).

[20] D. V. Talapin, C. B. Murray, Science. **310**, 86 (2005).

[21] M. C. Beard, A. G. Midgett, M. Law, O. E. Semonin, R. J. Ellingson, A. J. Nozik, Nano Letters. **9**, 836 (2009).

[22] T. Hanrath, D. Veldman, J. J. Choi, C. G. Christova, M. M. Wienk, R. A. J. Janssen, ACS Applied Materials & Interfaces. **1**, 244 (2009).

[23] B. A. Gregg, The Journal of Physical Chemistry B. **107**, 4688 (2003).

[24] B. A. Gregg, M. C. Hanna, Journal of Applied Physics. **93**, 3605 (2003).

[25] J. Nelson, The Physics of Solar Cells, Imperial College Press, London, 2003.

[26] Scharber, D. Mulbacher, M. Koppe, P. Denk, C. Waldauf, A. Heeger, C. Brabec, Advanced Materials. **18**, 789 (2006).

[27] R. J. Ellingson, M. C. Beard, J. C. Johnson, P. Yu, O. I. Micic, A. J. Nozik, A. Shabaev, A. L. Efros, Nano Letters. **5**, 865 (2005).

[28] A. J. Nozik, Physica E: Low-dimensional Systems and Nanostructures. **14**, 115 (2002).

[29] R. D. Schaller, V. I. Klimov, Physical Review Letters. **92**, 186601 (2004).

[30] M. Ben-Lulu, D. Mocatta, M. Bonn, U. Banin, S. Ruhman, Nano Letters. **8**, 1207 (2008).

[31] M. Ji, S. Park, S. T. Connor, T. Mokari, Y. Cui, K. J. Gaffney, Nano Letters. **9**, 1217 (2009).

[32] J. A. McGuire, J. Joo, J. M. Pietryga, R. D. Schaller, V. I. Klimov, Accounts of Chemical Research. **41**, 1810 (2008).

[33] G. Nair, M. G. Bawendi, Physical Review B (Condensed Matter and Materials Physics). **76**, 081304 (2007).

[34] V. Sukhovatkin, S. Hinds, L. Brzozowski, E. H. Sargent, Science. **324**, 1542 (2009).

[35] M. T. Trinh, A. J. Houtepen, J. M. Schins, T. Hanrath, J. Piris, W. Knulst, A. P. L. M. Goossens, L. D. A. Siebbeles, Nano Letters. **8**, 1713 (2008).

[36] J. M. An, A. Franceschetti, S. V. Dudiy, A. Zunger, Nano Letters. **6**, 2728 (2006).

[37] I. Kang, F. W. Wise, Journal of the Optical Society of America B. **14**, 1632 (1997).

[38] K. Overgaag, P. Liljeroth, B. Grandidier, D. Vanmaekelbergh, ACS Nano. **2**, 600 (2008).

[39] L. E. Brus, The Journal of Chemical Physics. **79**, 5566 (1983).

[40] A. Hagfeldt, M. Graetzel, Chemical Reviews. **95**, 49 (1995).

[41] J. Huang, P. F. Miller, J. S. Wilson, A. J. deMello, J. C. deMello, D. D. C. Bradley, Advanced Functional Materials. **15**, 290 (2005).

[42] H.-L. Yip, S. K. Hau, N. S. Baek, H. Ma, A. K. Y. Jen, Advanced Materials. **20**, 2376 (2008).

[43] W. J. E. Beek, M. M. Wienk, M. Kemerink, X. Yang, R. A. J. Janssen, The Journal of Physical Chemistry B. **109**, 9505 (2005).

[44] J. Gilot, M. M. Wienk, R. A. J. Janssen, Applied Physics Letters. **90**, 143512 (2007).

[45] F. Verbakel, S. C. J. Meskers, R. A. J. Janssen, Journal of Applied Physics. **102**, 083701 (2007).

[46] M. Shim, P. Guyot-Sionnest, Nature. **407**, 981 (2000).

[47] I. Robel, M. Kuno, P. V. Kamat, Journal of the American Chemical Society. **129**, 4136 (2007).

[48] R. A. Marcus, The Journal of Chemical Physics. **43**, 679 (1965).

[49] R. W. Meulenberg, J. R. I. Lee, A. Wolcott, J. Z. Zhang, L. J. Terminello, T. van Buuren, ACS Nano. **3**, 325 (2009).

[50] X. Y. Zhu, Q. Yang, M. Muntwiler, Acc. Chem. Res. **42**, 1779 (2009).

[51] B. P. Rand, D. P. Burk, S. R. Forrest, Physical Review B (Condensed Matter and Materials Physics). **75**, 115327 (2007).

[52] J. Nelson, J. Kirkpatrick, P. Ravirajan, Physical Review B. **69**, 035337 (2004).

CHAPTER 4

TUNABLE ENERGY LEVELS: NANOCRYSTAL QUANTUM DOT TANDEM SOLAR CELLS[1]

4.1 Introduction

As we discussed in chapter 3, intensive research efforts continue to provide important insights into the complex relationship between the coupled sub-processes of light absorption, exciton dissociation, and charge transport across multiple nanostructured interfaces in NQD solar cells. Beyond their application in conventional thin-film low-cost solar cells, NQDs also offer exciting prospects for the realization of third-generation photovoltaics with conversion efficiencies beyond the Shockley-Queisser limit [2, 3]. Recent reports of hot carrier [4] and multiple carrier [5] extraction from photoexcited NQDs highlight the potential of NQDs in high-performance solar cells. However, many daunting constraints, in particular regarding the charge extraction dynamics, need to be resolved before these discoveries can be translated to prototype photovoltaic devices [6]. An alternative approach to breaching the single-junction efficiency limit – the focus of this communication – is to create multijunction solar cells composed of distinct absorber layers with cascaded energy gaps. Advances in thin film growth via molecular beam epitaxy have enabled

---

[1] The results presented in this chapter have been published in Ref [1].

the creation of complex multijunction structures with efficiencies exceeding 40% [7]. Unfortunately, high fabrication costs have thus far limited the broad deployment of this technology.

The prospect of solution-processed NQD-based multi-junction solar cells introduces exciting opportunities for realizing high-conversion efficiency in low-cost device structures. Here we report the first tandem solar cells (at the time of the publication) produced from colloidal suspensions of size-tuned semiconductor NQDs. Related studies of organic multijunction cells have illustrated the importance of understanding and designing the optical absorption profile throughout the device stack and the charge transport characteristics of the interlayer [8-13]. The interlayer connecting the front and back cell must meet several stringent optical and electrical constraints: first, it should be optically transparent to pass light to the underlying cell; second, it must provide appropriate energy level alignment to accept electrons and holes from the subcells and efficiently recombine them without degrading the overall photovoltage of the cell. The interlayers in the best performing organic tandem cells reported so far are based on junctions between an n-type metal oxide layer and a p-type poly(3,4-ethylenedioxythiophene) poly(styrenesulfonate) (PEDOT:PSS) layer [10, 13]. Here we demonstrate that analogous interlayer structures can be applied to connect NQD-based subcells with specific energy gaps.

4.2 NQD-tandem Cell Fabrication and Characterization

The design of the NQD-tandem cell structure introduced in this report emerged from recent studies on size dependent absolute energy levels of lead salt NQDs [4, 14, 15] and device structures based on heterojunctions between NQD and metal oxide nanoparticle films [14, 16-19]. Lead chalcogenide (PbX; X=S,Se,Te) NQDs are particularly promising for tandem cells since their pronounced quantum confinement effects enable size-tunable energy gaps in the range of 0.4 to 2 eV [20]. This range encompasses the optimal energy gap for a single junction cell (1.2 eV) as well as the optimal gaps for a two-terminal tandem cell (0.94 and 1.61 eV) [21]. Here we prepare size-tuned PbS NQDs with energy gaps in the range of 0.7 eV and 2.0 eV and demonstrate the first NQD tandem cells with an open circuit voltage (V_{oc}) approaching 1V. NQD synthesis, optical characterization, and device fabrication are described in the supplementary information (Appendix B).

Figure 4.1 illustrates a schematic of our NQD tandem solar cell and the proposed energy level landscape. Excitons are photoexcited in the front and back PbS NQD layers and electrons are injected into the ZnO cathode and holes into the PEDOT:PSS anode, as described in previous studies [14, 15]. The two sub-cells are electrically connected with a ZnO/Au (1nm)/pH-neutral PEDOT:PSS interlayer that accepts electrons from the front cell and holes from the back cell and efficiently recombines them. We neutralized the pH of the PEDOT:PSS film by adding NaOH to prevent the acidity of the PEDOT from dissolving the underlying ZnO nanoparticle film [8]. Previous studies have observed a reduction of the PEDOT:PSS workfunction in response to increasing pH values [12, 22]. For reasons discussed below, we found that proper operation of the interlayer required two important modifications: (i) a thin

(1 nm) gold layer, and (ii) a hole acceptor film processed from pH-neutralized PEDOT:PSS.

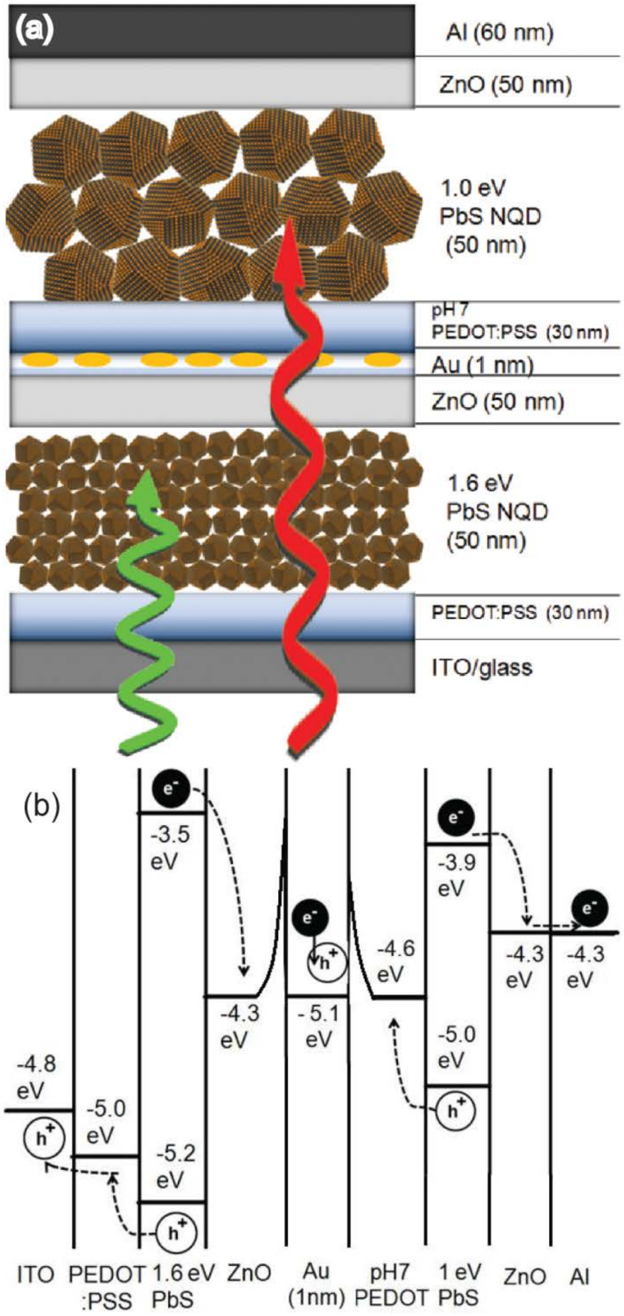

Figure 4.1: (a) Schematic of the proposed tandem cell with optimum combination of PbS NQD bandgaps. (b) Energy level diagram of the tandem device stack. The PbS

NQD layers in the sub-cells are electrically connected by ZnO/Au (1nm)/PEDOT:PSS interlayer where efficient recombination occurs.

The device performance of the NQD tandem cell (Figure 4.2) shows that the V_{oc} of the tandem cell is the sum of the V_{oc} of its sub-cells, which indicates that the interlayer efficiently recombines charges without significant voltage loss. Because the two-terminal tandem cell structure does not allow separate testing of its sub-cells, we fabricated corresponding single junction devices as controls with NQDs from the same synthesis batch prepared under identical film deposition conditions. Optimized tandem cells and corresponding control devices of each subcell were fabricated from 1.6 eV (d_{NC}= 3 nm) and 1.0 eV (d_{NC}= 4.8 nm) PbS NQD films; these size-tuned energy gaps correspond to the optimum theoretical value for a two terminal device [21]. Our best cell had V_{oc} = 0.91±0.02 V, short circuit current density J_{sc} = 3.7±0.1 mA/cm^2, fill factor FF = 0.37±0.01, and a power conversion efficiency PCE = 1.27±0.05%. The control front cell showed V_{oc} = 0.58±0.02 V, J_{sc} = 7.0±0.7 mA/cm^2, FF = 0.44±0.01, and PCE = 1.8±0.2%. The control back cell showed V_{oc}= 0.32±0.02 V, J_{sc} = 9.4±0.4 mA/cm^2, FF = 0.42±0.02 and PCE = 1.26±0.07%.

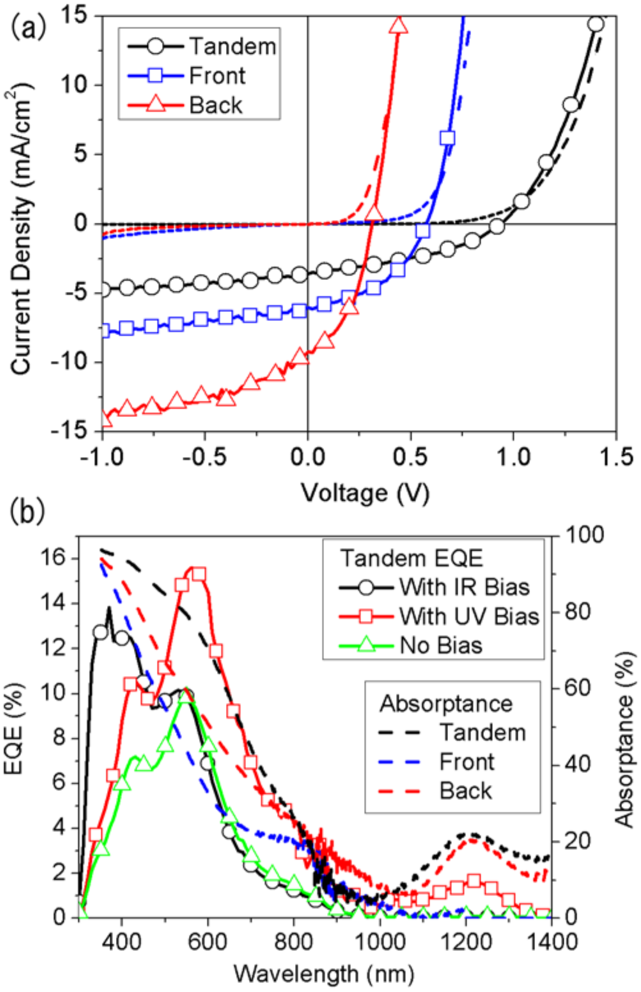

Figure 4.2: (a) J-V characteristic of the tandem cell and corresponding control single junction devices. The tandem cell exhibits open circuit voltage that is a sum of the open circuit voltages of the sub-cells indicating that the interlayer is recombining charges efficiently without voltage loss. (b) External quantum efficiency and absorptance spectra of the devices. Carefully adjusted light bias are required to measure signals from the sub-cells (see the main text for details)

Figure 4.2b shows external quantum efficiency (EQE) of each sub-cell within the champion tandem cell device alongside the absorptance spectra of the corresponding

NQD films in the device stacks. Absorptance measurements of the device stacks were performed using an integrating sphere to account for light scattering. EQE measurements of tandem solar cell structures require special precautions due to the coupled light-absorption and current-generation processes in each cell [23]. EQE measurements were performed with two excitation light sources – an unmodulated optical bias light beam was used to excite only one of the sub-cells while a modulated monochromatic probe light was used to measure the EQE of the other sub-cell (see Appendix B for details) [10, 13, 23]. The EQE spectra closely follow the absorptance spectra of the front and back cells, confirming that the photocurrents are generated from the size-tuned NQDs. The decrease in EQE at short wavelengths arises primarily from parasitic absorption in the ITO and ZnO layers. We are currently investigating the optical electrical field distribution within the device stack to understand how optical interference effects influence the EQE in the visible and to guide further optimization of absorber and interlayer film thickness. To avoid complications related to charge transport limitations in individual cells and to isolate the performance of the interlayer, we limit our studies here to relatively thin (~50 nm) NQD absorber layers. (See Appendix B for the effect of thicker NQD layers on device behavior)

4.3 Effect of Interlayer Workfunction and Conductivity

Efficient recombination in the interlayer is contingent upon proper energy level alignment and sufficient carrier densities. The energy level offset between ZnO and

PEDOT can be mitigated by the incorporation of ultra-thin metal films; this approach has been successfully demonstrated in organic tandem cells [24, 25]. To create efficient interlayers for the NQD tandem cell shown in Figure 4.1, we thermally evaporated a thin (1 nm) Au layer onto the ZnO film, which was followed by spin-coating a pH neutral PEDOT:PSS layer. Scanning electron micrographs show that Au forms few-nanometer sized metal islands instead of a continuous film (Appendix B). Without the Au layer, the current-voltage characteristics of the tandem devices (see Figure 4.3a) exhibited an ‘S-shape’ kink that has previously been attributed to an interfacial barrier for charge transport [26, 27]. Interestingly, the incorporation of either Ag or Al thin films into the interlayers failed to remedy the S-shaped kink in the current-voltage behavior. To delineate the effect of the surface work function and the carrier density, we carried out a series of control experiments discussed below.

We employed Kelvin probe force microscopy (KPFM) to understand how the composition of the metal thin film influences the surface Fermi level of ZnO/M (M=Al, Ag, or Au) layers. A platinum coated AFM tip was used and its workfunction was taken to be 5.65 eV. KPFM results showed that the ZnO surface Fermi level was 4.62 eV and that Au, Ag and Al raise the Fermi level to 5.11 eV, 5.03 eV and 4.98 eV respectively (Figure 4.3b). The run-to-run variation in the KPFM measurements introduced an experimental error of +/- 0.069 eV (see Appendix B for details). The ZnO Fermi level value is consistent with the literature values [28] and the increase in the Fermi level due to Au is also expected considering the 5.1 ~ 5.4 eV workfunction of Au [29]. The rise of surface workfunction of Ag to 5.0 eV has been observed previously and is attributed to oxidation in air [30]. We tentatively attribute the higher-than-expected workfunction of ZnO/Al to the oxidation of Al and its interaction with the ZnO surface. The lack of a statistically significant difference in the Fermi level of the ZnO/M surfaces suggests that the shift in workfunction due to metal composition alone cannot explain the observed trends in interlayer performance.

We isolated the transport characteristics of the interlayer stack by preparing a series of ITO/ZnO/M/PEDOT:PSS/Ag (M=Al, Ag, Au) control devices. This device configuration allowed us to probe how metal composition and photo-doping of the underlying ZnO nanoparticle film influence electrical characteristics of the interlayer. Janssen and co-workers have recently shown that short UV light exposure effectively eliminated S-shaped kinks in organic tandem cell performance [8]; this effect was attributed to increased concentration of mobile electrons [31, 32]. We found that the combination of ultra-thin Au films and UV photo-doping yielded interlayers with Ohmic transport characteristics (Figure 4.3c). Interlayer control devices with ultra-thin Ag or Al films on the other hand exhibit non-linear transport characteristics even after one hour of photo-doping (Appendix B). Addition of an Al thin film to the interlayer increased the series resistance by a factor of 3 compared to no metal or an Au layer. This observation serves as another indication that the Al layer is likely partially oxidized and thus reduces the conductance of interlayer stack. These results, combined with KPFM data, suggest that the metal layer serves to provide enough carriers for proper Fermi level tuning and band bending over a short spatial distance while maintaining conductance for successful interlayer operation.

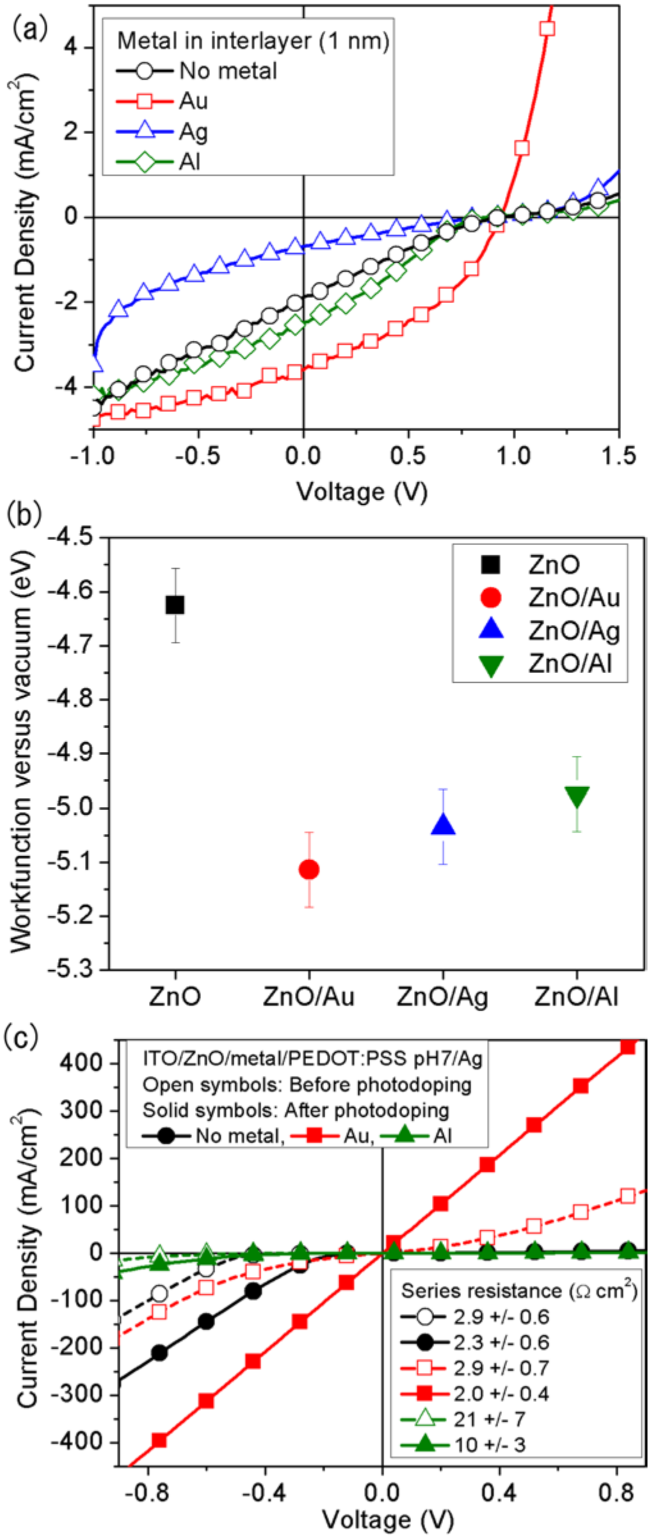

Figure 4.3: (a) Effect of thin (1 nm) metal layer in the interlayer on tandem device performance. The S-shape kink that is attributed to interfacial barrier for charge

transport disappears only when gold layer is inserted. (b) Kelvin probe force microscopy measurement of surface workfunction of the bare ZnO layer and various metals on top. The presence of metal layers increases the surface workfunction. (c) Conductance measurements on the interlayer stacks show that inserting Au layer causes Ohmic junction while inserting Al layer increases series resistance by a factor of 3.

The magnitude of the doping within the ZnO nanoparticle and PEDOT:PSS layers can drastically influence the efficacy of the interlayers. While many studies have been performed on understanding chemical doping in PEDOT:PSS [12, 22, 33], the ZnO nanoparticle layers remain somewhat of an electronic 'black box', despite recent efforts in this area [31, 32]. We found that the magnitude of the photo-doping of ZnO nanoparticle layer is sensitive to the type of ZnO nanoparticles. Specifically, ZnO nanoparticles synthesized with KOH (ZnO:KOH) respond more prominently to photo-doping than ZnO nanoparticles prepared with tetramethylammonium hydroxide (ZnO:TMAH) (Appendix B). While details of the underlying photo-doping mechanism remain unknown, we expect that the chemical and physical properties of the ZnO nanoparticles, which vary depending on the synthesis protocol, influence the density of surface traps, carrier density in the nanoparticle film and hence their response to photo-doping. In the context of interlayer performance, we found that photo-doping in ZnO:KOH nanoparticle films for a few seconds was sufficient to remove the S-shaped kink transport characteristics without the addition of a metal thin film. Janssen and co-workers seem to have achieved Ohmic junctions for their devices via UV doping of the ZnO:KOH nanoparticle layer which led to just enough band bending over a short space-charge layer length to allow for efficient tunneling of electrons through the barrier [31, 32]. In contrast, the ZnO:TMAH nanoparticle film could not obtain high enough carrier density with photodoping alone. Instead, the addition of a thin Au layer was required to achieve additional carriers and efficient charge recombination. Notably, NQD tandem devices fabricated with layers of ZnO:KOH nanoparticles exhibited worse device performances than devices fabricated with ZnO:TMAH, owing largely to lower photocurrent and fill-factor (Appendix B). These results corroborate our assertion that different types of surface states, electron mobilities, and/or carrier concentrations arise depending on the ZnO nanoparticle synthesis method.

4.4 Conclusion

In conclusion, we have exploited the quantum confinement of PbS NQDs to develop the first solution processed NQD tandem solar cells. The prototype devices, which feature interconnected NQD layers of cascaded energy gaps, exhibit IR sensitivity and a V_{oc} approaching 1V. The nature of the interconnect layers has a drastic effect on the output characteristics of the tandem devices. We investigated a variety of interlayer configurations and showed that ZnO/Au/PEDOT:PSS stacks possess the appropriate carrier density and energy-level alignment to efficiently connect NQD absorber layers. The advances presented in this communication provide guidelines for the design of an effective interlayer in solution processed tandem cell devices and suggest a promising future for NQD tandem solar cells.

BIBLIOGRAPHY

[1] J. J. Choi, W. N. Wenger, R. S. Hoffman, Y.-F. Lim, J. Luria, J. Jasieniak, J. A. Marohn, T. Hanrath, Advanced Materials. **23**, 3144 (2011).

[2] A. Nozik, Physica E. **14**, 115 (2002).

[3] W. Shockley, H. J. Queisser, J. Appl. Phys. **32**, 510 (1961).

[4] W. A. Tisdale, K. J. Williams, B. A. Timp, D. J. Norris, E. S. Aydil, X. Y. Zhu, Science. **328**, 1543 (2010).

[5] J. B. Sambur, T. Novet, B. A. Parkinson, Science. **330**, 63 (2010).

[6] O. E. Semonin, J. M. Luther, S. Choi, H.-Y. Chen, J. Gao, A. J. Nozik, M. C. Beard, Science. **334**, 1530 (2011).

[7] A. Barnett, D. Kirkpatrick, C. Honsberg, D. Moore, M. Wanlass, K. Emery, R. Schwartz, D. Carlson, S. Bowden, D. Aiken, A. Gray, S. Kurtz, L. Kazmerski, T. Moriarty, M. Steiner, J. Gray, T. Davenport, R. Buelow, L. Takacs, N. Shatz, J. Bortz, O. Jani, K. Goossen, F. Kiamilev, A. Doolittle, I. Ferguson, B. Unger, G. Schmidt, E. Christensen, D. Salzman, 22nd European Photovoltaic Solar Energy Conference, Milan, Italy, 2007.

[8] J. Gilot, M. M. Wienk, R. A. J. Janssen, Appl. Phys. Lett. **90**, 143512 (2007).

[9] A. Hadipour, B. de Boer, P. W. M. Blom, Adv. Funct. Mater. **18**, 169 (2008).

[10] J. Y. Kim, K. Lee, N. E. Coates, D. Moses, T.-Q. Nguyen, M. Dante, A. J. Heeger, Science. **317**, 222 (2007).

[11] S. J. Kim, W. J. Kim, A. N. Cartwright, P. N. Prasad, Appl. Phys. Lett. **92**, 191107 (2008).

[12] D. J. D. Moet, P. de Bruyn, P. W. M. Blom, Appl. Phys. Lett. **96**, 153504 (2010).

[13] S. Sista, M.-H. Park, Z. Hong, Y. Wu, J. Hou, W. L. Kwan, G. Li, Y. Yang, Adv. Mater. **22**, 380 (2010).

[14] J. J. Choi, Y.-F. Lim, M. E. B. Santiago-Berrios, M. Oh, B.-R. Hyun, L. Sun, A. C. Bartnik, A. Goedhart, G. G. Malliaras, H. D. Abruña, F. W. Wise, T. Hanrath, Nano Lett. **9**, 3749 (2009).

[15] B.-R. Hyun, Y.-W. Zhong, A. C. Bartnik, L. Sun, H. D. Abruña, F. W. Wise, J. D. Goodreau, J. R. Matthews, T. M. Leslie, N. F. Borrelli, ACS Nano. **2**, 2206 (2008).

[16] G. I. Koleilat, L. Levina, H. Shukla, S. H. Myrskog, S. Hinds, A. G. Pattantyus-Abraham, E. H. Sargent, ACS Nano. **2**, 833 (2008).

[17] K. S. Leschkies, T. J. Beatty, M. S. Kang, D. J. Norris, E. S. Aydil, ACS Nano. **3**, 3638 (2009).

[18] J. M. Luther, J. Gao, M. T. Lloyd, O. E. Semonin, M. C. Beard, A. J. Nozik, Adv. Mater. **22**, 3704 (2010).

[19] A. G. Pattantyus-Abraham, I. J. Kramer, A. R. Barkhouse, X. Wang, G. Konstantatos, R. Debnath, L. Levina, I. Raabe, M. K. Nazeeruddin, M. Grätzel, E. H. Sargent, ACS Nano. **4**, 3374 (2010).

[20] F. W. Wise, Acc. Chem. Res. **33**, 773 (2000).

[21] A. S. Brown, M. A. Green, Physica E. **14**, 96 (2002).

[22] M. M. de Kok, M. Buechel, S. I. E. Vulto, P. van de Weijer, E. A. Meulenkamp, S. H. P. M. de Winter, A. J. G. Mank, H. J. M. Vorstenbosch, C. H. L. Weijtens, V. van Elsbergen, Phys. Status Solidi A. **201**, 1342 (2004).

[23] J. Gilot, M. M. Wienk, R. A. J. Janssen, Adv. Funct. Mater. **20**, 3904 (2010).

[24] A. Yakimov, S. Forrest, Appl. Phys. Lett. **80**, 1667 (2002).

[25] A. Hadipour, B. De Boer, J. Wildeman, F. B. Kooistra, J. C. Hummelen, M. G. R. Turbiez, M. M. Wienk, R. A. J. Janssen, P. W. M. Blom, Adv. Funct. Mater. **16**, 1897 (2006).

[26] A. Kumar, S. Sista, Y. Yang, J. Appl. Phys. **105**, 094512 (2009).

[27] J. Gao, J. M. Luther, O. E. Semonin, R. J. Ellingson, J. Nozik Arthur, M. C. Beard, Nano Lettes 1 (2011).

[28] R. K. Swank, Phys. Rev. **153**, 844 (1967).

[29] H. B. Michaelson, J. Appl. Phys. **48**, 4729 (1977).

[30] M. S. White, D. C. Olson, S. E. Shaheen, N. Kopidakis, D. S. Ginley, Appl. Phys. Lett. **89**, 143517 (2006).

[31] F. Verbakel, S. C. J. Meskers, R. A. J. Janssen, Appl. Phys. Lett. **89**, 102103 (2006).

[32] G. Lakhwani, R. F. H. Roijmans, A. J. Kronemeijer, J. Gilot, R. A. J. Janssen, S. C. J. Meskers, J. Phys. Chem. C. **114**, 14804 (2010).

[33] C. H. L. Weijtens, V. van Elsbergen, M. M. de Kok, S. H. P. M. de Winter, Org. Electron. **6**, 97 (2005).

CHAPTER 5

TUNABLE COUPLING: INTER-NQD COUPLING INDUCED PHOTOGENERATED EXCITON DISSOCIATION[1]

5.1 Introduction

The performance of most of the proposed NQD technologies depends not only on the properties of the individual NQDs, but equally on the properties arising from interactions between the NQDs in the assembly where NQDs can be regarded as ‘artificial atoms’ which assemble to form ‘artificial solids’ [2]. As in the analogous atomic crystals, the collective interactions among NQDs in the artificial solids are strongly influenced by not just the NQD energy levels but, equally importantly, by the coupling between NQDs.

In contrast to the rapidly growing knowledge base on the properties of individual NQDs, the understanding of the coupling between NQDs is far less developed. NQD solar cells provide an illustrative example of this knowledge gap. The surge of interest in NQD photovoltaics has led to many encouraging results with size-tunable voltages and remarkably high current densities [3-6]. However, the complex sub-processes of exciton dissociation and free carrier transport at the level of an individual NQD and macroscopic charge transfer through the NQD film to the external electrodes are still

---

[1] The results presented in this chapter have been published in Ref [1].

not fully understood. While analogies to charge separation at bulk semiconductor interfaces such as Schottky junctions [3, 6] or NQD/acceptor type II heterojunctions [4, 5] have provided important initial insights, these models do not capture the complex physics and chemistry governing charge transfer across nanostructured interface at the NQD boundary. To understand exciton dissociation in an NQD assembly at the *microscopic* level, we should consider the inter-NQD electronic coupling and exciton binding energies, which govern exciton energy transfer [7, 8], exciton dissociation, exciton formation, and charge transport [9] in the NQD assembly. Exciton binding energy can be tuned by changing NQD size but is largely an intrinsic property of the NQD itself [10, 11] whereas inter-NQD coupling energy can be tuned by altering the inter-NQD separation distance.

Here we report studies of exciton dissociation in strongly coupled NQD films. We combined transient photoluminescence (tPL) and time resolved electric force microscopy (tr-EFM) to probe optical and electrical signatures of the relationship between inter-NQD coupling and photogenerated exciton dissociation in close packed lead salt NQD films. Using variable length alkyl and benzene dithiol linkers, we formed close packed NQD assemblies with tuned inter-NQD separation distance, which was measured using synchrotron based grazing incidence small angle X-ray scattering (GISAXS). Our results show that exciton lifetimes decrease exponentially with decreasing inter-NQD distance. We distinguished between exciton dissociation and competitive de-excitation pathways (e.g., charge transfer to the ligand or surface trapping) through a series of control experiments. We employed tr-EFM to show that the quenched excitons in fact result in free carrier generation in the NQD assemblies.

The correlation between inter-NQD spacing and charge transfer rate shows single exponential decay behavior, indicating that the exciton separation occurs through coupling induced tunneling between neighboring NQDs.

5.2 Tuning inter-NQD separation distance using variable linker molecules

As one of the most strongly quantum confined systems [12], lead salt NQDs naturally provide an ideal experimental testbed for the study of the relationship between inter-NQD coupling and exciton separation mechanism. Inter-NQD coupling energy between close packed lead salt NQDs has previously been measured to be in the range of tens of meV [13, 14], which is comparable to the exciton binding energy of around ~ 100 meV [10]. The high coupling energy and low exciton binding energy in lead salt NQDs, compared to other materials, originate from their strong quantum confinement that allows significant leakage of the electronic wavefunction out of NQD and a high dielectric constant that screens the Coulomb attraction. In contrast, in other NQD system, e.g., cadmium salts, the coupling energy is much smaller than the exciton binding energy and consequently resonant energy transfer acts as the dominant pathway for photogenerated excitons without involving exciton dissociation [8]. Whether the fate of photogenerated excitons is charge dissociation or energy transfer has major implications on opto-electronic device performance. Our findings explain why lead salt Schottky devices [6] give two orders of magnitude higher short-circuit currents than similarly prepared cadmium salt Schottky devices [6, 15], while cadmium salt NQDs show high performance in LED devices [16].

We used 2.7 nm diameter PbS NQDs synthesized via the hot injection method [17] and characterized with absorbance, photoluminescence and transmission electron microscopy. Detailed NQD synthesis procedures are given in Appendix C. As-synthesized NQDs were deposited on cleaned glass substrates via spin-coating or drop-casting to form close packed NQD assemblies. We adjusted the inter-NQD separation distance using variable length bi-linker dithiol ligands such as 1,2-ethanedithiol (EDT), 1,4-benzenedithiol (BDT), 4,4′-dibenzenedithol (DBDT) and 4,4″-tribenzenedithiol (TBDT) (Figure 5.1a). We denote the NQD assemblies treated with the bi-linker molecules as PbS_nBDT where *n* identifies the number of benzene rings (*n* = 0 for EDT, *n* =1 for BDT, *n* = 2 for DBDT, *n* = 3 for TBDT). We specifically chose bi-linker molecules comprised of phenyl rings since they possess only a torsional degree of freedom, to first approximation [18]; their rigidity allows us to precisely tune the inter-NQD separation distance. Moreover, the bi-linker nBDT molecules used in this study have HOMO-LUMO levels that are energetically unfavorable for direct NQD-to-ligand charge transfer [19] (see density functional theory calculation of nBDT HOMO-LUMO levels shown in Appendix C). Detailed sample preparation procedures are explained in the Appendix C.

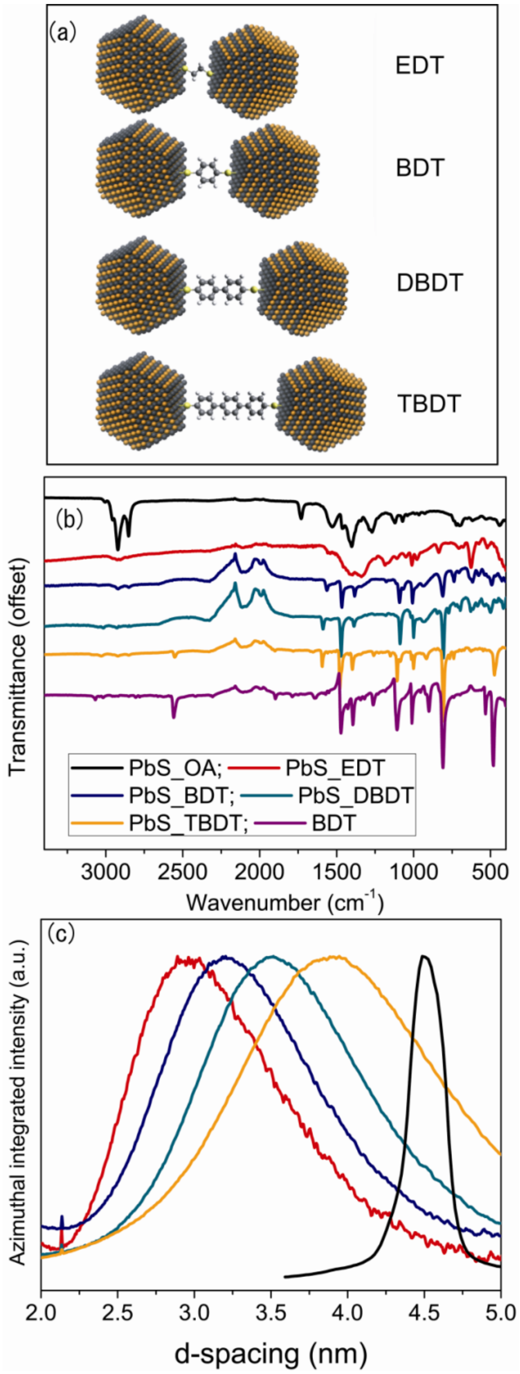

Figure 5.1: (a) Schematic of NQDs linked with various bi-linker molecules used for this study. (b) FTIR spectroscopy characterization of the samples showing the reduction of the C-H stretch peak near 2900 cm^{-1} and the emergence of an aromatic C=C stretch peak near 1500 cm^{-1} after treatment with the bi-linker molecules. The

absence of an S-H peak near 2600 cm^{-1} in dithiol-treated samples indicates that most of the sulfur atoms are bound to the NQD surface. The spectral signatures near 2200 cm^{-1} are due to the presence of CO_2 in the sampling environment. (c) Synchrotron based GISAXS shows a trend of longer inter-NQD distance with NQD assemblies treated with longer bi-linker molecule (same color legend as Figure 5.1b). Each additional benzene ring in the chain of bi-linker molecule results in ~0.3 nm larger average inter-NQD distance.

We monitored NQD surface chemistry before and after the ligand exchange using FTIR spectroscopy. The data in Figure 5.1b illustrate the extent of replacement of oleic acid ligands with dithiol ligands. The most prominent feature is the reduction of aliphatic C-H stretching peaks near 2900 cm^{-1} and emergence of aromatic C=C stretching peaks near 1500 cm^{-1}. These results show that bi-linker molecules with thiol functional group readily replace the long chain alkyl ligands with carboxylic acid group. The absence of an S-H peak at ~2600 cm^{-1} in dithiol-treated samples and the stiffness of the linker molecule lead us to conclude that the molecule is bound to the surface of two neighboring NQDs. An FTIR spectrum taken from pure BDT is included in Figure 5.1(b) for comparison.

The structure and inter-NQD distance of the NQD assemblies were characterized with synchrotron based GISAXS [20]. NQD films prepared from oleic acid (OA) passivated NQDs form a well-ordered face centered cubic superlattice which self-assembled with close-packed $(111)_s$ planes parallel to the substrate [20] whereas nBDT treated NQD assemblies show amorphous powder scattering features (see

Appendix C). Azimuthally integrated GISAXS intensity profiles of the NQD assemblies, shown in Figure 5.1(c), show a direct correlation between inter-NQD separation and the length of the bi-linker molecule. The PbS_OA film shows a narrow scattering feature corresponding to a well-ordered film with an average interparticle spacing of 4.5 nm. In the case of EDT treated PbS NQD films, we measured an average d-spacing of 2.95 nm, which, considering the 2.7 nm NQD diameter, translates to ~0.25 nm separation between the surfaces of proximate NQDs. We approximated the truncated octahedron shape of NQD as a quasi-spherical particle [21]. Each additional benzene ring contributes ~ 0.3 nm increase in average inter-NQD distance which is reasonable agreement with the expected trend considering that the length of benzene ring is ~ 0.4 nm. The trend observed in GISAXS data validates the approach to tuning the inter-NQD separation and provides direct access to the study of distance-coupling relationships. Despite the broad distributions of inter-NQD spacing present in the amorphous NQD assembly, we found a clear trend in the peaks of the distributions which we correlated with ensemble average measurements such as exciton lifetime measurements, as discussed below.

5.3 Optical characterization

Optical characterization of the NQD assemblies is summarized in Figure 5.2. Absorbance spectra of the samples are shown in the Figure 5.2a. Compared to the PbS_OA film sample, PbS_nBDT samples exhibit pronounced red-shift and broadened absorption peak. The red-shift is a strong indication of the presence of inter-NQD electronic (tunneling) coupling that hybridizes the band edge orbitals of the individual NQDs and thus reduces the quantum confinement energy [8, 13]. We interpret the peak broadening as a result of the distribution of different degree of coupling among the NQD populations. A trend of larger red-shift from samples with smaller inter-NQD spacing is apparent: the biggest red-shift of ~170 meV is seen in the PbS_EDT sample while the smallest red-shift of ~120 meV is seen in the PbS_TBDT sample. The magnitudes of the red-shift shown in our samples are much greater than the ~20 meV red-shift reported earlier in assemblies of larger diameter NQDs [22, 23] (inset of Figure 5.2a). We attribute the greater red-shift in smaller diameter NQDs to the greater electronic wavefunction overlap between smaller NQDs [8]. The quantitative determination of the exact inter-NQD coupling energy from the absorbance data is complicated by multiple factors including an increase in average dielectric constant of NQD film after ligand treatment [22]. Nevertheless, the red-shift of 120 to 170 meV seen in our PbS_nBDT films is a good indication of high inter-NQD coupling energy, well above tens of meV which have been measured elsewhere [13, 14]. Considering the similarity in magnitude of the coupling energy and the exciton binding energy in PbS NQDs [10], we anticipated that the coupling would significantly influence the fate of photogenerated excitons, which we discuss below. In contrast to PbS_nBDT samples, absorbance spectra of PbS_OA film compared to colloidal PbS_OA solution in tetrachloroethylene showed no red-shift and thus no indication of electronic coupling.

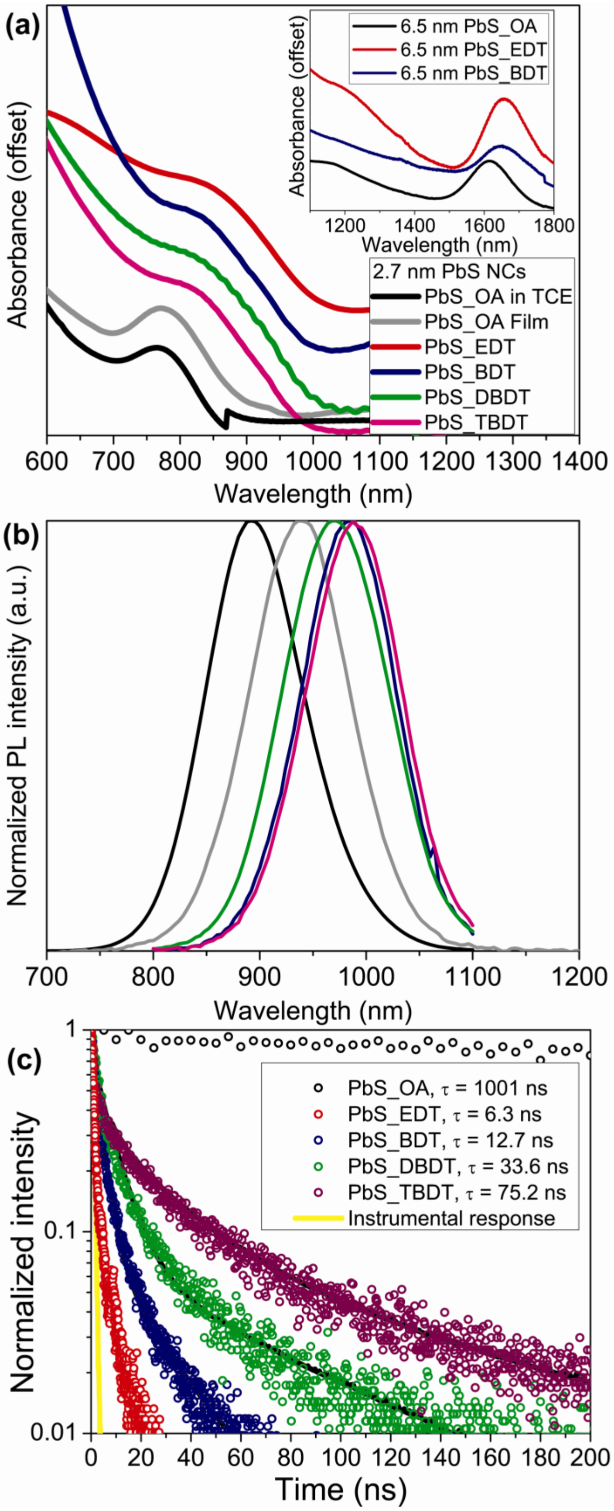

Figure 5.2: (a) Absorbance spectra of the NQD assemblies. The spectra of bi-linker treated NQD assemblies show a 120 to 170 meV red shift indicating strong inter-NQD

electronic (tunneling) coupling. NQD assemblies without the bi-linker treatment (PbS_OA film) does not show electronic coupling. The inset shows a smaller degree (~20 meV) of red-shift observed in bigger (6.5 nm) NQDs. (b) Time integrated photoluminescence spectra (same color legend as Figure 5.2a). Bi-linker treated NQD assemblies show a red-shift and orders of magnitude emission quenching. The PL spectra are normalized to account for the quenching and variations in film thickness. (c) Time resolved photoluminescence data from the NQD assemblies show a two orders of magnitude quenching of exciton lifetime in NQD assemblies treated with bi-linker molecules compared to the untreated NQD assembly. There is a clear trend of longer exciton lifetime with larger inter-NQD separation distance. Each sample was probed at its peak photoluminescence emission wavelength shown in Figure 5.2b. Several control experiments to pin-point the mechanism responsible for the exciton lifetime quenching in our samples are discussed in the main text.

Photoluminescence (PL) measurements can provide basic insights to the relaxation of photogenerated excitons. The PbS_OA film shows a red-shift of ~100 meV in PL compared to colloidal PbS_OA NQDs dispersed in tetrachloroethylene. This effect has been interpreted in context of resonant energy transfer from the population of smaller diameter NQDs to the population of bigger diameter NQDs [7]. The PL spectra of PbS_nBDT films show red-shifts compared to the spectrum of the PbS_OA film. We attribute the slight variation in red-shift across the PbS_nBDT samples to different degree of Stokes shifts with different surface ligands. The PL intensity of all bi-linker treated films was quenched by up to 5 orders of magnitude compared to PbS_OA films. The pronounced PL quenching in NQD films treated with bi-linkers can be attributed to several non-radiative mechanisms including charge transfer to the ligands, charge transfer to neighboring NQDs or charge trapping by NQD surface states.

To better understand the PL quenching mechanism, we turned to transient photoluminescence spectroscopy (see Appendix C for detailed information on the tPL set-up). Transient PL data of PbS_OA films (Figure 5.2c) show a long exciton lifetime of ~1 μs with a single exponential decay behavior. In contrast, PbS_nBDT samples show exciton lifetimes on the order of few to tens of nanoseconds, shortened by two orders of magnitude compared to the PbS_OA film. The decay behavior is not well fit by a single exponential; we fit the data to a bi-exponential decay following a model that has been successfully used in molecular systems [24]. The reduced exciton lifetime observed in PbS_nBDT films suggests that the de-excitation dynamics for PbS_nBDT films are fundamentally different from that of the PbS_OA film. This trend can be explained by several mechanisms such as inter-NQD exciton dissociation, resonant energy transfer [7, 8], charge transfer to surface ligands [25], and surface charge trapping [26]. Carefully designed control experiments are required to distinguish between these possible mechanisms; we discuss these experiments below.

To delineate between resonant energy transfer and exciton dissociation de-excitation pathways, we probed the rise time of PL transients. If low bandgap (large diameter) NQDs would accept energy transfer from larger bandgap (small diameter) NQDs in the assembly, then a characteristic rise time would be observed in the early transient when probed at the long wavelength tail of the PL spectrum [7, 8]. We probed tPL of PbS_nBDT samples at 1060 nm, i.e., in the high wavelength tail of the time integrated

PL peak, and detected no rise time in any of the samples (see Appendix C). Based on the work by Clark et al. [7], we calculated the Förster radius to be ~ 5 nm for PbS NQDs used in this study which translates to a resonant energy transfer lifetime in the PbS_nBDT assemblies on the order of tens to hundreds of nanoseconds. Rise times with such time scales can be clearly resolved with our tPL set-up but were not observed in the PbS_nBDT samples. In contrast, consistent with earlier reports [7], tPL measurement on the PbS_OA film did exhibit a rise time characteristic of resonant energy transfer (Appendix C). These results provide a strong indication that resonant energy transfer is not the dominant de-excitation pathway in PbS_nBDT films.

To distinguish between inter-NQD exciton dissociation and charge transfer to the surface ligand or surface charge trapping, we prepared PbS NQDs treated with ethanethiol, a short ligand molecule, in (1) colloidal solution form and in (2) close-packed film form and compared their exciton lifetimes (See Appendix C for detailed sample preparation procedures). In these experiments, both samples have the same surface molecule with a thiol functional group. Hence, if charge transfer to the ligand [25] or surface trapping [26] were to occur due to the surface thiol molecules, the exciton lifetime would be quenched in both colloidal solution and close packed film forms. Instead, our experiment reveals a long lifetime of 890 ns in colloidal PbS_ethanethiol solution in toluene while identical particles in the close-packed film exhibited a quenched lifetime of 167 ns (see Appendix C). We can therefore conclude that the exciton lifetime quenching does not originate from charge transfer to ligand or surface trapping but rather from proximity of NQDs to each other. We stress that the bi-linker nBDT molecules used in this study have HOMO-LUMO levels that are unsuitable to accept charges from PbS NQDs [19]. In summary, these findings rule out charge transfer to the surface ligand or surface charge trapping as possible mechanisms of exciton lifetime quenching.

5.4 Electric Force Microscopy Characterization

To corroborate our picture of the fate of quenched excitons, we complemented our optical measurements by employing time-resolved electrostatic force microscopy (tr-EFM) to observe light-induced free carrier generation in PbS_nBDT samples at millisecond time scales (see inset of Figure 5.3a). EFM enables direct examination of local capacitance, proportional to free charge density, and local potential [27, 28]. By being able to detect local potential change due to trapped charges [29], EFM also provides direct proof of whether the exciton lifetime quenching is due to surface traps or exciton dissociation. PbS_OA and PbS_nBDT films were prepared on top of interdigitated gold electrodes on glass substrate and loaded into a custom-fabricated high vacuum electric force microscope [29]. All measurements were taken at a single location near the mid-point of the channel between electrodes with no source-drain voltage applied during the measurement. Detailed procedures on sample preparation and EFM measurements are provided in Appendix C. Figure 5.3a shows that there is no change in the capacitance of the PbS_OA film upon illumination with white light. This result, coupled with the optical characterization of PbS_OA film that showed bright PL with long lifetime, indicates that quenched excitons in PbS_OA film do not lead to free carrier generation. In contrast, Figure 5.3b shows that the PbS_EDT film shows an increase in capacitance under light illumination with a rise time faster than the instrumental response time of ~ 4 ms, indicating increased free carrier density upon light illumination. The applied tip voltage of 3 V did not contribute to exciton separation (and thus free charge generation). To show this, we measured the cantilever frequency, $f(t)$, at various tip modulation voltages. At each modulation voltage, we inferred the capacitance by taking the ratio of the Fourier component, $\hat{f}$, of the cantilever frequency at twice the modulation frequency divided by the square of the tip voltage (see Appendix C). We measured nearly identical capacitances at tip modulation voltages of 1, 2 and 3 V (Figure 5.3c), proving that the EFM measurement is not perturbing charge generation. Similar increase in sample capacitance under light illumination was observed in other PbS_nBDT samples (Appendix C). We note that the local potential did not show any sign of trapped charges in PbS_nBDT after turning light off (Appendix C). Taken together, the EFM and optical data show, for the first time to our knowledge, that photogenerated excitons in PbS_nBDT films ultimately results in free carrier generation *without* the aid of a chemical potential gradient or external bias.

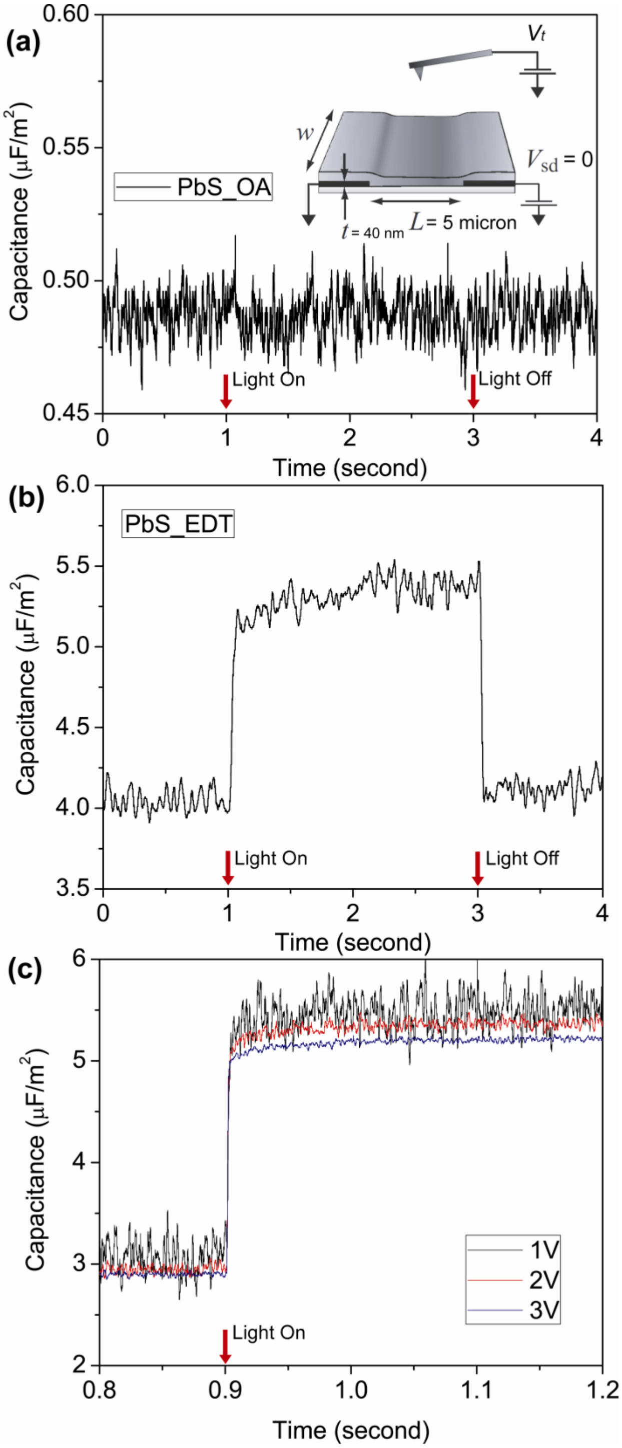

Figure 5.3: (a) The inset shows a schematic of the electric force microscope measurement. No source-drain voltage was applied during the measurements. The PbS_OA film does not show change in capacitance upon white-light illumination,

indicating that the photogenerated excitons in this film do not result in free charge generation. (b) In contrast, the PbS_EDT film shows rapid increase in capacitance upon light illumination indicating a photo-induced increase in free carrier density. This result complements the optically observed exciton lifetime quenching shown in Figure 5.2c and provides a direct evidence of dissociation of photogenerated excitons into free carriers in close packed NQD assembly *without* any heterojunction or external bias. (c) The independence of the Fourier component at twice the modulation frequency divided by the square of the modulation voltage shows that the tip voltage does not cause exciton dissociation (see the main text for details).

5.5 Discussion and conclusion

In light of the corroborating optical and electrical signatures of photogenerated exciton dissociation in PbS_nBDT, we sought to gain further insight on the precise mechanism underlying the exciton dissociation. To do so, we calculated charge transfer time constants in each of the PbS_nBDT samples from the measured exciton lifetimes (Figure 5.2c) via the equation $k_{\mathrm{et}} = 1/\tau_{(\mathrm{coupled})} - 1/\tau_{(\mathrm{isolated})}$ and plotted them versus the inter-NQD distance, d, obtained from GISAXS measurements (Figure 5.1c). The resulting plot shows that the charge transfer rate as a function of inter-NQD distance is well described by a single exponential decay function (Figure 5.4a). This behavior can be described with the Marcus theory [30] which, in the case of symmetric reorganization energy and Gibbs free energy for the charge transfer reaction, simplifies to a rate-distance relationship of the form $k_{et} = k_0 \exp(-\beta\ d)$ in terms of the electron tunneling constant (β) and the donor-acceptor distance (d), describing tunneling of the charge through a potential barrier. In PbS_nBDT films, the donor and the acceptor in charge transfer reaction are the neighboring PbS NQDs. Since all our PbS_nBDT samples are prepared from the same synthesis batch and have the same narrow NQD size distribution and site energy dispersion, identical reorganization energy and Gibbs free energy hold to good approximation. The good fit to single exponential function also indicates that the variation in the potential barrier due to different nBDT bi-linker molecule is small and that the inter-NQD distance is the dominant parameter governing the electron transfer. The value of the electron tunneling constant, β, obtained from fitting the data to a single exponential is 2.6 ± 0.2 nm^{-1}. This value of β should be taken as a lower bound; preliminary calculations indicate that modifying the analysis of k_{et} to account for the different distributions in d-spacing of the PbS_nBDT samples give a slightly larger best-fit β. We note that PbS_OA film, in which *resonant energy transfer* is the dominant pathway for photogenerated excitons, shows an order of magnitude slower rate than the trend from charge transfer rates (Figure 5.4a).

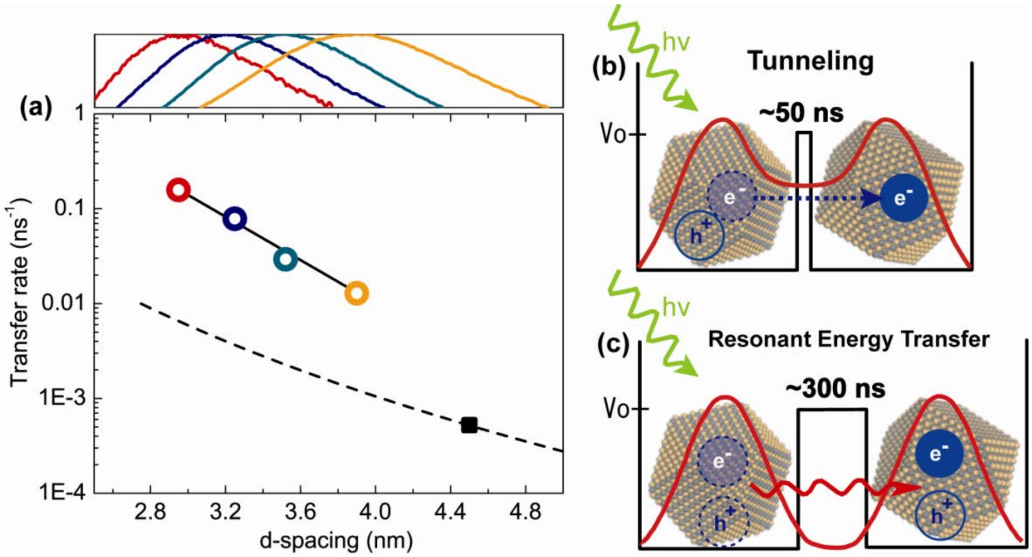

Figure 5.4: (a) Plot of charge transfer rates (Same color legends as Figure 5.1), calculated from exciton lifetimes (Figure 5.2b), versus inter-NQD spacing measured with GISAXS (Figure 5.1c). Single exponential decay fit (black solid line) indicates that the charge transfer occurs via tunneling of charge through a potential barrier. Resonant energy transfer is shown in PbS_OA sample (black rectangle) and the calculated energy transfer rates (dotted line) for corresponding inter-NQD spacing using a Förster radius of 5 nm shows an order of magnitude lower rate than the charge transfer rates. This indicates that exciton dissociation via tunneling is the dominant pathway in the regime of short inter-NQD distance and high coupling energy (Figure 5.4b) whereas resonant energy transfer is dominant in low inter-NQD coupling regime (Figure 5.4c). All calculated transfer rates have error bars smaller than the symbols. Distributions in d-spacing measured with GISAXS are shown on the top of (a).

These results provide several important insights for the design of opto-electronic devices based on NQD artificial solids: (1) Depending on the inter-NQD separation distance and associated inter-NQD coupling energy, there are two distinct regimes – one in which exciton dissociation via tunneling of charge is dominant (Figure 5.4b) and one in which resonant energy transfer is dominant (Figure 5.4c). (2) The initial charge transfer responsible for exciton dissociation in PbS_nBDT NQD arrays is through a coherent tunneling process, without involving charge injection and hopping through the bi-linker molecules [31]. (3) The exciton dissociation rate can be increased exponentially by decreasing either the inter-NQD distance or the electron tunneling constant. The first insight provides a guideline for maximum performance in targeted opto-electronic device applications by selecting the appropriate NQD material, which largely determines the exciton binding energy, and the inter-NQD separation distance, which determines the inter-NQD coupling energy. Consider solar cells and LEDs, for example. Both cases require high electronic coupling, thus shorter inter-NQD separation distance and lower inter-NQD potential barrier, for efficient charge transport across the NQD assembly. However, their requirements for the dominant pathway for excitons are drastically different - solar cells require efficient exciton *dissociation* whereas LEDs require efficient exciton radiative *recombination*. Thus, for solar cell devices, NQD materials with low exciton binding energy are preferred so that inter-NQD coupling energy can be comparable or exceed the exciton binding energy. In that case, the NQD assembly should be in the regime of dominant exciton dissociation, which is the case in the PbS_nBDT samples studied here. In contrast, LEDs require NQD materials with high exciton binding energy for the NQD assembly to be in the regime of dominant radiative recombination. We believe these insights explain why Schottky solar cells based on lead salt NQDs [3, 6] generate a short-circuit current that is two orders of magnitude higher than similarly prepared cadmium-salt Schottky devices [6, 15] whereas, in LED devices, cadmium-salt NQDs have shown promising performances [16]. In lead-salt NQD assemblies with high inter-NQD coupling energy and low exciton binding energy, treatment of NQD assemblies with short bi-linker molecules such as EDT decreases inter-NQD distance enough to be in the regime where exciton dissociation becomes the dominant process – and thus high current density is obtained in photovoltaic device structure. In contrast, the coupling energy in cadmium-salt NQDs with similarly short bi-linker molecules has been measured [8] to be smaller than the exciton binding energy [11] and thus exciton dissociation is blocked and only resonant energy transfer has been observed [8]. We note that exciton dissociation is only the first in a series of sub-processes that constitute the conversion of incident photons to free charges in an external circuit. Other processes such as charge conduction mechanism through NQD arrays [9, 32, 33] also need to be considered to fully explain the higher photocurrent density observed in lead salt NQD arrays compared to cadmium salt NQD arrays. The effects of site energy dispersion due to NQD size distribution and the order/disorder of NQD packing on the conduction through the NQD array are currently being investigated in our laboratories. The second insight reveals that recently reported solar cells employing close packed NQD arrays have not been utilizing charge transfer to the surface ligands [3-6] and presents us with the intriguing question of whether inducing charge transfer to the surface ligands might result in faster exciton dissociation [25, 34] and ultimately improved solar cell efficiency. The third insight suggests possibilities for manipulating the NQD surface to exponentially increase the exciton dissociation rate. Several options such as encapsulating the NQD arrays with different organic or inorganic mediums or using short inorganic spacer instead of bi-linker molecules [35] are available to lower the inter-NQD potential barrier.

In conclusion, we have shown optical and scanned-probe evidence of inter-NQD coupling induced dissociation of photogenerated excitons in lead-salt NQD arrays. The exciton dissociation occurs via tunneling of charge between neighboring NQDs. New insights obtained from this work provide guidelines for improving the design of a range of opto-electronic devices based on NQD solids.

BIBLIOGRAPHY

[1] J. J. Choi, J. Luria, B.-R. Hyun, A. C. Bartnik, L. Sun, Y.-F. Lim, J. A. Marohn, F. W. Wise, T. Hanrath, Nano Letters. **10**, 1805 (2010).

[2] G. Markovich, C. P. Collier, S. E. Henrichs, F. Remacle, R. D. Levine, J. R. Heath, Acc. Chem. Res. **32**, 415 (1999).

[3] G. I. Koleilat, L. Levina, H. Shukla, S. H. Myrskog, S. Hinds, A. G. Pattantyus-Abraham, E. H. Sargent, ACS Nano. **2**, 833 (2008).

[4] K. S. Leschkies, T. J. Beatty, M. S. Kang, D. J. Norris, E. S. Aydil, ACS Nano. **3**, 3638 (2009).

[5] J. J. Choi, Y.-F. Lim, M. E. B. Santiago-Berrios, M. Oh, B.-R. Hyun, L. Sun, A. C. Bartnik, A. Goedhart, G. G. Malliaras, H. D. Abruña, F. W. Wise, T. Hanrath, Nano Lett. **9**, 3749 (2009).

[6] J. M. Luther, M. Law, M. C. Beard, Q. Song, M. O. Reese, R. J. Ellingson, A. J. Nozik, Nano Lett. **8**, 3488 (2008).

[7] S. W. Clark, J. M. Harbold, F. W. Wise, J. Phys. Chem. C. **111**, 7302 (2007).

[8] R. Koole, P. Liljeroth, C. de Mello Donega, D. Vanmaekelbergh, A. Meijerink, J. Am. Chem. Soc. **128**, 10436 (2006).

[9] D. V. Talapin, C. B. Murray, Science. **310**, 86 (2005).

[10] I. Kang, F. W. Wise, J. Opt. Soc. Am. B. **14**, 1632 (1997).

[11] R. W. Meulenberg, J. R. I. Lee, A. Wolcott, J. Z. Zhang, L. J. Terminello, T. van Buuren, ACS Nano. **3**, 325 (2009).

[12] F. W. Wise, Acc. Chem. Res. **33**, 773 (2000).

[13] K. J. Williams, W. A. Tisdale, K. S. Leschkies, G. Haugstad, D. J. Norris, E. S. Aydil, X. Y. Zhu, ACS Nano. **3**, 1532 (2009).

[14] P. Liljeroth, K. Overgaag, A. Urbieta, B. Grandidier, S. G. Hickey, D. Vanmaekelbergh, Phys. Rev. Lett. **97**, 096803 (2006).

[15] I. S. Liu, H.-H. Lo, C.-T. Chien, Y.-Y. Lin, C.-W. Chen, Y.-F. Chen, W.-F. Su, S.-C. Liou, J. Mater. Chem. **18**, 675 (2008).

[16] K. S. Cho, E. K. Lee, W. J. Joo, E. Jang, T. H. Kim, S. J. Lee, S. J. Kwon, J. Y. Han, B. K. Kim, B. L. Choi, J. M. Kim, Nature Photon. **3**, 341 (2009).

[17] M. A. Hines, G. D. Scholes, Adv. Mater. **15**, 1844 (2003).

[18] L. Venkataraman, J. E. Klare, C. Nuckolls, M. S. Hybertsen, M. L. Steigerwald, Nature. **442**, 904 (2006).

[19] A. M. Scheer, G. A. Gallup, P. D. Burrow, Chem. Phys. Lett. **466**, 131 (2008).

[20] T. Hanrath, J. J. Choi, D.-M. Smilgies, ACS Nano. **3**, 2975 (2009).

[21] K.-S. Cho, D. V. Talapin, W. Gaschler, C. B. Murray, J. Am. Chem. Soc. **127**, 7140 (2005).

[22] J. M. Luther, M. Law, Q. Song, C. L. Perkins, M. C. Beard, A. J. Nozik, ACS Nano. **2**, 271 (2008).

[23] M. C. Beard, A. G. Midgett, M. Law, O. E. Semonin, R. J. Ellingson, A. J. Nozik, Nano Lett. **9**, 836 (2009).

[24] J. R. Lakowicz, Principles of fluorescence spectroscopy, Springer, New York, 2006.

[25] M. Sykora, M. A. Petruska, J. Alstrum-Acevedo, I. Bezel, T. J. Meyer, V. I. Klimov, J. Am. Chem. Soc. **128**, 9984 (2006).

[26] A. Pandey, P. Guyot-Sionnest, Science. **322**, 929 (2008).

[27] J. D. Slinker, J. A. DeFranco, M. J. Jaquith, W. R. Silveira, Y.-W. Zhong, J. M. Moran-Mirabal, H. G. Craighead, H. D. Abruna, J. A. Marohn, G. G. Malliaras, Nature Mater. **6**, 894 (2007).

[28] W. R. Silveira, J. A. Marohn, Phys. Rev. Lett. **93**, 116104 (2004).

[29] M. J. Jaquith, J. E. Anthony, J. A. Marohn, J. Mater. Chem. **19**, 6116 (2009).

[30] R. A. Marcus, N. Sutin, Biochim. Biophys. Acta. **811**, 265 (1985).

[31] D. M. Adams, L. Brus, C. E. D. Chidsey, S. Creager, C. Creutz, C. R. Kagan, P. V. Kamat, M. Lieberman, S. Lindsay, R. A. Marcus, R. M. Metzger, M. E. Michel-Beyerle, J. R. Miller, M. D. Newton, D. R. Rolison, O. Sankey, K. S. Schanze, J. Yardley, X. Zhu, J. Phys. Chem. B. **107**, 6668 (2003).

[32] T. S. Mentzel, V. J. Porter, S. Geyer, K. MacLean, M. G. Bawendi, M. A. Kastner, Phys. Rev. B. **77**, 075316 (2008).

[33] B. L. Wehrenberg, D. Yu, J. Ma, P. Guyot-Sionnest, J. Phys. Chem. B. **109**, 20192 (2005).

[34] B.-R. Hyun, A. C. Bartnik, J.-K. Lee, H. Imoto, L. Sun, J. J. Choi, Y. Chujo, T. Hanrath, C. K. Ober, F. W. Wise, Nano Lett. **10**, 318 (2010).

[35] M. V. Kovalenko, M. Scheele, D. V. Talapin, Science. **324**, 1417 (2009).

CHAPTER 6

TUNABLE COUPLING: NANOCRYSTAL QUANTUM DOT LIGHT-EMITTING DIODES WITH CONTROLLED INTER-DOT SPACING[1]

6.1 Introduction

Infrared light-emitting diodes (LEDs) are currently fabricated from direct-gap semiconductors by epitaxy, which makes them expensive and difficult to integrate with other materials. LEDs based on colloidal semiconductor quantum dots, on the other hand, can be solution-processed at low cost, and can be directly integrated with silicon [2]. However, exciton dissociation and recombination have not been well-controlled in these devices, and this has limited their performance [3-9]. Here, by tuning the distance between adjacent PbS quantum dots, we fabricate thin-film quantum-dot LEDs that operate at infrared wavelengths with radiances (6.4 W sr^{-1} m^{-2}) that are eight times higher, and external quantum efficiencies (2.0%) that are two times higher, than the highest values previously reported. The distance between adjacent dots is tuned over a range of 1.3 nm by varying the length of linker molecules from 3 to 8 CH_2 groups, which allows us to achieve the optimum balance between charge injection and radiative exciton recombination. The electroluminescent powers of the best devices are comparable to those produced by commercial InGaAsP LEDs.

---

[1] The results presented in this chapter have been published in Ref [1].

By varying the size of the quantum dots, we can tune the emission wavelengths between 800 nm and 1850 nm.

Colloidal quantum dots have been proposed for the development of low-temperature solution-processed quantum-dot devices, including next-generation photovoltaics, photodetectors and LEDs [2-12]. In particular, the development of high-power, efficient and low-cost infrared LEDs will spur applications such as night vision, optical communications, and sensing. Early efforts to exploit quantum dots in LEDs were based on hybrid device structures in which the quantum dots were interfaced with conjugated polymers. Quantum dots with long capping ligands were either mixed with organic host, or directly sandwiched between organic carrier-transporting layers to form the LED structure [7-9]. The operating mechanism of these devices is mainly based on Förster transfer—exciton energy transfers from the organic host to the quantum dots through the dipole-dipole interaction. Owing to the long capping ligands and the low carrier mobility of the organic materials, these devices suffer from low current density, charge injection imbalance, and exciton ionization caused by large applied bias voltages [13]. Recently, an infrared quantum-dot LED based on direct exciton generation through carrier injection achieved 1.15% external quantum efficiency (EQE), but the organic carrier-injection layer limited the current density, and consequently, the radiance [3] (0.0067 W sr^{-1} m^{-2}). To date, the brightest infrared quantum-dot LEDs have achieved a radiance of 0.8 W sr^{-1} m^{-2} (see Appendix D), with 0.5% external quantum efficiency (EQE) [9]. In visible-wavelength quantum-dot LEDs, inorganic charge-transport layers (ZnO:SnO_2 alloy for electrons, and NiO for holes) were recently employed to increase current density to a few amperes per square centimeter, and consequently the radiance was significantly improved [4]. These results directly reflect the improved performance of the charge-injection layers of the devices.

Charge-carrier dynamics in the quantum dot layer also play a critical role in device performance. Increasing the carrier injection rate while avoiding excessive non-radiative decay through dissociation or field ionization and eventual trapping of the charge carriers requires a delicate balance of the relevant physical processes. The requirements for successful operation of quantum-dot LEDs are more constrained than those for operation of quantum-dot photovoltaic devices. Beyond the challenge of achieving efficient inter-dot charge transfer common to both, an LED must also balance charge injection against efficient radiative recombination within the quantum dot layer. The competition between exciton dissociation and radiative recombination can be controlled by tailoring the inter-dot separation using linker molecules of different lengths [14]. The crucial development that we report here is the ability to enhance the quantum efficiency of exciton recombination dramatically by tuning the distance between PbS quantum dots in the active layer of an LED. For linker molecules with between 3 and 8 CH_2 groups, the quantum efficiency can vary over two orders of magnitude. By fabricating devices with the optimal linker length along with high-performance carrier-injection layers, we demonstrate infrared quantum-dot LEDs with an 8-fold increase in radiance and 2-fold increase in EQE over the prior best devices.

6.2 Device design and fabrication

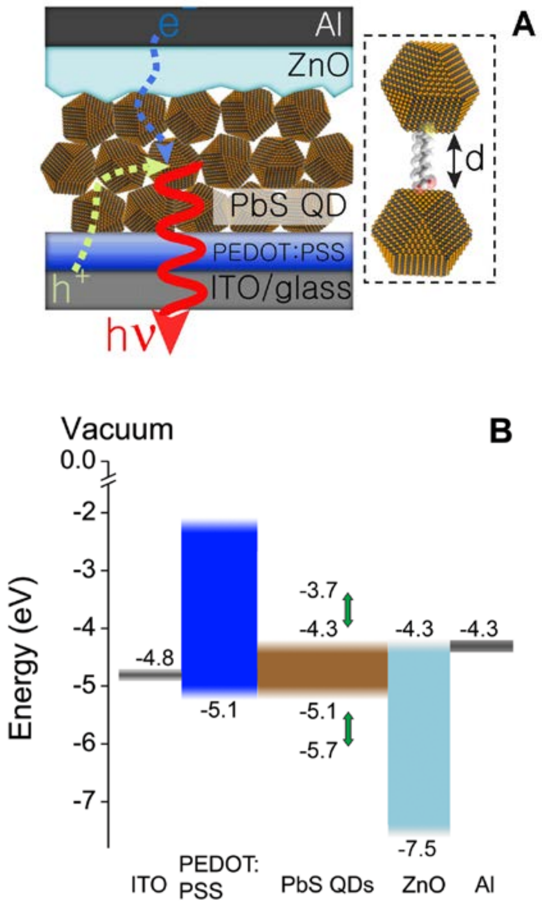

Figure 6.1: Physical and electronic structures of the LEDs. (A) Schematic device structure. (B) Electronic energy levels of each material in the device stack. Energies are relative to vacuum, which is defined as the zero of electron energy. The arrows indicate the tuning range of the electron affinity (from -3.7 eV to -4.3 eV) and the ionization potential (from -5.7 eV to -5.1 eV) by changing the diameter (from 2.7 nm to 6.5 nm) of the quantum dots.

The schematic structure of the quantum-dot LEDs is shown in Figure 6.1A, and the rationale for their operation can be understood from the relevant energy levels in

Figure 6.1B. Lead-salt quantum dots are well-established as efficient emitters in the near-infrared, and in this work we focus on PbS quantum dots because their absolute energy levels [15] are most appropriate (Figure 6.1B). The ZnO layer is intended to inject electrons into the quantum dots and block holes, while the poly(3,4-ethylenedioxythiophene) poly(styrenesulfonate) (PEDOT:PSS) film should inject holes and block electrons. We fabricated electron-injecting layers from colloidal ZnO nanoparticles for several reasons. First, the electron mobility of ZnO [16] is about two orders of magnitude higher than that of commonly-used *tris*(8-hydroxyquinolinato) aluminum (Alq3) [17]. Second, the ZnO prevents direct contact between the quantum dots and the aluminum electrode, thereby avoiding plasmonic quenching of the quantum dot emission [18]. Finally, the use of colloidal ZnO nanoparticles avoids damage to the quantum dots, which would likely occur with ZnO layers deposited by sputtering [19]. The transparent conductor PEDOT:PSS is chosen as a high-conductivity (~ 10^{-3} S cm^{-1}) hole-transporting contact to the quantum dot film. Nearly-ohmic contacts are formed between the quantum dot layer and the carrier-transporting layers due to the close energy-level alignment.

Colloidal PbS quantum dots were synthesized using organometallic precursors [20, 21]. We successively spin-coated the PEDOT:PSS, PbS quantum dots, and ZnO nanoparticle layers onto cleaned, pre-patterned indium tin oxide (ITO) substrates. To couple the quantum dots within the active layer, the long-chain oleate ligands were displaced by bifunctional linker molecules of controlled length. Specifically, we used mercapto alkyl carboxylic acids of variable alkyl chain lengths, including 3-mercaptopropionic acid (MPA), 6-mercaptohexanoic acid (MHA), 8-

mercaptooctanoic acid (MOA), and 11-mercaptoundecanoic acid (MUA). The active layer was formed by repeated cycles of quantum-dot spin-casting and linker treatment, which provides robust, crack-free films [10]. The aluminum top electrode was deposited by thermal evaporation on the ZnO.

Small separation favors efficient charge transport (in the plane of the quantum dot layer as well as in the injection direction), but also leads to more-rapid exciton dissociation [14]. On the other hand, larger spacing promotes radiative recombination, but charge injection is more difficult. We determined the distance between quantum dots in the films using grazing-incidence small-angle X-ray scattering (GISAXS) (Figure 6.2A). The electroluminescence quantum efficiencies of the films were measured (see Methods) as a function of the inter-dot distance.

6.3 Device characterization

Starting from MPA, as the inter-dot distance increases by 0.7 nm, the EQE increases by a factor of ~150 (Figure 6.2B). With further increase, the efficiency declines. The measured photoluminescence lifetimes and quantum efficiencies of the same quantum dot films increase monotonically and by a factor of about 20 with inter-dot distance (Appendix D). However, increasing the spacing between quantum dots also weakens the screening of any external field. This in turn increases the probability of exciton ionization [13], which effectively decreases the electroluminescence efficiency. The maximum EQE was obtained with MOA for all quantum dot diameters. We also measured the EQE as a function of current density, for each linker. For most of the devices, the EQE increases slightly, and then decreases with current density (Figure 6.2C). The EQE varies by less than a factor of 10 while the current density varies over two to three orders of magnitude. The current density at which the EQE reaches its maximum value depends on the linker molecule (see Appendix D). Finally, the EQE depends on the size of the quantum dots, even for fixed linker. Although the measured EQE fluctuates from device to device, the overall trend is that the EQE decreases as the quantum dot size increases (see Appendix D), which is consistent with the trend of PL quantum efficiency [22]. The highest EQE (2.0±0.3%) was obtained from MOA-capped quantum dots with emission peak at 1054 nm (Figure 6.2C, inset). With 1.2 V applied bias, the electroluminescence power is 185 nW. The corresponding internal quantum efficiency is estimated to be 8%, based on a calculation that assumes Lambertian emission (see Methods). The highest radiance was obtained from a device with MOA-capped quantum dots (diameter 4.5 nm) with an emission peak at 1232 nm (Figure 6.2C). It emits 60 μW from a pixel of area 0.03 cm^2, which corresponds to a radiance of 6.4 W sr^{-1} m^{-2}. This value is 8 times the highest radiance of an infrared quantum-dot LED reported previously [9]. The electroluminescence power is comparable to the state-of-the-art infrared LEDs (e.g., commercial InGaAsP LEDs) fabricated by planar epitaxial technology over the range 900 – 1300 nm.

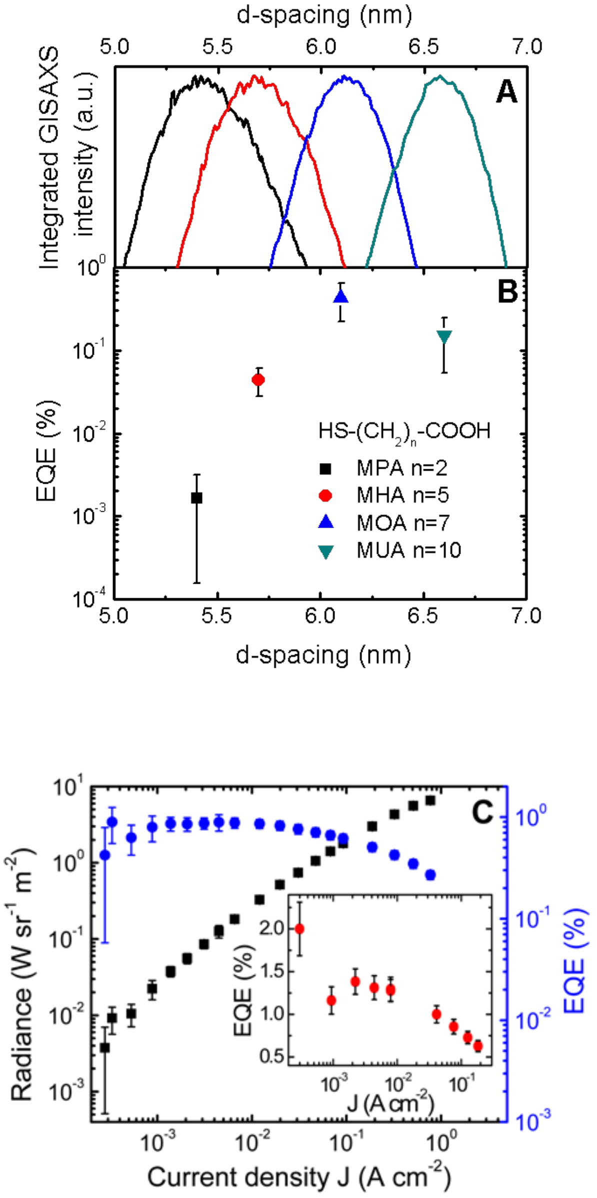

Figure 6.2: Relation between LED performance and inter-dot distance in the film. (A) Azimuthally integrated GISAXS intensity of quantum dot films with varying linker length (see Appendix D). (B) EQE dependence on the inter-dot distance. Error bars indicate the EQE fluctuations in a broad range of bias (0.7 ~ 11 V), and from diode to diode. (C) Dependence of radiance (squares) and EQE (circles) on the current density

for the device with the maximum radiance. Inset: dependence of EQE on current density for the device with the maximum EQE. The error bars indicate the overall experimental errors (see Appendix D). All the measurements were taken from the devices which were made using quantum dots with diameter 4.5 nm, except the inset, which was made using quantum dots with diameter 3.5 nm.

6.4 Discussion on the effects of tuning NQD size and inter-NQD distance on device behavior

We believe that the competition between exciton dissociation (and eventual non-radiative recombination) and radiative recombination dominates the variation of EQE with the different linker molecules. However, other effects may play a role. Changing the linker molecules may change the passivation of the quantum dot surfaces to some extent, in addition to changing the electronic coupling between quantum dots. The balance of charge injection and the efficiency of coupling out emitted light will also be influenced by the choice of linker molecules. Further work will be needed to quantitatively assess the role of these processes. Finally, we estimate that the number of excitons per quantum dot is always well below one. Thus, Auger relaxation of multiple excitons plays a negligible role in the dynamics.

The quantum-dot LEDs show good rectification behavior (see Appendix D). A representative current-voltage characteristic (corrected for the built-in potential [23]) reveals a single operation regime with a slope of 2.1 (Figure 6.3), which implies that the current is space-charge-limited. The high mobility of the carrier-transporting materials facilitates high current density (~ 1 A cm^{-2}) at a fairly low bias (~ 4.5 V) in these devices (Figure 6.3). The current density is improved by several orders of magnitude compared to previous quantum-dot LEDs [3, 4, 7, 9], and this contributes to the high radiance of our devices.

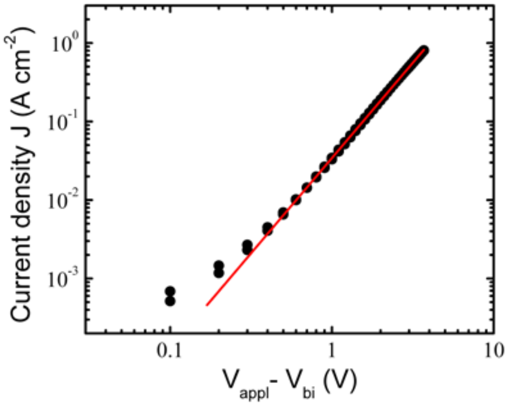

Figure 6.3: Current density-voltage characteristic of a device made of MOA-capped quantum dots with diameter 4.5 nm. The slope of the solid line is 2.1. Scans acquired with increasing and decreasing bias are displayed, and slight hysteresis is observed.

Figure 4 shows EL and PL spectra of quantum-dot LEDs with different sizes of quantum dots. The emission peak can be tuned from 950 nm up to 1650 nm, and the emission tail extends from 800 nm to beyond 1850 nm. There is virtually no broadening or shift of the electroluminescence spectra with respect to the PL spectra. The radiance is maximum for devices that emit between 900 and 1300 nm, and decreases outside that range, while the current is approximately constant. The IR image of a typical device (Figure 6.4, inset) shows uniform emission near 1244 nm, which is evidence of uniform carrier-transport and quantum-dot active layers.

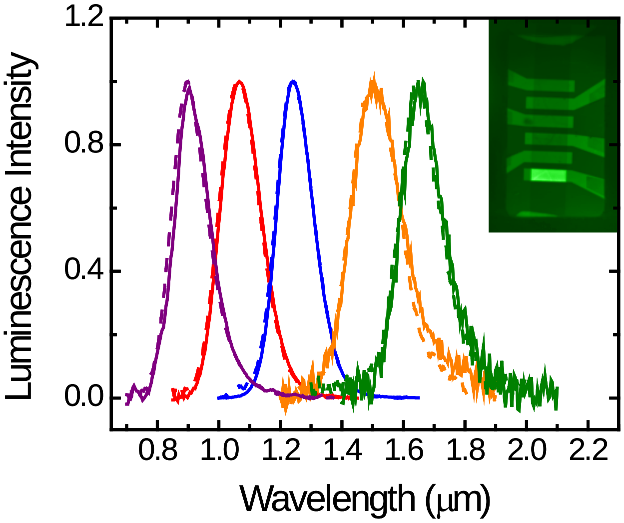

Figure 6.4: Emission spectra and an infrared image of LEDs. Normalized electroluminescence (solid) and PL (dashed) spectra of LEDs made of different size quantum dots, all capped by MHA linkers. Inset: photograph of a device emitting at 1244 nm taken by an InGaAs camera.

The performance of the quantum-dot LEDs presented here can compete with state-of-the-art infrared LEDs fabricated by planar epitaxy. Moreover, we are optimistic that further performance improvements are possible based on our understanding of the limitations of charge transport and injection into the quantum-dot active layer. In general, fine-tuning of the mobilities and carrier-injection rates can optimize the LED efficiency and radiance [24]. The PbS quantum dots capped by mercapto alkyl carboxylic acids linkers are effectively p-type [25]: the electron mobility in the film is lower than the hole mobility, and as a result electron-hole recombination may occur near the cathode [24]. This non-uniform distribution of recombination may limit the device efficiency. The mobilities can be balanced by treating the quantum dots with amine-based linker molecules, which has been done for PbSe [26, 27] quantum dots. On the other hand, the difference of the conductivities of the electron- and hole-transporting layers causes imbalance of carrier injection, which consequently charges the quantum dots. Charging increases the probability of non-radiative Auger relaxation, which quenches the luminescence [18]. However, this imbalance can be tuned by adjusting the conductivity of the PEDOT:PSS film by changing the ratio of PSS to PEDOT [2], or the ZnO film through photodoping (see Appendix D).

By controlling the distance between quantum dots on the angstrom level, exciton recombination in a quantum-dot film can be enhanced dramatically, and this leads to order-of-magnitude improvement in infrared LEDs. Further improvements can be expected as the surface passivation of lead-salt and other infrared nanostructures is improved. These solution-processed emitters may be easily integrated with other materials. The results and approach presented here can be extended to a broad range of nanostructure-based optoelectronic devices.

BIBLIOGRAPHY

[1] L. Sun, J. J. Choi, D. Stachnik, A. C. Bartnik, B.-R. Hyun, G. G. Malliaras, T. Hanrath, F. W. Wise, Nature Nanotechnology doi:10.1038/nnano.2012.63 (2012).

[2] K.-S. Cho, E. K. Lee, W.-J. Joo, E. Jang, T.-H. Kim, S. J. Lee, S.-J. Kwon, J. Y. Han, B.-K. Kim, B. L. Choi, J. M. Kim, Nature Photonics. **3**, 341 (2009).

[3] K. N. Bourdakos, D. M. N. M. Dissanayake, T. Lutz, S. R. P. Silva, R. J. Curry, Applied Physics Letters. **92**, 153311 (2008).

[4] J. M. Caruge, J. E. Halpert, V. Wood, Bulovi, V., M. G. Bawendi, Nature Photonics. **2**, 247 (2008).

[5] S. Coe, W.-K. Woo, M. Bawendi, V. Bulovic, Nature. **420**, 800 (2002).

[6] V. L. Colvin, M. C. Schlamp, A. P. Alivisatos, Nature. **370**, 354 (1994).

[7] G. Konstantatos, C. Huang, L. Levina, Z. Lu, E. H. Sargent, Advanced Functional Materials. **15**, 1865 (2005).

[8] J. S. Steckel, S. Coe-Sullivan, V. Bulović, M. G. Bawendi, Advanced Materials. **15**, 1862 (2003).

[9] N. Tessler, V. Medvedev, M. Kazes, S. Kan, U. Banin, Science. **295**, 1506 (2002).

[10] J. J. Choi, Y.-F. Lim, M. B. Santiago-Berrios, M. Oh, B.-R. Hyun, L. Sun, A. C. Bartnik, A. Goedhart, G. G. Malliaras, H. c. D. Abruna, F. W. Wise, T. Hanrath, Nano Lett. **9**, 3749 (2009).

[11] G. Konstantatos, I. Howard, A. Fischer, S. Hoogland, J. Clifford, E. Klem, L. Levina, E. H. Sargent, Nature. **442**, 180 (2006).

[12] F. W. Wise, Acc. Chem. Res. **33**, 773 (2000).

[13] H. Huang, A. Dorn, G. P. Nair, V. Bulovic, M. G. Bawendi, Nano letters. **7**, 3781 (2007).

[14] J. J. Choi, J. Luria, B.-R. Hyun, A. C. Bartnik, L. Sun, Y.-F. Lim, J. A. Marohn, F. W. Wise, T. Hanrath, Nano Lett. **10**, 1805 (2010).

[15] B.-R. Hyun, Y.-W. Zhong, A. C. Bartnik, L. Sun, H. D. Abruna, F. W. Wise, J. D. Goodreau, J. R. Matthews, T. M. Leslie, N. F. Borrelli, ACS Nano. **2**, 2206 (2008).

[16] F. Verbakel, S. C. J. Meskers, R. A. J. Janssen, Journal of Applied Physics. **102**, 083701 (2007).

[17] R. G. Kepler, P. M. Beeson, S. J. Jacobs, R. A. Anderson, M. B. Sinclair, V. S. Valencia, P. A. Cahill, Applied Physics Letters. **66**, 3618 (1995).

[18] K. T. Shimizu, W. K. Woo, B. R. Fisher, H. J. Eisler, M. G. Bawendi, Physical Review Letters. **89**, 117401 (2002).

[19] D. A. R. Barkhouse, I. J. Kramer, X. Wang, E. H. Sargent, Optics express. **18**, A451 (2010).

[20] M. A. Hines, G. D. Scholes, Advanced Materials. **15**, 1844 (2003).

[21] C. B. Murray, C. R. Kagan, M. G. Bawendi, Annual Review of Materials Science. **30**, 545 (2000).

[22] O. E. Semonin, J. C. Johnson, J. M. Luther, A. G. Midgett, A. J. Nozik, M. C. Beard, J. Phys. Chem. Lett. **1**, 2445 (2010).

[23] G. G. Malliaras, J. R. Salem, P. J. Brock, C. Scott, Physical Review B. **58**, R13411 (1998).

[24] G. G. Malliaras, J. C. Scott, Journal of Applied Physics. **83**, 5399 (1998).

[25] A. G. Pattantyus-Abraham, I. J. Kramer, A. R. Barkhouse, X. Wang, G. Konstantatos, R. Debnath, L. Levina, I. Raabe, M. K. Nazeeruddin, M. Grätzel, E. H. Sargent, ACS Nano. **4**, 3374 (2010).

[26] M. Law, J. M. Luther, Q. Song, B. K. Hughes, C. L. Perkins, A. J. Nozik, J. Am. Chem. Soc. **130**, 5974 (2008).

[27] D. V. Talapin, C. B. Murray, Science. **310**, 86 (2005).

CHAPTER 7

TUNABLE STRUCTURE: CONTROLLING NANOCRYSTAL QUANTUM DOT SUPERLATTICE SYMMETRY THROUGH SURFACE LIGAND INTERACTIONS[1]

7.1 Introduction

The assembly of NQDs into ordered superstructures is forecast to yield a new class of materials, also referred to as *artificial* solids, with tunable optical, electrical, and magnetic properties [2, 3]. Most proposed NQD-based technologies depend on functional assemblies in which the constituent NQDs interact with each other and macroscopic external contacts. Therefore, controlling the structure of the NQD assembly is both a valuable degree of freedom to gain fundamental insights into tunable collective properties of the NQD ensemble as well as a critical requirement for the development of NQD based technologies [2, 4, 5]. Compared to the growing body of knowledge on properties of individual NQDs, progress in understanding the mechanisms underlying the formation of various NQD assemblies and the relationship between superlattice structure and its collective properties has lagged behind.

Challenges to building the foundational understanding of mechanisms governing NQD assembly formation arise primarily from the inherent complexity of the self-

---

[1] The results presented in this chapter have been published in Ref [1].

assembly process. NQD superlattice self-assembly resides naturally at the intersection of molecular crystal growth and the assembly of micrometer-sized colloids. A number of interactions between the NQDs, the surface-bound ligands and the surrounding solvent need to be considered [6-9]. To a first approximation, the interaction between colloidal NQDs can be described by a soft sphere model which assumes isotropic NQD interaction potentials and thus predicts the formation of close-packed (i.e. face-centered cubic, *fcc* or hexagonal close-packed, *hcp*) assemblies. The effective 'softness' of the NQD/ligand complex and the shape of the NQD core introduce important perturbations that can lead to the formation of superlattices with non-close-packed (e.g., body-centered cubic, *bcc*) symmetry [10-13]. Electrostatic interactions must also be considered; for example, Talapin et al. [14] recently attributed the formation of NQD assemblies with non-close packed simple hexagonal (*sh*), symmetry to perturbations introduced by the electrostatic interactions between permanent NQD dipoles. In a separate report, we show that NQDs with identical core and ligand can be assembled into predefined superlattices with either *fcc,* body centered-tetragonal *(bct),* or *bcc* symmetry with orientational order of NQDs in their lattice site [15]. This work underscored the significance of a molecular-level understanding of the role of ligand-ligand and ligand-solvent interactions in the self-assembly process.

Here, we show that the ligand coverage on the NQD surface presents another important parameter in understanding and directing NQD superlattice assembly. We discovered a relationship between ligand coverage density and superlattice symmetry and interpret the trend in context of anisotropic changes in the ligand coverage on specific NQD facets. In this model, changes in surface chemistry amplify the effect of aspherical shape of NQD on the interaction potential and lead to superlattices with long-range translational *and* orientational order. The interpretation of our experimental observations is corroborated by density functional theory (DFT) calculations of the ligand binding strength on specific NQD facets. Taken together, our experimental and computational results illustrate that facet-specific ligand surface coverage can change the asphericity of the NQD-ligand complex and thereby control the symmetry of the resulting NQD superlattice.

7.2 X-ray scattering results

The X-ray scattering results summarized in Figure 7.1 show that colloidal NQD suspensions from the same synthesis batch can self-assemble to form superlattices with either *fcc* or *bcc* symmetry depending on the extent of air exposure of the colloidal suspension. We aged a 5 mg/ml hexane suspension of oleic acid (OA) passivated PbS NQD inside a capped glass vial under ambient air and ambient light. The suspension was returned to the glove box, NQDs were precipitated with ethanol, centrifuged to remove unbound ligand and finally redispersed in hexane. A control sample suspension from the same synthesis batch was aged inside a nitrogen glove box (oxygen concentration < 1 ppm) for the same period (four months) and washed with the same protocol. Using a previously reported method [16], NQD assemblies were formed via drop-casting in solvent saturated environment on top of cleaned silicon substrates (see Appendix E for details). Similar experiments with shorter air exposure periods showed that suspensions exposed to air for only 2 days assembled into *bct* superlattice symmetry while *bcc* NQD superlattice were formed from colloidal suspensions exposed to 6 days of ambient air. We note that the *fcc*-*bct*-*bcc* superlattice symmetry transformation is related through a Bain distortion as discussed in a separate report by our group [15].

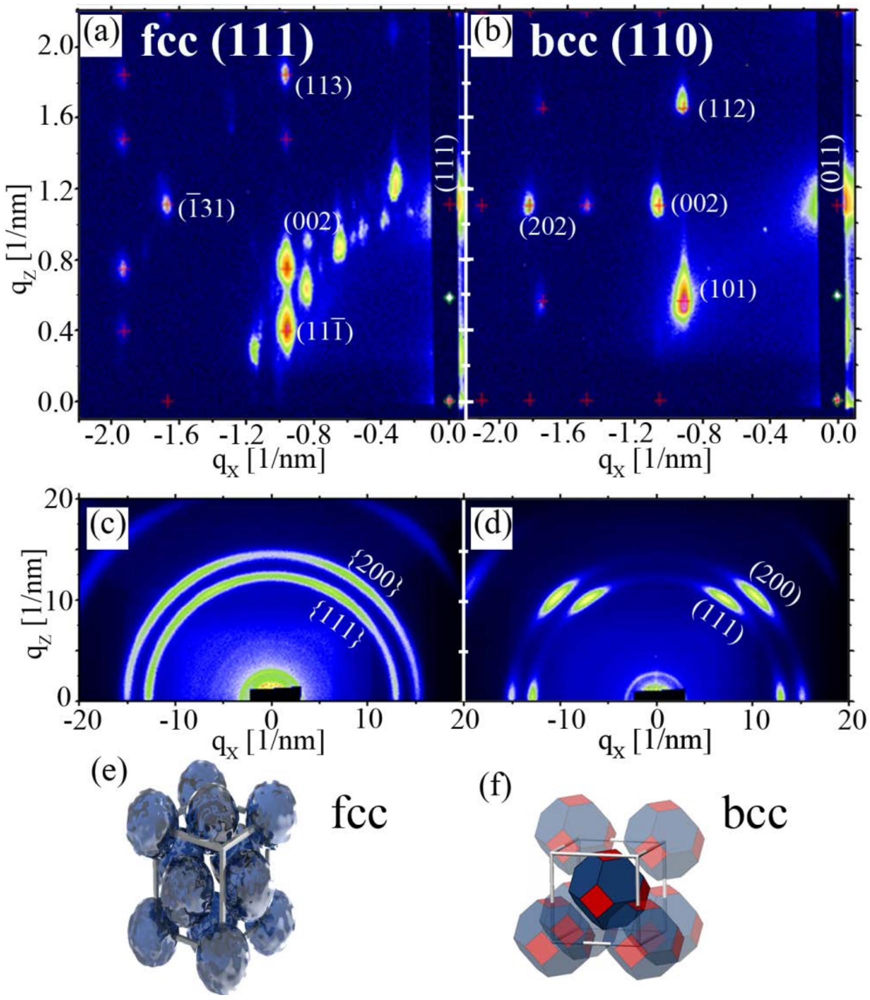

Figure 7.1: (a) N$_2$-aged PbS NQDs formed an fcc superlattice with (111)$_{SL}$ planes parallel to the substrate, as shown by GISAXS. The associated GIWAXS pattern (c) shows at best weak orientational ordering of individual NQDs. (b) Air-aged PbS

NQDs form bcc superlattice with $(110)_{SL}$ planes parallel to the substrate and with strong alignment of individual NQDs (d). schematic model of (e) *fcc* and (f) *bcc* superlattice with orientational coherence of individual NQDs. The red shaded $\{100\}_{NQD}$ are characterized by reduced ligand coverage as discussed in the text.

The grazing incidence small angle X-ray scattering (GISAXS) pattern of the control PbS NQD film (*i.e.* aged in nitrogen) shown in Figure 7.1a can be uniquely indexed to a highly-ordered superlattice with *fcc* symmetry with $\{111\}_{SL}$ planes oriented parallel to the substrate. The subscripts ‘SL’ and ‘NQD’ refer to the crystallographic planes and direction of the superlattice and individual nanocrystals respectively. The superlattice constant, a_{fcc}, of this assembly is measured to be 13.9 nm, and the lattice exhibits approximately 8% shrinkage in the vertical direction (normal to the substrate). Remarkably, air-aged NQDs assembled to form a different superlattice symmetry than the *fcc* assembly observed in the nitrogen-aged control sample. The GISAXS pattern of NQD assemblies formed from air-aged NQDs reveals the scattering signature of crystal symmetry indexed to a *bcc* symmetry with $\{110\}_{SL}$ planes parallel to the substrate (Figure 7.1b). The *bcc* superlattice constant, a_{bcc}, is 11.0 nm and the structure exhibits approximately 3% shrinkage in the vertical direction.

To compare the different superlattice symmetries revealed by the GISAXS patterns, we analyzed the nearest-neighbor separation and the packing density (NQD per unit volume). We determined the nearest neighbor separation by analyzing the spacing between NQD surfaces, δ_{hkl}, along the [*hkl*] close-packed direction of the superlattice. In *fcc* crystals the close-packed directions are the face diagonals <110>, hence the shortest separation between the surfaces of neighboring NQDs is given by $\delta_{110} = \left(\sqrt{2}/2\right)a_{fcc} - \bar{d}_{NC}$, where $\bar{d}_{NC}$ is the average NQD diameter determined from statistical analysis of TEM images (*vide infra*). In the case of the *fcc* superlattice formed from N_2-aged NQDs, this spacing is 3.5±0.6 nm, which corresponds to approximately twice the length of OA molecules (~1.8 nm). We find a similar nearest-neighbor separation in the *bcc* superlattice (3.4±0.7 nm); in this case the close-packed directions are along the body diagonals <111> and the corresponding inter-NQD separation is given by $\delta_{111} = \left(\sqrt{3}/2\right)a_{bcc} - \bar{d}_{NC}$. Both *fcc* and *bcc* NQD superlattices are characterized by a packing density of approximately ($\rho \sim 1.49(10^{18})$ cm^{-3}). The similarities in packing density suggest that the approximation of the NQD as a spherical particle is invalid since the theoretical volume packing fraction of spheres in a *fcc* crystal (0.74) is significantly larger than for a *bcc* crystal (0.68). This comparison suggest that the approximation of the NQDs as spheres is invalid and shape effects need to be considered more closely.

To better understand how superlattice symmetry is related to the shape and orientation of individual NQD within the lattice, we simultaneously measured grazing-incidence wide-angle X-ray scattering (GIWAXS). The GIWAXS pattern of the *fcc* superlattice formed from N_2-aged NQDs shows ring-like scattering patterns which indicates that individual NQDs are randomly oriented within their superlattice sites (Figure 7.1c). In contrast, *bcc* superlattices formed from air-aged NQDs showed $(111)_{NQD}$ and $(200)_{NQD}$ reflections with narrow azimuthal widths in the GIWAXS pattern. This scattering indicates long range orientational ordering of individual

NQDs in their lattice sites (Figure7.1d). Specifically, we find that the $[110]_{NQD}$ axis of PbS NQDs within the superlattice is oriented coaxially with the $[110]_{SL}$ direction of the *bcc* superlattice. Figure 7.1e and 7.1f schematically illustrate the translational and orientational order in the NQD *fcc* and *bcc* superlattices.

Taken together, the small-angle and wide-angle X-ray scattering data provide important insights on the effective shape of the interaction volume of the NQD core/surface ligand complex. The combination of long-range translational and orientational ordering in the *bcc* superlattices cannot be explained with the NQDs modeled as soft spheres. Instead, orientational coherence of NQDs within the superlattice indicates an aspherical interaction potential. More precisely, the NQDs in the air-aged suspension interact as truncated octahedrons. Note that the special case of a truncated octahedron is the Wigner-Seitz cell of the *bcc* superlattice which can be packed with 100% space filling density in a *bcc* crystal. NQDs in the N_2-aged suspensions on the other hand assemble into an *fcc* superlattice without orientational coherence; in this case quasi-spherical NQD approximation adequately describes the symmetry of the interaction potential.

7.3 Searching for origin of different superlattice symmetry

The observation of different superlattice symmetries leads to the intriguing question: why do colloidal NQDs aged under different conditions self assemble into different superlattice symmetries? To answer this question we formulated the following three alternative hypotheses:

(i) *NQD size, shape and charged facets*: Figure 7.2a and 7.2b show transmission electron microscopy (TEM) images and statistical image analysis of NQD monolayers prepared from the colloidal suspensions aged in nitrogen and air, respectively. Air-aged NQDs exhibited a slightly smaller NQD diameter (6.1±0.7 nm) compared to the N_2-aged NQDs (6.3±0.6 nm). We note that the extent of reduction of the average PbS NQD diameter is less pronounced than that of a recent report by Sykora et al. [17] in the case of PbSe NQDs. Moreover, our PbS NQD suspension remained stable for the four-month time-frame considered in our aging experiments and excessive aggregation was not observed. We tentatively attribute the difference to various factors including differences between PbS and PbSe NQDs oxidation, slight differences in NQD synthesis and cleaning procedures, NQD size, solution concentration and light exposure [18]. The TEM analysis summarized in Figure 7.2 allows us to eliminate changes in the NQD core size and shape as the driving force behind the superlattice symmetries.

(ii) NQD dipoles and electrostatic charging due to ligand loss: As an alternative hypothesis, we also considered the possibility of an aspherical interaction potential arising from NQD dipoles or more generally Coulombic interactions of charged NQDs. We tested the electrophoretic mobility of NQDs with different ligand coverage and observed no significant correlation between the electrophoretic mobility and the NQD ligand coverage (Appendix E). This suggests that possible differences in the nature of charged surface states are either absent or below the measurement sensitivity.

(iii) NQD surface chemistry and molecular interactions of surface bound ligands: NQD surface ligand coverage can be determined using infrared spectroscopy. Fourier transform infrared (FTIR) spectra of colloidal PbS NQDs dispersed in tetrachloroethylene show two distinct features: (i) the C-H vibrational signatures (υ_{CH}; near 2900 cm^{-1}) of the OA ligand and (ii) the exciton peak (E_G; ~6000-7000 cm^{-1}) of the quantum confined NQD core (Figure 7.2c). Consistent with other reports [17-19], we observe a blue-shift of the NQD exciton peak in response to air exposure, which suggests that air-aged NQDs are characterized by stronger quantum confinement, i.e. a decrease in the volume of the PbS NQD to which the wave functions are confined [20]. Based on the well-established relationship between NQD size and energy gap (E_G) [21-23], we can correlate the 0.05 eV blue shift of the exciton peak with reduction in NQD core size by approximately 0.4 nm which is in good agreement with the TEM analysis.

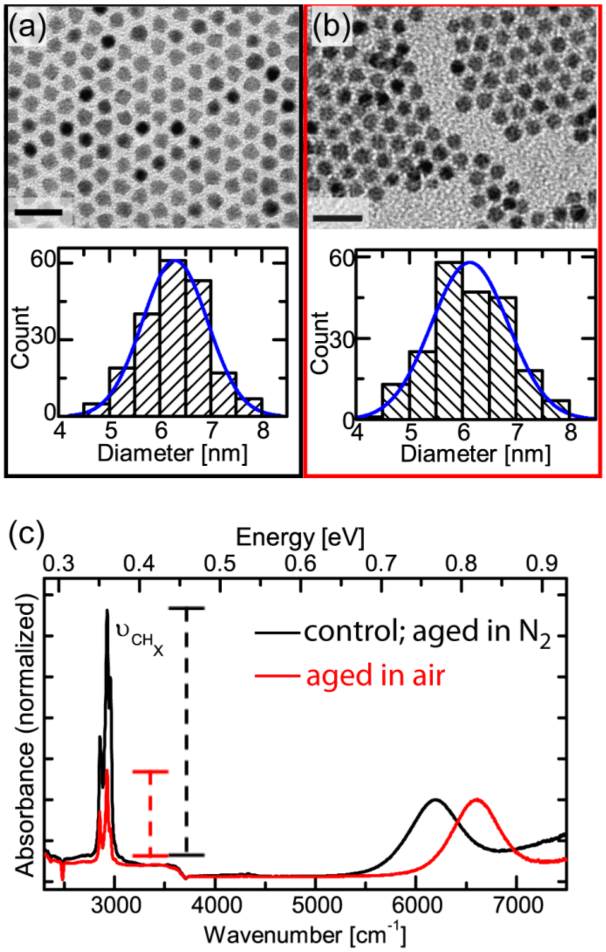

Figure 7.2: TEM images and histogram of NQD size analysis of suspensions aged in nitrogen (a) and in air (b). (c) FTIR spectrum of colloidal PbS NQD suspensions. Suspensions aged in air show a decreased intensity of C-H vibrations due to reduced ligand coverage and a blue shift in the exciton peak of the NQD core.

We can use the relative intensity of the ligand stretching (υ_{CH}) and NQD core excitation (E_G) spectral signatures to directly assess the ratio (ϕ) of OA ligands per NQD. We calibrated peak height of υ_{CH} from the NQD suspension relative to standardized solutions with known OA concentration and determined the NQD concentration from size-dependent extinction coefficient of PbS NQDs [24] (detailed calculations are provided in Appendix E). Using this approach we found that the N_2-aged NQDs had a ligand coverage of approximately 4.5±0.7 nm^{-2} whereas the air-aged NQDs had a 60% lower coverage (~1.8±0.3 nm^{-2}). We emphasize that the calculated ligand density should be taken as an upper bound estimate since the actual surface area of the NQD depends on the specific shape and surface faceting. Similar calculations for truncated octahedron shaped NQDs result in approximately 10% lower coverage density due to larger overall surface compared to spheres of equal volume (see Appendix E). Our calculated ligand coverage agrees well with a previous report by Moreels et al. [19] in which they presented extensive studies on surface chemistry of PbSe NQDs and observed a similar surface ligand density of 4.2 nm^{-2} and 40% ligand loss due to 2 months of air exposure.

We conjectured that the reduced surface coverage in air-aged NQD suspensions results from changes in the composition of the NQD surface (e.g. partial oxidation) that may reduce the affinity of the ligand to the oxidized NQD surface. The oxidized species formed on different NQD facets are likely to be dissimilar vis-à-vis the differences in surface termination and reconstruction - the precise reconstruction and faceting is not yet fully understood and remains a subject of intensive investigation [25, 26]. We turned to X-ray photoelectron spectroscopy (XPS) to investigate changes in the chemical composition of the PbS NQDs. XP spectra were collected from thin films of NQDs drop-cast onto cleaned silicon substrates (exposure to ambient air was limited to less than 5 min during loading into the XPS chamber). We note that, considering the inelastic mean free path of the O(1s), Pb(4f), and S(2s) photoelectrons in PbS (1.8 - 2.6 nm) [27], XPS analysis gives disproportionate weight to the atoms on the outer surface of the particles, and that the majority of signal will be from the top few NQD layers.

XP spectra from the Pb(4f) region for the air-aged and N_2-aged PbS NQD films are displayed in Figure 7.3. Here the data is fit to two peak doublets; one attributed to Pb atoms in a sulfide binding environment (PbS), the other to Pb in a more highly oxidized state [Pb(ox)]. The difference in binding energies of the PbS and Pb(ox) peaks was 1.1 eV and 1.3 eV for the air-aged and N_2-aged samples, respectively. A number of oxidation products resulting in shifts in the Pb(4f) binding energy in the range of +0.9 to +1.5 eV are possible, depending on the conditions and the extent of surface exposure to the oxidizing agents [28-30]. Therefore, we will not assign a specific chemical structure to the high binding energy peak, though the most likely components are PbO, $Pb(OH)_2$, and $PbCO_3$ [28-30]. In the air-aged NQDs, the oxidized species accounts for 42% of the total area of the Pb(4f) feature, whereas for the N_2-aged film the oxidized species account for only 8%. In addition, the O/Pb atomic ratio was calculated to be 1.27 for the air-aged particles, and 0.91 for the N_2-aged particles (see Appendix E for details of XPS peak fitting and atomic ratio calculation). Taken together, the Pb(4f) peak fitting and the O/Pb ratio indicate that a higher proportion of lead atoms are oxidized in the air-aged NQD film.

Inspection of the S(2s) feature for the air-aged particles indicates that no significant S-containing oxidation products are present (Appendix E). For extensive air exposures, planar PbS is known to form sulfate species, which would be observed at ~ 7 eV above the sulfide component [31]. However, this was not observed in our NQD films. Notably, the S/Pb ratio was found to be 0.35 for the air-aged and 0.52 for the N_2-aged NQDs. Simultaneous increase in the oxygen content, the appearance of a high-binding energy component in the Pb(4f) feature, as well as a decrease in the S/Pb atomic ratio have been observed previously during the early stages of planar PbS oxidation [28]. The decrease in the S/Pb ratio upon oxidation likely indicates that the sulfur-containing oxidation products of PbS have sufficiently high vapor pressure to leave the surface under ultrahigh vacuum, or react with air prior to introduction into the vacuum chamber. Previous XPS studies have shown that elemental sulfur, for example, is only detected on the oxidized PbS surface if the sample is cooled to <150 K while under vacuum [28]. The ~33% decrease in relative S concentration, along with the increase of ~34% in the relative contribution of Pb(ox) to the Pb(4f) feature suggests that the near-surface sulfur atoms are being replaced by atmospheric O from O_2, H_2O, or CO_2.

The partial oxidation of PbS NQD surfaces indicated by the XPS study is qualitatively consistent with the reduced OA ligand coverage evidenced by the FTIR spectra. The oxidation of surface lead atoms would be accompanied by loss of oleate ligands based on a previous XPS analysis of PbS NQD by Weller that showed oleate binding to surface lead atoms [32]. Since the species and extent of oxidation across different NQD facets may be different it is likely that the detachment of ligand may also be more pronounced on specific NQD facets. At present, the precise determination of ligand coverage on specific NQD facets is beyond the capabilities of state-of-the-art characterization tools.

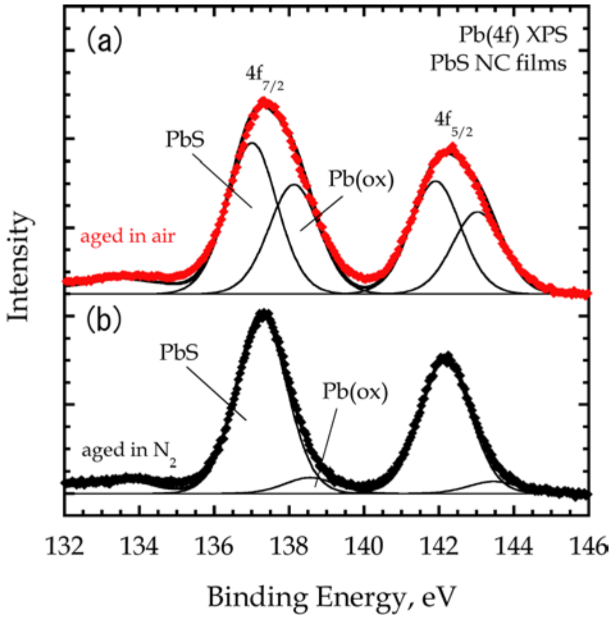

Figure 7.3: X-ray photoelectron spectra of films of air-aged (a) and N_2-aged (b) PbS NQDs. Spectra were fit assuming contributions from two chemical binding environments, one corresponding to PbS, the other to a more highly oxidized form of Pb. In the air-aged case, the more highly oxidized form accounts for 42% of the total area of the feature, while for the N_2 aged case the more highly oxidized form accounts for 8% of the total. The spectrum for air-aged NQDs has been shifted higher on the ordinate to facilitate presentation.

7.4 Calculations on facet specific binding energies

To get a better understanding of the physical and chemical nature of the NQD surface at atomic length scales, we turned to computational model and DFT analysis of ligand binding energies on different facets. We modeled $\{100\}_{\mathrm{NQD}}$ and $\{111\}_{\mathrm{NQD}}$ surfaces with atomic details and calculated binding energies of Pb acetate

($Pb(CH_3COO)_2$) on each facet (see Appendix E for detailed DFT methods). $Pb(CH_3COO)_2$ was chosen instead of Pb oleate [19, 32] for increased computational efficiency. The functional group, rather than the carbon chain length, is expected to dominate the binding.

PbS NQD surfaces were modeled with slabs consisting of four layers; only the atoms in the top layer were allowed to move during relaxation. For the $\{001\}_{NQD}$ surface, the cations and anions in the surface layer relaxed slightly inwards, reducing the layer spacing from the bulk value of 3.00 Å to about 2.82 Å. For the $\{111\}_{NQD}$ surface, the occurrence of a surface reconstruction was taken into account. Unreconstructed $\{111\}_{NQD}$ surfaces exhibit a very high surface energy [25]. The $\{111\}_{NQD}$ layers are comprised of oppositely charged layers of cations and anions resulting in a dipole moment perpendicular to the plane. Recently, Fang *et al.* [25] showed that the surface energy of $\{111\}_{NQD}$-terminated PbSe surfaces is reduced by more than an order of magnitude if alternating rows of cations in the topmost layer are removed. As such, each surface terminates in half a monolayer of cations above a full layer of anions; this approach to the reconstruction (referred from here on as the $\{111\}_{NQD}$-1/2-Pb reconstruction) has long been known to drastically reduce the surface energy of other polar ionic crystal surfaces [33]. Rutherford backscattering experiments suggest that real PbSe $\{111\}_{NQD}$ surfaces may be reconstructed along these lines; epitaxially grown PbSe was seen to terminate in a Pb layer which had an atomic density of about 40% [34]. After relaxation of the $\{111\}_{NQD}$-1/2-Pb reconstructed surface, the Pb atoms in the terminating layer shift slightly closer to the remainder of the slab, such that the separation between the surface Pb atoms and the neighboring S atoms is 2.6-2.8 Å.

The binding energy of $Pb(CH_3COO)_2$ on the reconstructed $\{111\}_{NQD}$ surface is calculated by placing the Pb atom of $Pb(CH_3COO)_2$ inside the “trench” resulting from the surface reconstruction, while for the $\{001\}_{NQD}$ slab, the Pb atom was placed above a surface S atom. In both cases a number of initial geometries for the acetate molecules were attempted, in order to find the geometry with the strongest binding energy in each case. The modeled $Pb(CH_3COO)_2$ molecules absorbed on $\{001\}_{NQD}$ and $\{111\}_{NQD}$ surfaces, after the system has been relaxed using DFT, are shown in Appendix E. The binding energies for $Pb(CH_3COO)_2$ on the $\{001\}_{NQD}$ and the reconstructed $\{111\}_{NQD}$ surfaces were calculated to be 0.616±0.017 eV and 0.962±0.012 eV, respectively.

Importantly, our DFT results indicate that the Pb-oleate ligands bind stronger to the $\{111\}_{NQD}$ facets than to the $\{100\}_{NQD}$ facets and provide important insights on facet specific ligand adsorption/detachment equilibrium. We emphasize here that organic ligands bound to the surface of an inorganic NQD core constitute a dynamic system. These dynamics are a well-established concept underlying the controlled nucleation and growth processes during NQD synthesis. Aside from stabilizing the growing NQD, the ligand attachment to specific NQD facets can be tailored to modify the relative growth rate of those facets and thereby enable the growth of nanostructures with complex 3-dimensional shapes [35]. At room temperature, the ligand dynamics in colloidal NQD suspensions are slowed down considerably, but the dynamics between bound and unbound ligands still play an important role [36]. Indeed, Moreels *et al.*

has observed this dynamic between bound and unbound lead oleate ligands on PbSe NQDs [19]. Our DFT results therefore provide insights on facet specific ligand loss equilibrium dynamics and indicate anisotropic ligand loss across different NQD facets – $\{100\}_{\mathrm{NQD}}$ facets will end up with reduced ligand coverage compared to the $\{111\}_{\mathrm{NQD}}$ facets.

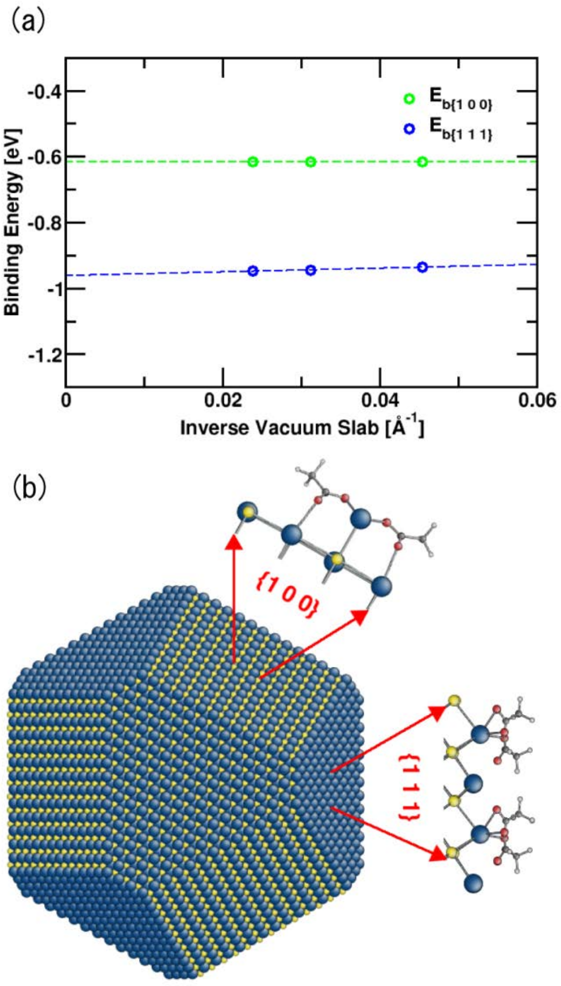

Figure 7.4: Density functional theory calculations of Pb-acetate molecule binding energies to the PbS {111} (blue), and {100} (green) surfaces. {111} surface was modeled after accounting for surface reconstructed (see the main text for details). This result indicates that the Pb-oleate ligands bind stronger to $\{111\}_{\mathrm{NQD}}$ facets than

$\{100\}_{NQD}$ facets and provide important insights on facet specific ligand adsorption/detachment equilibrium.

In conjunction with the XPS data, the DFT results suggest another possible mechanism of facet specific ligand loss – anisotropic ligand loss due to facet specific oxidation. Lead salt NQDs have been found to have a significant amount (~ 40 %) of excess lead atoms [37]. Comparing calculated energies required to put excess lead atoms on $\{111\}_{NQD}$ and $\{100\}_{NQD}$ facets, we reason that the excess lead atoms are more likely to be distributed on $\{111\}_{NQD}$ facets rather than $\{100\}_{NQD}$ facets. The dense distribution of excess Pb atoms on $\{111\}_{NQD}$ facets would bury the S atom layers underneath and thus block them from oxidation. This reasoning, along with our XPS data that show replacement of surface S atoms with O atoms, suggests that it is $\{100\}_{NQD}$ facets that are more readily being oxidized and thus losing ligands.

7.5 Discussion and conclusion

Given the experimental and computational results discussed so far, we now discuss how the detailed spatial arrangement of OA ligands on specific NQD facets influence interactions between NQDs during self-assembly of the superlattice. If we consider a fully passivated NQD with high ligand coverage, the dense ligand shell effectively masks the faceted shape of the NQD core and neighboring NQDs interact as soft spheres. On the other hand, lower surface coverage, especially due to anisotropic ligand loss across different facets, will enhance the NQD shape effect and the anisotropy of the NQD interaction volume. Variations in ligand coverage density resulting in ‘patchy’ particles has previously been recognized as an important parameter in the directed self-assembly of colloids [9], e.g. Janus particles [38], or isolated DNA-functionalized metal nanoparticle homodimers [39, 40]. Here, we illustrate that the anisotropic ligand coverage can also be exploited to control the translational and orientational order of NQD superlattices.

The eightfold coordination of NQDs in the *bcc* superlattice and the eightfold degeneracy of $\{111\}_{NQD}$ facets of individual PbS NQDs provides an important clue for understanding the relationship between facet specific ligand coverage and the assembly of the non-close packed *bcc* structure. The relationship between NQD faceting and orientational alignment is consistent with a recent molecular dynamics simulation by Fichthorn and Qin which illustrated that oscillatory solvation forces induce neighboring particles to rotate to approach each other via paths of minimum free energy [41].

Considering the detailed molecular interactions between surface bound ligands, another possible mechanism is that ligands on $\{111\}_{NQD}$ facets of neighboring NQDs will, through van der Waals interaction, be interdigitated or aligned with each other to form ‘artificial bonds’ to connect NQDs along specific crystallographic directions. In case of the truncated octahedral NQDs studied in this work, such ‘bonds’ between ligands bound to $\{111\}_{NQD}$ facets strengthen interactions along the eightfold $<111>_{SL}$ directions. We note that this interpretation is similar to earlier molecular dynamics simulations by Landman and Luedtke who predicted that ligands bound to the surface of Au NQDs arrange to form bundles [42]. The proposed formation of ‘ligand-bridges' connecting neighboring NQDs, as previously reported by Wang for metal NQD assemblies, is consistent with this picture [43].

In summary, we show how variations in ligand coverage on specific NQD facets may influence the interactions between NQDs during assembly into ordered superstructures. PbS NQDs with dense ligand coverage assemble into *fcc* superlattices. Reduced ligand coverage on aged and partially oxidized NQDs assemble into *bcc* superlattices with long range orientational order. Our experimental and computational results indicate that the assembly of the aged NQDs is influenced by anisotropic ligand coverage on $\{111\}_{NQD}$ and $\{100\}_{NQD}$ facets of truncated octahedral NQDs. The anisotropic ligand coverage amplifies the significance of the NQD core shape during assembly. Beyond the implications on NQD superlattice with controlled symmetries illustrated in this paper, improved understanding of ligand coverage and surface chemistry on specific NQD facets also provides important insights into the interactions responsible for the fusion of lead salt NQDs into 1D wires [44, 45] or 2D sheets [46].

BIBLIOGRAPHY

[1] J. J. Choi, C. R. Bealing, K. Bian, K. J. Hughes, W. Zhang, D.-M. Smilgies, R. G. Hennig, J. R. Engstrom, T. Hanrath, J. Am. Chem. Soc. **133**, 3131 (2011).

[2] G. Markovich, C. P. Collier, S. E. Henrichs, F. Remacle, R. D. Levine, J. R. Heath, Accounts of Chemical Research. **32**, 415 (1999).

[3] D. V. Talapin, J.-S. Lee, M. V. Kovalenko, E. V. Shevchenko, Chemical Reviews. **110**, 389 (2010).

[4] F. Remacle, R. Levine, ChemPhysChem. **2**, 20 (2001).

[5] M. P. Pileni, J. Phys. Chem. B. **105**, 3358 (2001).

[6] K. J. M. Bishop, C. E. Wilmer, S. Soh, B. A. Grzybowski, Small. **5**, 1600 (2009).

[7] Y. Min, M. Akbulut, K. Kristiansen, Y. Golan, J. Israelachvili, Nat Mater. **7**, 527 (2008).

[8] M. P. Pileni, Accounts of Chemical Research. **41**, 1799 (2008).

[9] M. Grzelczak, J. Vermant, E. M. Furst, L. M. Liz-Marzan, ACS Nano. **4**, 3591 (2010).

[10] R. L. Whetten, M. N. Shafigullin, J. T. Khoury, T. G. Schaaff, I. Vezmar, M. M. Alvarez, A. Wilkinson, Accounts of Chemical Research. **32**, 397 (1999).

[11] B. A. Korgel, D. Fitzmaurice, Physical Review B. **59**, 14191 (1999).

[12] W. Lu, Q. Liu, Z. Sun, J. He, C. Ezeolu, J. Fang, J Am Chem Soc. **130**, 6983 (2008).

[13] A.-I. Henry, A. Courty, M.-P. Pileni, P.-A. Albouy, J. Israelachvili, Nano Lett. **8**, 2000 (2008).

[14] D. V. Talapin, E. V. Shevchenko, C. B. Murray, A. V. Titov, P. Král, Nano Letters. **7**, 1213 (2007).

[15] K. Bian, J. J. Choi, A. Prakash, P. Clancy, D. M. Smilgies, T. Hanrath, ACS Nano, **5**, 2815 (2011).

[16] T. Hanrath, J. J. Choi, D.-M. Smilgies, ACS Nano. **3**, 2975 (2009).

[17] M. Sykora, A. Y. Koposov, J. A. McGuire, R. K. Schulze, O. Tretiak, J. M. Pietryga, V. I. Klimov, ACS Nano. **4**, 2021 (2010).

[18] Q. Dai, Y. Wang, Y. Zhang, X. Li, R. Li, B. Zou, J. Seo, Y. Wang, M. Liu, W. W. Yu, Langmuir. **25**, 12320 (2009).

[19] I. Moreels, B. Fritzinger, J. C. Martins, Z. Hens, Journal of the American Chemical Society. **130**, 15081 (2008).

[20] J. W. Stouwdam, J. Shan, F. C. J. M. van Veggel, A. G. Pattantyus-Abraham, J. F. Young, M. Raudsepp, Journal of Physical Chemistry C. **111**, 1086 (2007).

[21] C. Murray, S. Sun, W. Gaschler, H. Doyle, T. Betley, C. Kagan, IBM Journal of Research and Development. **45**, 47 (2001).

[22] C. M. Evans, L. Guo, J. J. Peterson, S. Maccagnano-Zacher, T. D. Krauss, Nano Lett. **8**, 2896 (2008).

[23] W. Yu, J. Falkner, B. Shih, V. Colvin, Chem Mater. **16**, 3318 (2004).

[24] I. Moreels, K. Lambert, D. Smeets, D. De Muynck, T. Nollet, J. C. Martins, F. Vanhaecke, A. Vantomme, C. Delerue, G. Allan, Z. Hens, ACS Nano. **3**, 3023 (2009).

[25] C. Fang, M. A. van Huis, D. l. Vanmaekelbergh, H. W. Zandbergen, ACS Nano. **4**, 211 (2010).

[26] V. Petkov, I. Moreels, Z. Hens, Y. Ren, Physical Review B. **81**, 241304 (2010).

[27] S. Tanuma, C. J. Powell, D. R. Penn, Surface and Interface Analysis. **17**, 927 (1991).

[28] A. N. Buckley, R. Woods, Applications of Surface Science. **17**, 401 (1984).

[29] P. Nowak, K. Laajalehto, Applied Surface Science. **157**, 101 (2000).

[30] D. S. Zingg, D. M. Hercules, The Journal of Physical Chemistry. **82**, 1992 (1978).

[31] S. Evans, E. Raftery, Journal of the Chemical Society, Faraday Transactions 1. **78**, 3545 (1982).

[32] A. Lobo, T. Moller, M. Nagel, H. Borchert, S. Hickey, H. Weller, J Phys Chem B. **109**, 17422 (2005).

[33] J. T. Kummer, Y.-F. Y. Yao, Canadian Journal of Chemistry. **45**, 421 (1967).

[34] K. Kimura, K. Nakajima, Y. Fujii, M.-h. Mannami, Surface Science. **318**, 363 (1994).

[35] A. G. Kanaras, C. Sonnichsen, H. Liu, A. P. Alivisatos, Nano Letters. **5**, 2164 (2005).

[36] B. Kim, L. Avila, L. Brus, I. Herman, Appl Phys Lett. **76**, 3715 (2000).

[37] I. Moreels, K. Lambert, D. De Muynck, F. Vanhaecke, D. Poelman, J. C. Martins, G. Allan, Z. Hens, Chemistry of Materials. **19**, 6101 (2007).

[38] S. Jiang, Q. Chen, M. Tripathy, E. Luijten, K. S. Schweizer, S. Granick, Adv Mater. **22**, 1060 (2010).

[39] X. Xu, N. L. Rosi, Y. Wang, F. Huo, C. A. Mirkin, J Am Chem Soc. **128**, 9286 (2006).

[40] M. M. Maye, D. Nykypanchuk, M. Cuisinier, D. van der Lelie, O. Gang, Nat Mater. **8**, 388 (2009).

[41] K. A. Fichthorn, Y. Qin, Ind Eng Chem Res. **45**, 5477 (2006).

[42] W. D. Luedtke, U. Landman, The Journal of Physical Chemistry. **100**, 13323 (1996).

[43] Z. L. Wang, Advanced Materials. **10**, 13 (1998).

[44] K.-S. Cho, D. V. Talapin, W. Gaschler, C. B. Murray, Journal of the American Chemical Society. **127**, 7140 (2005).

[45] P. Schapotschnikow, M. A. van Huis, H. W. Zandbergen, D. Vanmaekelbergh, T. J. H. Vlugt, Nano Lett. **10**, 3966 (2010).

[46] C. Schliehe, B. H. Juarez, M. Pelletier, S. Jander, D. Greshnykh, M. Nagel, A. Meyer, S. Foerster, A. Kornowski, C. Klinke, H. Weller, Science. **329**, 550 (2010).

CHAPTER 8

FUTURE DIRECTIONS

8.1 NQD energy levels

As discussed in chapter 1, 3 and 4, the advances so far in synthetic control over the size and shape of NQDs and various characterization techniques have revealed much insight on the tunable energy levels of NQDs. However, there are still many unknowns regarding energy levels of NQDs - the two major remaining frontiers are (1) understanding effect of surface chemistry on absolute energy level locations and (2) advanced separation techniques for further improvement of monodispersity in NQD populations. For topic (1), previous studies have shown that the surface chemistry can shift the HOMO-LUMO energy levels of NQD by as large as 0.4 eV [1, 2]. The binding group of the ligand molecules seem to have bigger influence than the overall structure and dipole moments associated to the ligand molecules [1, 2] but the exact causes are still unclear. Obtaining better understanding and control over the effects of surface chemistry on NQD energy levels will allow rational selection of NQD energy levels tailored for targeted optoelectronic device applications. For topic (2), advances in NQD synthetic techniques so far have improved the monodispersity of as-synthesized NQDs within the size distribution of one atomic lattice constant. Compared to the size control, information on the distribution of ligand grafting density among the NQD population is still not well known. Most studies so far have reported only the average ligand density without information on the distribution [3, 4]. Recent report employing ultracentrifugation has shown much promise in accurate characterization of ligand grafting density distribution [5] and additional studies are expected to reveal more insights. In general, NQDs can be considered to be in the same material class as polymers due to their polydispersity and need for statistical description of the ensemble [6] and tapping into the established separation techniques employed for polymeric materials may provide efficient routes for obtaining NQDs with extremely small polydispersity [5, 7, 8].

Here, I note that the discussion in this section touches upon an important research area in the field of NQD – the surface science of NQDs. Arguably, the unknowns in the surface of NQDs are the biggest challenges in the advancement of NQD science and technology. Astoundingly little is known about the surface of NQDs due to the inherent complexity of NQD surfaces and challenges related to characterization of precise crystal and molecular structures on various facets of NQD surfaces. Figure 8.1 illustrates the complexity of NQD surfaces and the ensuing knowledge gap compared to the advanced surface science of single crystalline surfaces. Because of the presence of nanoscale facets, it is extremely challenging to predict and characterize the distribution of surface facets, exact crystal structure of each facet, bonding and structural characteristics of the bridge molecules at different facets. Without the precise knowledge on the surface structures, it is difficult to systematically study the structure-property relationships of NQDs and their superstructures. There are largely two big unknowns - structure of nanoscale facets and different surface chemistry at each facet. In terms of structural unknowns, advanced electron microscopy and X-ray diffraction techniques may shed more light on the distribution of nanoscale facets and structures [9-14]. In terms of surface chemistry, the identity of various surface species, their type of bonding and binding energies on different facets are still not fully understood. Because of the unknowns, rational selection of molecules for ligand exchange chemistry or synthesis of shape tuned NQDs have been difficult and results have largely been obtained empirically. Many new findings regarding the NQD surface chemistry are still surfacing even after decades intense research - for example, the existence of X-type binding of anionic ligand binding to excess surface Cd^{2+} ions on CdSe NQD surface in addition to dative L-type binding sites has only recently been discovered whereas conventionally CdSe NQDs were thought to be passivated with L-type ligands only [15]. Lead salt NQDs have been found to have excess surface lead species and it is not yet fully known how they are distributed, charge balanced and bonded at different facets [16]. Recent studies have shown that the excess surface atoms may be asymmetrically distributed among different facets depending on their binding energy [3, 17]. More studies on facet specific surface chemistry are needed to obtain better understanding and control of ligand binding on different facets.

More insights on nanoscale structure of NQD facets and how different molecules bind to different facets will have huge impact in the NQD field - ranging from enabling finer control over synthesis of NQDs with various shapes and aspect ratio[17, 18] to providing rational knowledge base to design NQD optoelectronic devices.

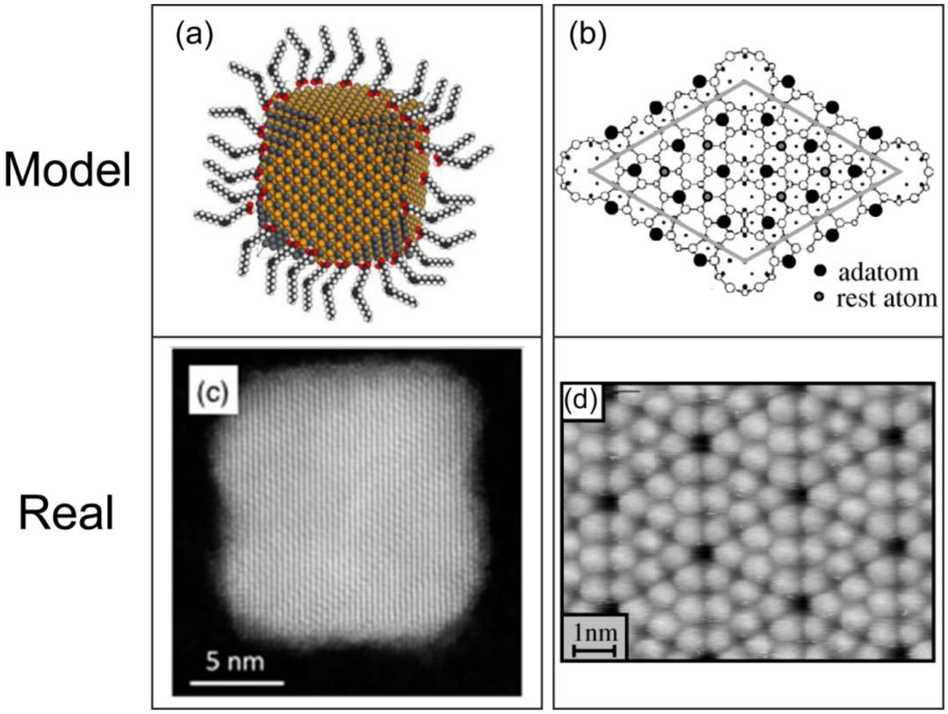

Figure 8.1: Comparison of NQD and single crystalline surface as systems for surface science. Disparity between (a) the simplified schematic of oleate surface ligand passivated PbS NQDs with well-defined {100} and {111} facets and (c) high resolution TEM of real PbS NQDs that reveal complex distribution of surface facets is contrasted with the good agreement between (a) dimer-adatom-stacking fault model of the Si(111)-(7x7) surface and (d) scanning force microscopic image of the real system. (Adapted from [19] Copyright 2000 American Physical Society)

8.2 Inter-NQD coupling

Studies and references presented in chapter 5 and 6 of this thesis clearly illustrate that different surface molecules critically influence charge transfer and transport in NQD systems but the precise mechanisms are still not fully understood. The NQD community has so far has been largely focused on the charge *transfer* aspects of the systems where the electronic structures of the NQDs as the charge donors and various charge acceptor materials are mainly considered whereas the linker molecules placed between the NQDs and the acceptor (bridge molecules) are simply approximated as potential barriers. In the future, closer inspection of the NQD systems in the context of the *charge transport through the bridge molecules* in which the detailed physical and electronic structure of the bridge molecules are considered may generate deeper understanding and finer control over charge transfer/transport dynamics in NQD systems. Many physical and electronic aspects of the bridge molecules such as length, energy level location, degree of conjugation, conformation, orientation and end group moieties are expected to have major influence over the electronic coupling and charge transfer in NQD systems. Systematic studies on these topics have been sparse and, in most studies so far, bridge molecules have been simply taken to be potential barriers for the charge tunneling between the donor-acceptor pair. Deeper understanding and faster progress are anticipated if systematic investigation on the effect of other aspects of bridge molecules mentioned above.

I propose that drawing connections to the molecular electronics community whom has accumulated extensive and insightful knowledge base over the last three decades on the topic of charge transport through single molecules [20-29] may accelerate the progress in the NQD field. The similarity between the experimental systems employed for studying charge transport in the fields of molecular electronics and charge transfer in NQDs is noteworthy (Figure 8.2). Both cases can be approached in the context of donor-bridge-acceptor classification [20, 22] where the molecule 'bridge' connects the donor and acceptor of electrical charges (Figure 8.2A). The donor and acceptor pair can be any combination of NQDs, molecules, semiconductors or metals, with different physics to consider in each case. Most of the molecular electronics studies rely on methods such as scanning probes and break junctions that allow electrical contacts to individual molecules with metals (Figure 8.2B) or electrochemical and spectroscopic kinetic studies of charge transfer between molecular donor and acceptor through the bridge molecule [20, 22-24, 26, 28, 29]. Similarly, many studies on NQDs have relied on bridge molecules to modulate electronic coupling and charge transfer between the donor and acceptor pair, where the donor is a NQD and the acceptor can be another NQD (Figure 8.2C), other semiconductor materials or metal electrodes. Once established, I believe that robust connections between the NQD and molecular electronics communities will not only allow better experimental designs and deeper insights from the results but also inspire novel research directions for both communities.

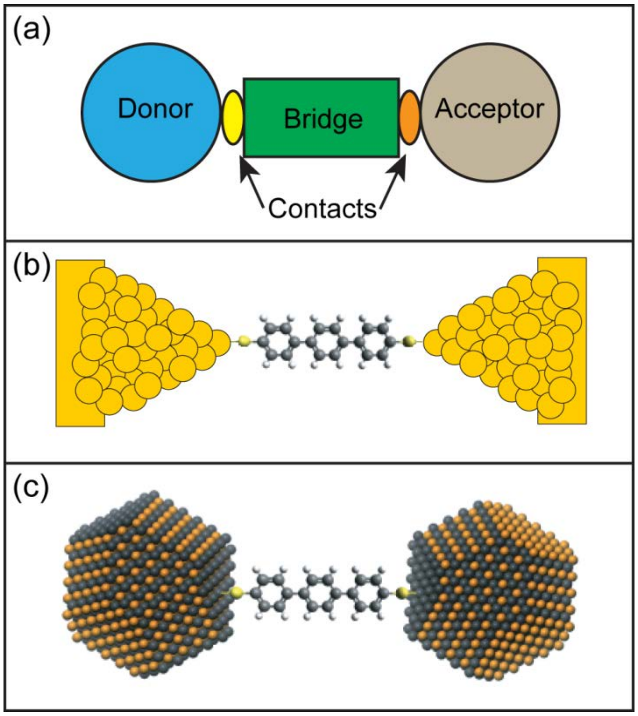

Figure 8.2: Similarity between systems for experimental and theoretical studies in molecular electronics and charge transfer in NQDs in the context of donor-bridge-acceptor classification.

8.3 NQD superlattice structure

Understanding mechanisms behind NQD self-assembly will be crucial in studying NQD superstructures in the context of artificial solids and successful development of NQD device applications. There is much to be studied in this area due to the complexity of nanoscale interactions of NQDs [30]. As recent studies have illustrated the importance of ligand interactions in determining the shape of NQD interaction potentials [31-33] and more studies are needed to understand and control the strength of ligand interactions by changing solvents, ligand structure, length and etc. Ultimately, deeper insights in the self-assembly process of NQDs will allow preparation of superstructures of NQDs with high translational and orientational order that exhibit large electronic coupling and coherent properties.

BIBLIOGRAPHY

[1] M. Soreni-Harari, N. Yaacobi-Gross, D. Steiner, A. Aharoni, U. Banin, O. Millo, N. Tessler, Nano Lett. **8**, 678 (2008).

[2] J. Jasieniak, M. Califano, S. Watkins, ACS Nano 110612110216029 (2011).

[3] J. J. Choi, C. R. Bealing, K. Bian, K. J. Hughes, W. Zhang, D.-M. Smilgies, R. G. Hennig, J. R. Engstrom, T. Hanrath, Journal of the American Chemical Society. **133**, 3131 (2011).

[4] I. Moreels, B. Fritzinger, J. C. Martins, Z. Hens, Journal of the American Chemical Society. **130**, 15081 (2008).

[5] R. P. Carney, J. Y. Kim, H. Qian, R. Jin, H. Mehenni, F. Stellacci, O. M. Bakr, Nature Communications. **2**, 335 (2011).

[6] D. V. Talapin, Y. Yin, Journal of Materials Chemistry. **21**, 11454 (2011).

[7] J. P. Wilcoxon, J. E. Martin, P. Provencio, Langmuir. **16**, 9912 (2000).

[8] A. M. Al-Somali, K. M. Krueger, J. C. Falkner, V. L. Colvin, Anal. Chem. **76**, 5903 (2004).

[9] M. J. Yacaman, J. A. Ascencio, H. B. Liu, J. Gardea-Torresdey, Journal of Vacuum Science & Technology B: Microelectronics and Nanometer Structures. **19**, 1091 (2001).

[10] S. J. L. Billinge, I. Levin, Science. **316**, 561 (2007).

[11] P. D. Jadzinsky, G. Calero, C. J. Ackerson, D. A. Bushnell, R. D. Kornberg, Science. **318**, 430 (2007).

[12] C. Fang, M. A. van Huis, D. l. Vanmaekelbergh, H. W. Zandbergen, ACS Nano. **4**, 211 (2009).

[13] S. V. Aert, K. J. Batenburg, M. D. Rossell, R. Erni, G. V. Tendeloo, Nature. **470**, 374 (2011).

[14] M. C. Scott, C.-C. Chen, M. Mecklenburg, C. Zhu, R. Xu, P. Ercius, U. Dahmen, B. C. Regan, J. Miao, Nature. **483**, 444 (2012).

[15] J. S. Owen, J. Park, P.-E. Trudeau, A. P. Alivisatos, J. Am. Chem. Soc. **130**, 12279 (2008).

[16] I. Moreels, K. Lambert, D. De Muynck, F. Vanhaecke, D. Poelman, J. C. Martins, G. Allan, Z. Hens, Chemistry of Materials. **19**, 6101 (2007).

[17] C. R. Bealing, W. J. Baumgardner, J. J. Choi, T. Hanrath, R. G. Hennig, ACS Nano. **6**, 2118 (2012).

[18] C.-Y. Chiu, Y. Li, L. Ruan, X. Ye, C. B. Murray, Y. Huang, Nature Chemistry. **3**, 393 (2011).

[19] Lantz, Hug, P. J. van Schendel, Hoffmann, Martin, Baratoff, Abdurixit, Guntherodt, Gerber, Physical Review Letters. **84**, 2642 (2000).

[20] M. A. Ratner, J. Jortner, Molecular Electronics, Blackwell, Oxford, UK, 1997.

[21] A. Nitzan, Annual Review of Physical Chemistry. **52**, 681 (2001).

[22] D. M. Adams, L. Brus, C. E. D. Chidsey, S. Creager, C. Creutz, C. R. Kagan, P. V. Kamat, M. Lieberman, S. Lindsay, R. A. Marcus, R. M. Metzger, M. E. Michel-Beyerle, J. R. Miller, M. D. Newton, D. R. Rolison, O. Sankey, K. S. Schanze, J. Yardley, X. Zhu, J. Phys. Chem. B. **107**, 6668 (2003).

[23] R. M. Metzger, Chem. Rev. **103**, 3803 (2003).

[24] A. Nitzan, M. A. Ratner, Science. **300**, 1384 (2003).

[25] A. Salomon, D. Cahen, S. Lindsay, J. Tomfohr, V. B. Engelkes, C. D. Frisbie, Advanced Materials. **15**, 1881 (2003).

[26] X. Y. Zhu, Surface Science Reports. **56**, 1 (2004).

[27] B. Albinsson, M. P. Eng, K. Pettersson, M. U. Winters, Phys. Chem. Chem. Phys. **9**, 5847 (2007).

[28] F. Chen, J. Hihath, Z. Huang, X. Li, N. J. Tao, Annual Review of Physical Chemistry. **58**, 535 (2007).

[29] R. L. McCreery, A. J. Bergren, Advanced Materials. **21**, 4303 (2009).

[30] K. J. M. Bishop, C. E. Wilmer, S. Soh, B. A. Grzybowski, Small. **5**, 1600 (2009).

[31] K. Bian, J. J. Choi, A. Kaushik, P. Clancy, D.-M. Smilgies, T. Hanrath, ACS Nano. **5**, 2815 (2011).

[32] J. J. Choi, C. R. Bealing, K. Bian, K. J. Hughes, W. Zhang, D.-M. Smilgies, R. G. Hennig, J. R. Engstrom, T. Hanrath, J. Am. Chem. Soc. **133**, 3131 (2011).

[33] Y. Zhang, F. Lu, D. van der Lelie, O. Gang, Physical Review Letters. **107**, 135701 (2011).

APPENDIX A

SUPPLEMENTARY INFORMATION: EFFECT OF NQD ENERGY LEVEL LOCATIONS ON PHOTOVOLTAIC BEHAVIOR[1]

A.1 Synthesis of 2 – 10nm PbSe NQDs

PbSe NQDs were prepared following the method reported by Yu et al. [2] The synthesis was carried out in a three-necked flask under an inert nitrogen atmosphere. In a typical synthesis, PbO (4 mmol) and oleic acid (10 mmol) were dissolved in 1-octadecene (ODE) to yield a precursor solution with [Pb] = 0.3 M and a molar Pb:oleic acid ratio of 1:2.5. The solution was then degassed by heating to $160^{o}C$ for 1 hour under flowing nitrogen. In a glovebox, Se was dissolved in trioctylphosphine (TOP) to yield a 1 M stock solution. Small amount of diphenylphospine (DPP) (4.5 mM) was added to the TOPSe solution. 12 ml of the 1 M TOP-Se solution was rapidly injected into the vigorously stirred, hot lead oleate solution. PbSe nanocrystals formed immediately after injection and their size was tuned through adjustments in temperature ($120\text{-}180^{o}C$), reaction time (0.2-5 min), and molar Pb:oleic acid ratio (1:6 to 1:3). After the elapsed reaction time, the solution was quenched by transferring the flask to a water bath. Following synthesis, the nanocrystals were washed several times by sequential precipitation with ethanol and redispersion in anhydrous hexane.

---

[1] The results presented in this chapter have been published in Ref [1].

A.2 Synthesis of <2nm PbSe NQDs

Small (<2nm) PbSe NQDs were prepared with similar method reported by Evans et al. [3] In a typical synthesis, 1.78g (8 mmol) of PbO and 10mL of oleic acid were dissolved in ODE and then heated to 150^{o}C for 1 hour under nitrogen to form lead oleate. The solution was then cooled down to 30 to 60 ^{o}C depending on the desired reaction temperature. In a glovebox, 1.42g of selenium was dissolved in 18mL of TOP. 16mL of the TOP-Se was rapidly injected into the lead oleate solution. Reaction temperature was set between 30 ^{o}C and 60 ^{o}C and the reaction time was between 30 minutes to 4 hours depending on the reaction temperature and desired NQD size.

A.3 Cyclic Voltammetry

Samples for electrochemical characterization were prepared by spin-casting (1000 rpm; 60 sec) or drop-casting a 5 – 10 mg/mL as-synthesized PbSe NQDs with oleic acid ligands in chlorobenzene onto a glassy carbon electrode. The electrode was then protected by direct light and allowed to dry. The glassy carbon electrode was then immersed in acetonitirile solution containing 0.1M tetra-*n*-butylammonium perchlorate (TBAP). Silver wire was used as quasi-reference electrode and platinum wire was used as counter electrode. The cell potential was calibrated using ferrocene/ferrocinium couple. A BAS-27 W potentiostat was used to perform the experiments. Data were digitally recorded using WinDaq® Serial Acquisition software (DATAQ Instruments). All experiments were done in a glove box to avoid particle oxidation with water and oxygen. Following the procedure from our previous work with PbS NQDs,[1] the lowest unoccupied molecular orbital (LUMO) of PbSe NQD was determined from the value of the first reduction peak location in CV data (examples shown in Figure 3.2B) and the highest occupied molecular orbital (HOMO) was determined by subtracting optically measured energy gap from the LUMO value. The correction due to exciton binding energy was ignored since it is smaller effect than the precision of CV measurement. [4]

Control experiment shows just the glassy carbon (no peak)

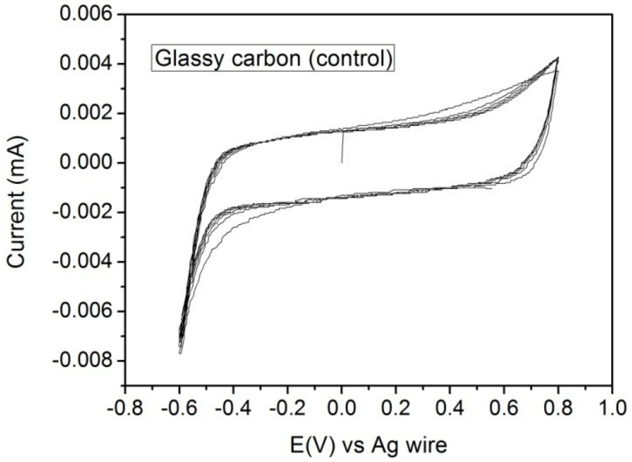

Figure A.1: Cyclic voltammogram of glassy carbon (control)

Following plots show cyclic voltammograms from 6.5nm PbSe NQD. First scan shows a peak at -0.1V.

CV analysis was based on peak position instead of peak onset. After each scan, the peak showed a negative shift with increased signal up to around -0.25V and continued the negative shift up to -0.4V while the signal is getting reduced. This complex trend illustrates a number of factors that must be taken into consideration in the electrochemical analysis of NQDs [5, 6]. It is suspected that irreversible electrochemical reaction forms film of different chemical species on the working electrode and in that case the first scan would be the most trustworthy data. Three runs were performed and they showed that the result is reproducible with error of ~0.1eV.

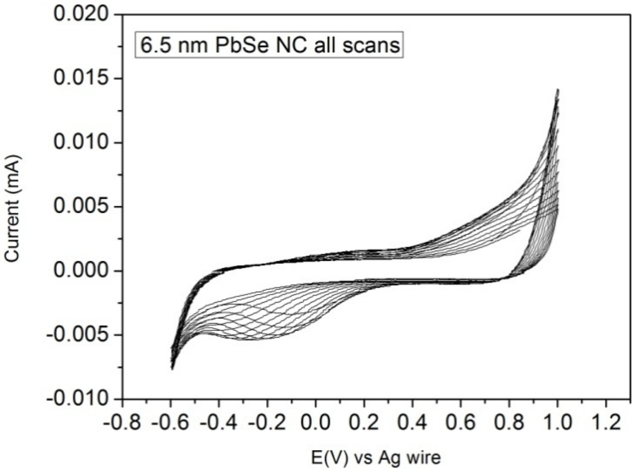

Figure A.2: Sequential scans from CV of 6.5 nm PbSe NQD. Shift in reduction peak is observed.

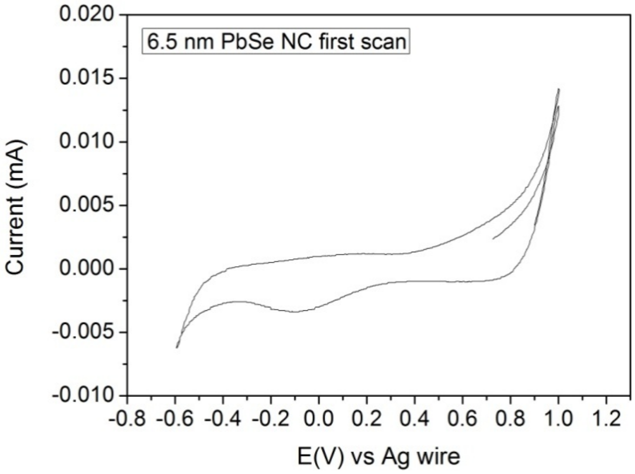

Figure A.3: First scan from CV of 6.5 nm PbSe NQD

There were other complexities associated with the cyclic voltammograms. First of all, the first oxidation peaks usually showed sharply rising current while their locations did not show any trend with the diameter of NQD. We attribute these oxidation peaks to decomposition of PbSe NQD [6]. We found this oxidation peak important in ‘activation’ of the NQDs. In all cases, the voltage had to be swept toward positive voltage far enough for the first oxidation peak occur before the reduction sweep. If the voltage was swept toward negative voltage first, no reduction peak was observed in first scan and it only appeared in second scan after the first oxidation peak. Another complexity with the CV data is that, there were additional reduction and oxidation peaks that are not yet fully identified. We suspect the peaks to be from chemical species produced by NQD decomposition or unbound ligands. Further electrochemical and analytical studies are needed for full understanding. Despite the above mentioned complexity, the location of first reduction peak that correspond to NQD LUMO level showed consistent trend that depends on the NQD diameter. Thus, we focused on the location of the first reduction peak to extract the most pertinent and consistent information on NQD energy levels.

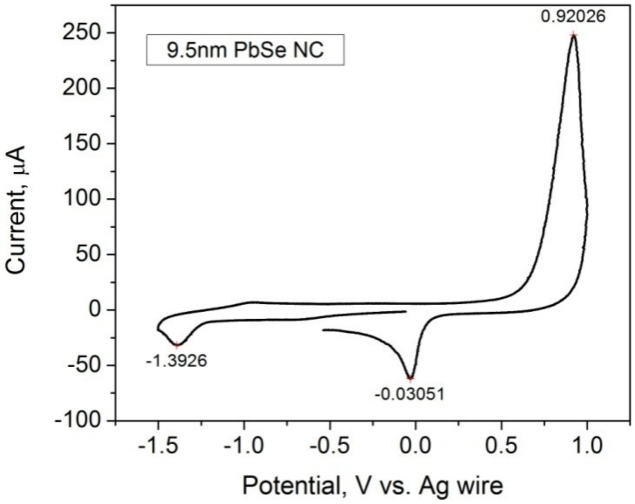

Figure A.4: CV of 9.5 nm PbSe NQD

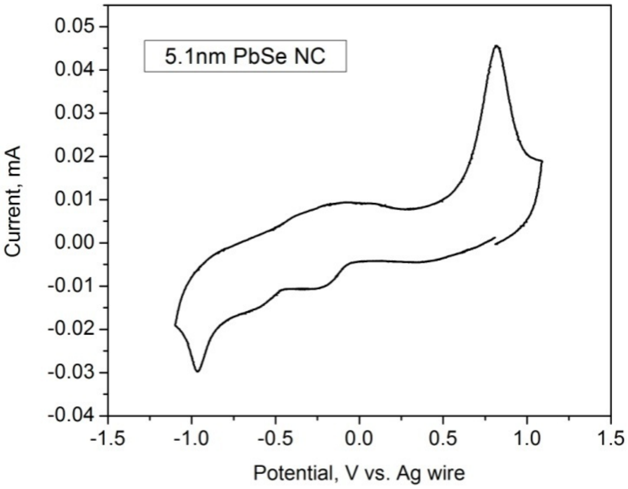

Figure A.5: CV of 5.1 nm PbSe NQD

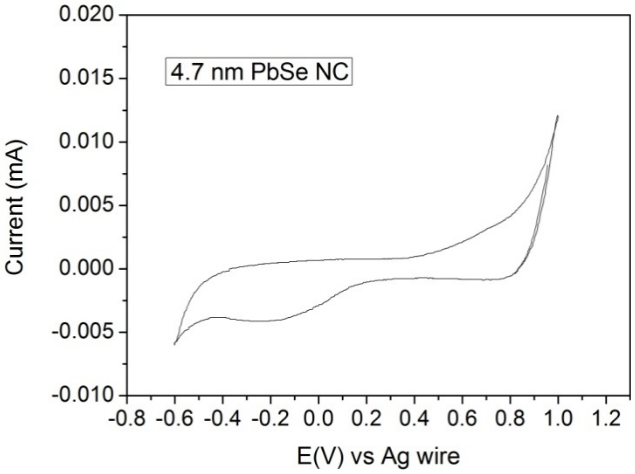

Figure A.6: CV of 4.7 nm PbSe NQD

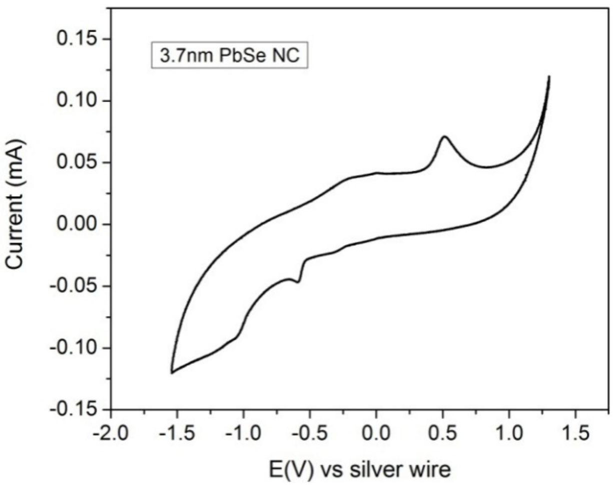

Figure A.7: CV of 3.7 nm PbSe NQD

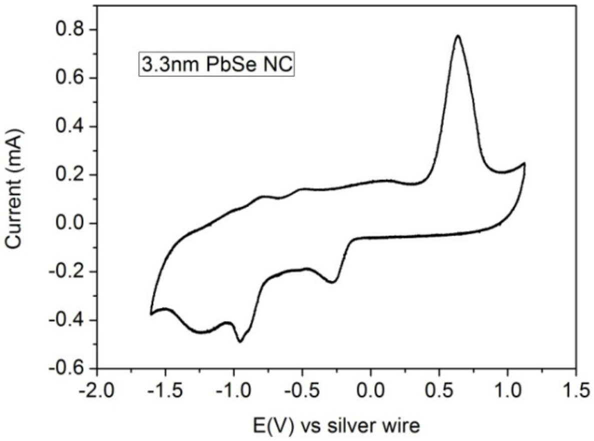

Figure A.8: CV of 3.3 nm PbSe NQD

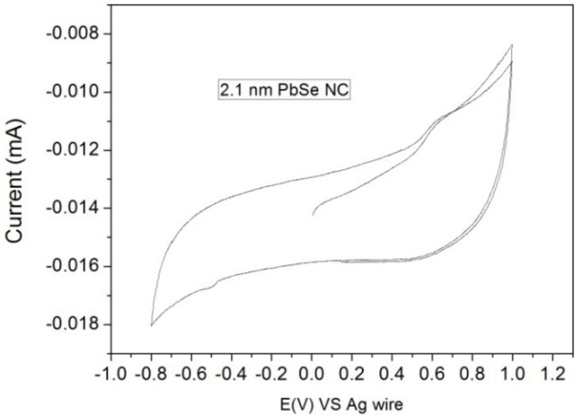

Figure A.9: CV of 2.1 nm PbSe NQD

A.4 ZnO nanoparticle synthesis

ZnO particles were prepared based on adaptation of the method reported by Beek et al. [7] In a typical synthesis, 4.425g of zinc acetate dihydrate was dissolved in 190mL of methanol and the solution temperature was set to 60 °C. In a separate container, 2.17g of KOH was dissolved in 97mL methanol with vigorous stirring. The KOH solution was then added to the zinc acetate dehydrate solution and the solution was left under stirring with temperature at 60 °C. After 2.5 hours, the heater and stirrer were removed and the solution was allowed to cool down slowly for 1 hour. The ZnO nanoparticle product was collected by centrifuging the solution. The collected ZnO nanoparticles were washed three times by redispersion in pure methanol and centrifuging.

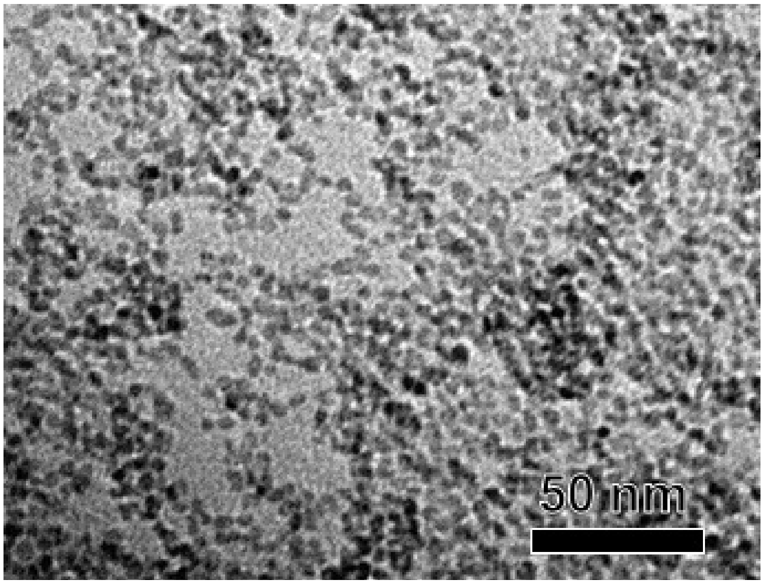

Figure A.10: TEM picture of ZnO nanoparticles

A.5 Photovoltaic device fabrication and characterization

Pre-patterned ITO coated glass substrates from Kintec, Hong Kong were cleaned by sonication in a mild detergent, rinsed with de-ionized water. The substrates were then dried in a nitrogen stream and treated with UV-ozone for 10 minutes. PEDOT:PSS

PH500 from H.C. Starck was filtered through 0.45 µm PVDF syringe filter and then spun-casted on the cleaned ITO substrate at 6000 rpm for 1 minute. The deposited PEDOT:PSS was then baked on a hot plate at 170 ^{o}C for 4 minutes to remove residual solvent. The samples were then transferred into a glovebox in which all subsequent processing steps were carried out. To reproducibly deposit PbSe NQD film, we used 'sequential spin-casting' method instead of using layer-by-layer dip coating method. 10 – 20mg/mL of PbSe NQD in chlorobenzene solution was spun-cast on top of PEDOT:PSS layer at 1000 rpm for 1 minute. 0.1M of ethanedithiol (EDT) in acetonitrile solution was then dispensed on top of deposited PbSe NQD film, left there for 1 minute and then spun-cast. Alternatively, the sample with deposited PbSe NQDs film can be taken out of the spin-coater and rinsed with 0.1M EDT solution and then put back on the spin-coater. We found that both ways work well. Pure acetonitrile was then dispensed on top of the film and spun-cast to remove residual free standing EDT molecules. Pure chlorobenzene was dispensed on top of the film and spun-cast to remove ligand exchanged oleate molecules. This completes one cycle of the 'sequential spin-casting'. Three cycles of depositions were performed to form crack-free PbSe NQDs films (see Figure 3.3C). After deposition of PbSe NQD film, 40mg/mL of ZnO nanoparticles in chloroform was spun-cast at 1000 rpm for 1 minute. Then 800Å of aluminum was thermally evaporated to form the top electrode. The aluminum evaporation was set at 1 Å/sec for first 100 Å and 4 Å/sec for the rest of the deposition. The photovoltaic device testing was performed with Keithley 236 source-measurement-unit under 100mW/cm^2 AM1.5 illumination from Solar Light 16S-002 solar simulator. Light output power was calibrated with Newport 818P-010-

12 thermopile high power detector. Spectral mismatch was not taken into account in these measurements.

A.6 Photodoping of ZnO layer

Following plot shows the effect of UV photodoping of ZnO layer in 3.1 nm PbSe NQD device. For all devices, UV exposure was needed to 'activate' the devices. The photodoping process happened almost immediately (within 5 seconds). Without UV exposure, the devices showed low conductivity with no rectification. The device was tested in following order: (1) measurement in dark prior to any light exposure (2) measurement in light with 455 nm cut-off filter (3) measurement in light with 455 nm filter removed (4) measurement in dark after the full light exposure.

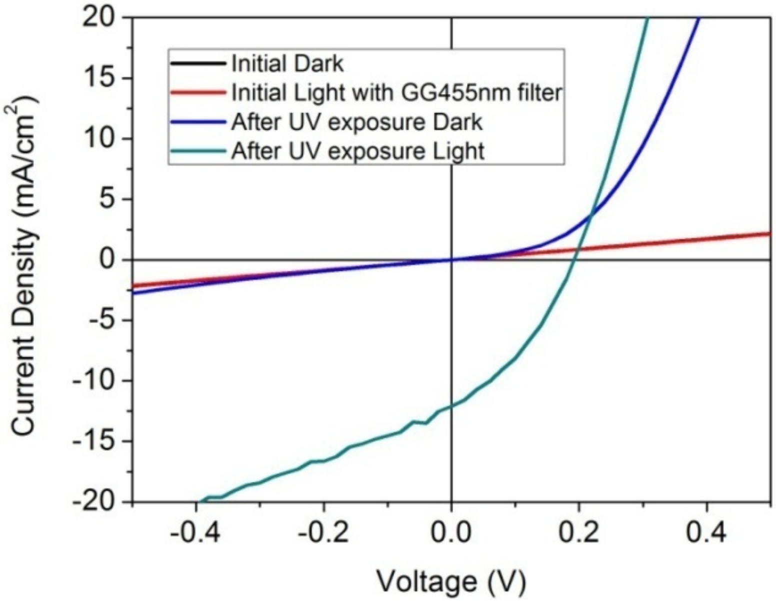

Figure A.11: Effect of photodoping of ZnO layer on device behavior

A.7 Effect of Absence of ZnO and PEDOT:PSS layers on Device Performance

Following control experiment samples were fabricated with PbSe NQD from the same reaction batch of NQD used for ZnO UV photodoping experiment discussed above. They show that presence of ZnO and PEDOT:PSS layers improve the V_{oc} by relying excitonic solar cell mechanism instead of Schottky junction for charge separation. The device without ZnO layer did not require any UV photodoping as expected.

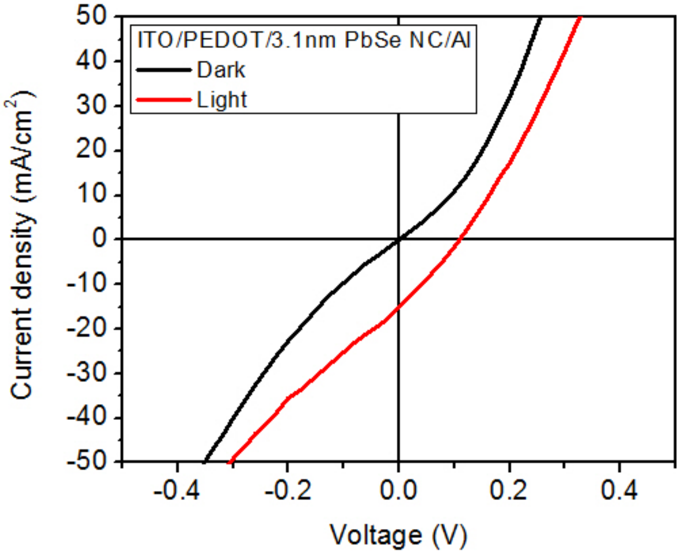

Figure A.12: Absence of ZnO layer significantly reduces the V_{oc} and rectification

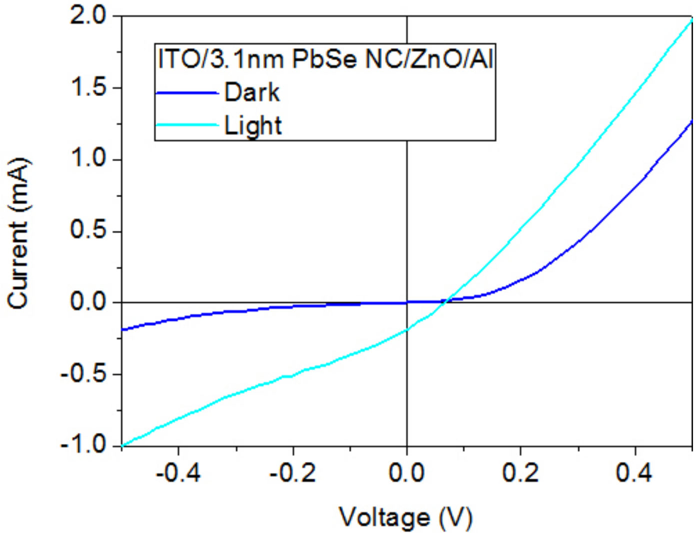

Figure A.13: Absence of PEDOT:PSS layer significantly reduces the V_{oc}

A.8 Control Experiment on Effect of Film Thickness Variation on Device Characteristic

All our devices studied in the main text had relatively thin PbSe NQD films of 40 – 50 nm thickness to allow V_{oc} to be mainly determined by the energy level offset at the interfaces. To check for the effect of film thickness variation on V_{oc}, we have compared current-voltage characteristics of devices with 40 nm PbSe NQD film and 80 nm PbSe NQD film and observed no change in V_{oc}. The PbSe NQDs and ZnO nanoparticles used for this experiment were taken from same batches and all other device fabrication steps were identical except for varying the PbSe NQD film thickness. The fact that 80 nm thick film gave higher short-circuit current suggests that 40 – 50 nm films are indeed shorter than the diffusion and junction lengths and V_{oc} from our devices is highly dependent on the energy level offsets at the interfaces.

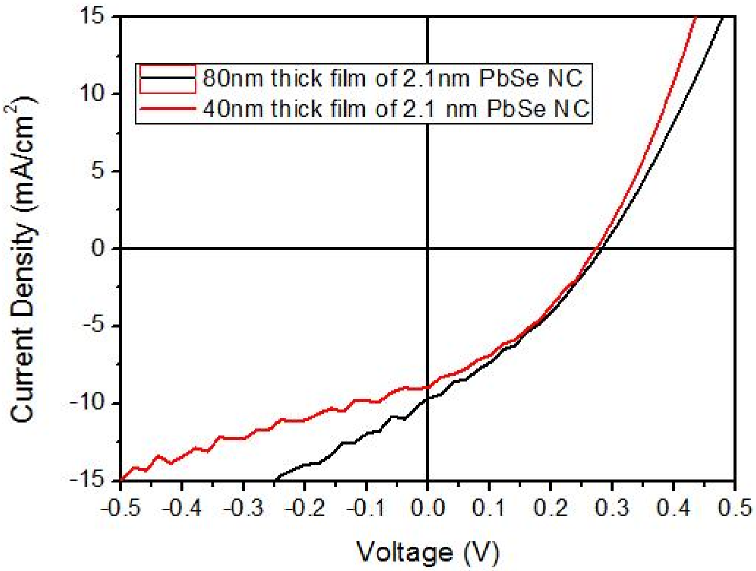

Figure A.14: Effect of PbSe NQD film thickness variation on device characteristics

BIBLIOGRAPHY

[1] J. J. Choi, Y.-F. Lim, M. B. Santiago-Berrios, M. Oh, B.-R. Hyun, L. Sun, A. C. Bartnik, A. Goedhart, G. G. Malliaras, H. D. Abruna, F. W. Wise, T. Hanrath, Nano Letters. **9**, 3749 (2009).

[2] W. W. Yu, J. C. Falkner, B. S. Shih, V. L. Colvin, Chemistry of Materials. **16**, 3318 (2004).

[3] C. M. Evans, L. Guo, J. J. Peterson, S. Maccagnano-Zacher, T. D. Krauss, Nano Letters. **8**, 2896 (2008).

[4] B.-R. Hyun, Y.-W. Zhong, A. C. Bartnik, L. Sun, H. D. Abruna, F. W. Wise, J. D. Goodreau, J. R. Matthews, T. M. Leslie, N. F. Borrelli, ACS Nano. **2**, 2206 (2008).

[5] S. K. Haram, B. M. Quinn, A. J. Bard, Journal of the American Chemical Society. **123**, 8860 (2001).

[6] L. Sun, L. Bao, B.-R. Hyun, A. C. Bartnik, Y.-W. Zhong, J. C. Reed, D.-W. Pang, H. c. D. Abruna, G. G. Malliaras, F. W. Wise, Nano Letters. **9**, 789 (2009).

[7] W. J. E. Beek, M. M. Wienk, M. Kemerink, X. Yang, R. A. J. Janssen, The Journal of Physical Chemistry B. **109**, 9505 (2005).

APPENDIX B

SUPPLEMENTARY INFORMATION: NANOCRYSTAL QUANTUM DOT TANDEM SOLAR CELLS[1]

B.1 Synthesis of Materials

PbS NQD synthesis: The PbS synthesis followed the work by Hines and Scholes [2]. The synthesis was carried out in a three-necked flask under an inert nitrogen atmosphere. In a typical synthesis, 3 mmol of PbO was mixed with oleic acid in a 1:2 to 1:25 molar ratio, depending on the desired NQD size. An appropriate amount of 1-octadecene (ODE) was added to make the total volume of solution 30 mL. The solution was degassed by heating to 150^oC for 1 hour under flowing nitrogen. In a glovebox, 378 µL of *bis*(trimethylsilyl)sulfide (TMS) was dissolved in 18 mL of ODE and stirred thoroughly. A 15 mL aliquot of the TMS solution was rapidly injected into a vigorously stirred, hot lead oleate solution held at a temperature between 90 and 150 ^oC (depending on desired NQD size). PbS NQDs formed immediately after injection and were collected after 1 minute of reaction. Following synthesis, the NQDs were washed several times by sequential precipitation with ethanol and redisperson in hexane.

ZnO nanoparticle synthesis: The ZnO was synthesised in ambient air using an adaptation of a previously published method [3]. 1.76 g of zinc acetate dihydrate was dissolved in 150 mL of ethanol with vigorous stirring and heated to 60 ^oC for 1 hour.

---

[1] The results presented in this chapter have been published in Ref [1].

Parafilm was used to block solvent evaporation during the heating and the entire reaction time. In a separate container, 6.4 mL of a tetramethyl ammonium hydroxide (TMAH) solution (28% in MeOH) was added to 50 mL of ethanol. Over 10 minutes, the TMAH solution was slowly added to the zinc acetate solution at regular intervals. During this time the temperature of the zinc acetate solution was maintained at 60 ^{o}C with continuous stirring. Subsequently, the solution was heated at 60 ^{o}C for 30 minutes after which the heater and stirrer were removed. After cooling to room temperature, the solution was kept refrigerated at ~ 5 ^{o}C. This mother-liquor solution was stable for over ~5 months. ZnO nanoparticles were collected from the refrigerated solution immediately before device fabrication. To prepare devices, 5 mL of the solution was typically mixed with 20 mL of hexane to precipitate the ZnO particles. After centrifugation, the supernatant was removed and the white precipitate was dissolved in a 1:2 by volume chlorobenzene:methanol mixture.

B.2 Device Fabrication and Characterization

Tandem cell fabrication: Pre-patterned ITO-coated glass substrates were cleaned and treated with UV-ozone for 10 minutes. PEDOT:PSS (Product No. AI4083, H.C. Starck) was filtered through 0.45 μm PVDF syringe filter and spin-cast onto the cleaned ITO substrate at 6000 rpm for 1 minute and baked on a hot plate at 170 ^{o}C for 4 minutes. PbS NQDs for the front cell were spin-cast from a 30 mg/mL chlorobenzene solution at 1000 rpm for 30 seconds. The NQD film was then treated with a 0.1M solution of ethanedithiol (EDT) in acetonitrile and rinsed with pure acetonitrile and chlorobenzene by dispensing the solution on top of film and spin-casting at 1000 rpm for 30 seconds. This protocol constituted one cycle of the PbS NQD layer deposition. Typically, three cycles of depositions were performed. After deposition of the PbS NQD film, 20 mg/mL of a ZnO nanoparticle solution was spin-cast at 1000 rpm for 1 minute. Three such depositions of ZnO nanoparticles were carried out to ensure complete coverage. Following ZnO deposition, 10 Å of Au, Ag or Al was thermally evaporated in ultrahigh vacuum (~10^{-6} Torr) at a rate of 0.1 Å/second. The pH 7 PEDOT:PSS layer for the interlayer was spin-cast on top to complete the interlayer. Subsequently, a PbS NQDs layer and a ZnO layer were deposited with identical methods mentioned above. For the top electrode, 600 Å of aluminum was deposited via thermal evaporation in ultrahigh vacuum (~10^{-6} Torr). The entire device fabrication sequence, except for the metal evaporation step, was performed in ambient air. The completed devices were tested after 3 hours of air exposure.

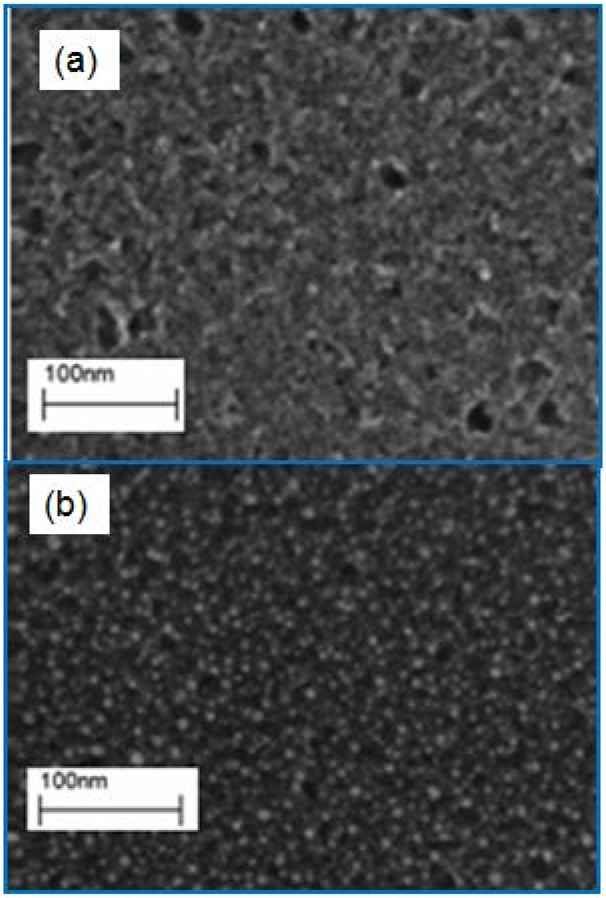

Figure B.1: SEM image of the (top) ZnO layer surface and (bottom) ZnO layer surface with 1 nm of thermally deposited Au. The gold layer forms nanoscale islands instead of a continuous layer.

Device characterization: Device testing was performed with a source measurement unit (Keithley 236). Samples were irradiated with 100mW/cm^2 AM1.5 illumination from a Solar Light 16S-002 solar simulator. Light output power was calibrated with a Newport 818P-010-12 thermopile high power detector. Small spectral mismatch was not taken into account in these measurements. External quantum efficiency measurements were performed with a PV Measurements QEX7 IPCE system. The probe beam was produced from a xenon light source and a monochrometer whose output was chopped at 100 Hz for modulation. Bias light for the front cell was produced from a UV lamp with power density of 20 W/m^2. Bias light for the back cell was from a broad band white light source (Newport 10LWF-800-B 815 ~ 1200 nm bandpass filter, 200 W/m^2). Absorptance spectra of the device stacks were taken with a Shimadzu UV-3101PC UV/Vis/Near-IR Spectrophotometer and an ISR-3100 integrating sphere, a photomultiplier tube, and a PbS detector.

B.3 Kelvin Probe Force Microscopy Measurements

Kelvin Probe Force Microscopy: KPFM measurements were carried out in a custom-built vacuum apparatus operating at room temperature. A Pt-Au coated cantilever (SPMtips model NSC18- Pt/Au) with a spring constant of 1 N/m, resonance frequency of 80 kHz, and a quality factor of 8000 (at a pressure of 10^{-6} mbar) was used. Cantilever displacement was detected with a fiber-optic interferometer operating at 1310 nm with an output power of 100 microwatts. The tip-sample separation was 30 nm. For imaging of local electrostatic potential, tip voltage was modulated with a 100 mV zero-to-peak sine wave applied at the cantilever resonance frequency. Cantilever motion was demodulated using a commercial FPGA (RHK PLLpro 1.0; bandwidth = 400 Hz). During imaging, a DC voltage to cantilever tip was adjusted via feedback to keep the cantilever amplitude zero at 80 kHz, using an analog PID controller with (typical) coefficients (P=-.01, I= 2 Hz, D=.5 ms).

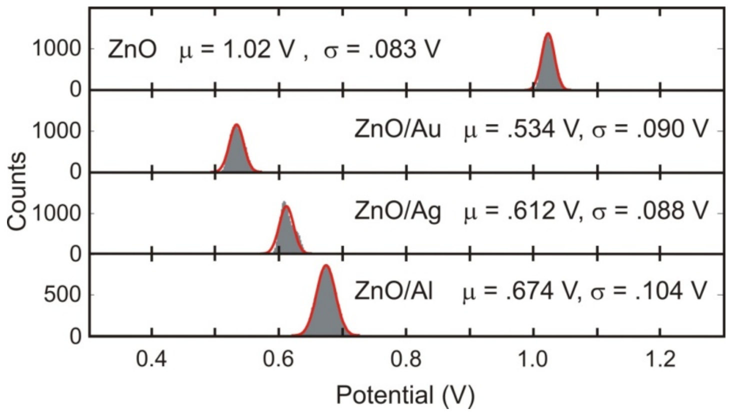

Figure B.2: Histogram of the surface potential, measured via Kelvin probe force microscopy, of the bare ZnO layer and ZnO with various metals on top. The presence of metal layers increases the surface workfunction. Data were fit to Gaussian distribution and their means and standard deviations are shown in the figure.

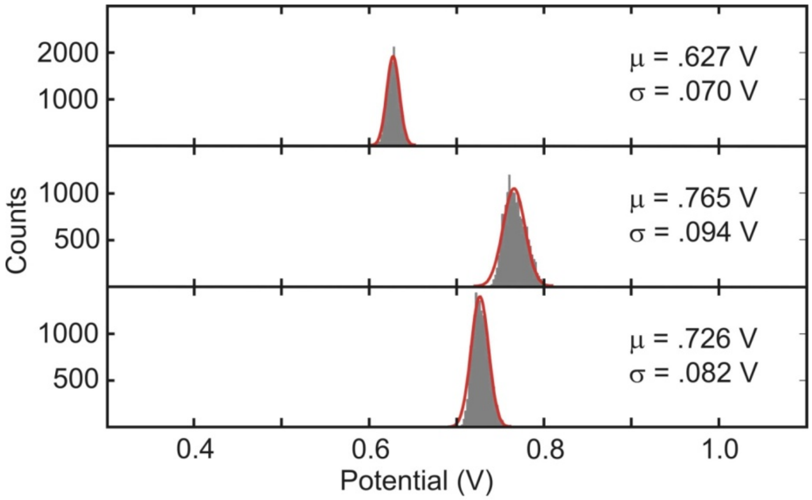

Figure B.3: Histogram of the KPFM-measured surface potential over three ITO/ZnO samples. Data was fit to a Gaussian, with mean and standard deviation reported. The sample-to-sample variation in the contact potential had a standard deviation of 0.069 V. The cantilever used for these measurements is different than the cantilever used for the workfunction measurements in the body of the paper, and should have a slightly different tip workfunction.

B.4 NQD energy gap combination and thickness optimization

Initial optimization efforts have determined the best combination of the NQD energy gaps in the front and back cell to be 1.6 eV and 1.0 eV, respectively. Notably, this is close to the optimal combination of bandgaps estimated from detailed balance calculations assuming two terminal series tandem cell configuration. With other combinations, for example, using bigger energy gap NQD (1.85 eV) for the front cell while maintaining similar film thickness resulted in a higher device open-circuit voltage of V_{oc} = 1.04 V but a lower J_{sc} and ultimately lower power conversion efficiency. The need for further optimization of NQD film thickness guided by optical modeling of the absorptance in each layer is clearly indicated. These studies are currently underway.

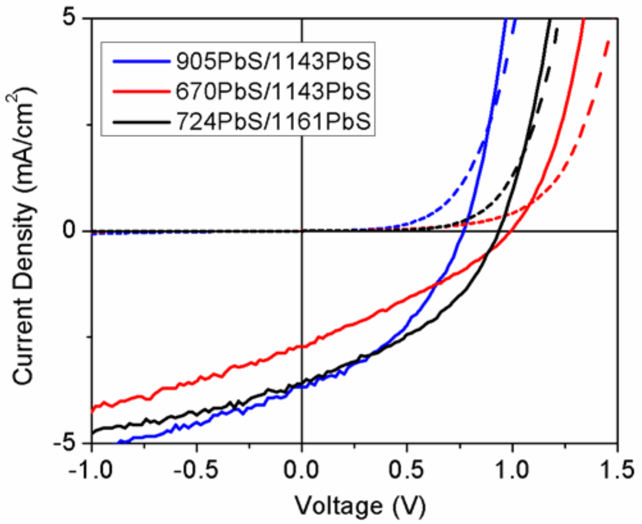

Figure B.4: J-V curves of tandem cells fabricated using various NC energy gap combinations.

A preliminary study of thicker absorber layers revealed charge transfer limitations which would have obscured the study of interlayer effects at the focus of this study. Better charge transport through PbS NQD layers or structured interfaces with increased area for charge transfer will allow thicker NQD layers for more light absorption. With further optimization guided by theoretical analysis, we believe that even higher current densities are within reach.

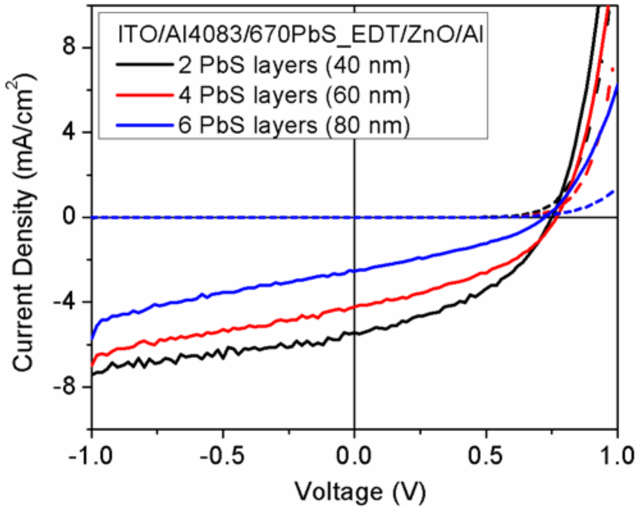

Figure B.5: Optimization of the control single-layer junction shows that the thinnest PbS NQD film gives the highest current density.

B.5 Effect of ZnO synthesis method on interlayer performance

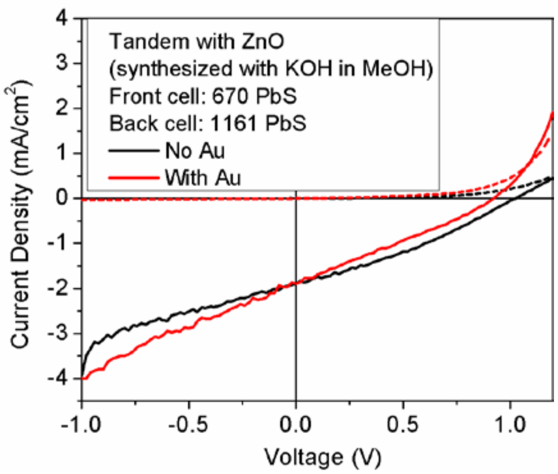

Figure B.6: Tandem cells with ZnO nanoparticles used in Gilot et al. (synthesized with KOH) show an Ohmic junction at the interlayer when made without a thin metal layer.

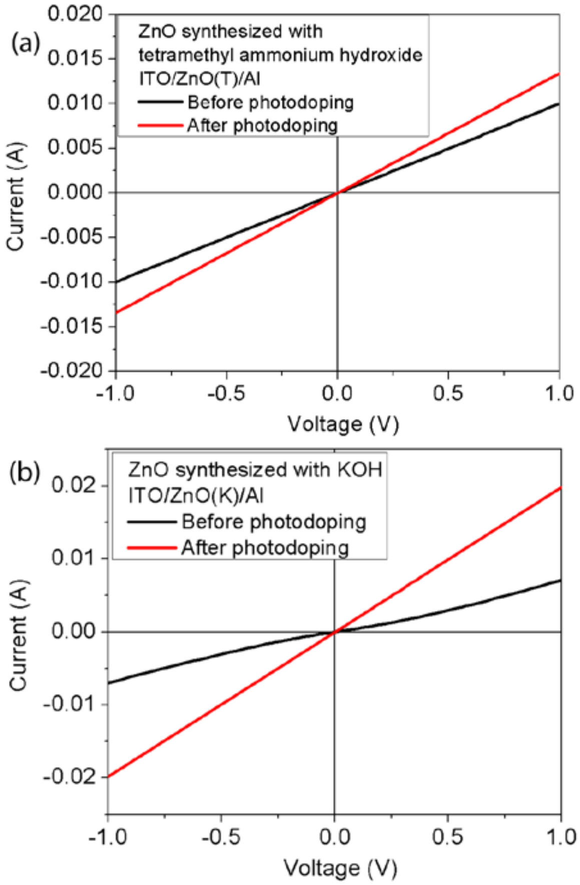

Figure B.7: ZnO synthesized with tetramethyl ammonium hydroxide (a) shows less degree of photo-doping then ZnO synthesized with KOH (b).

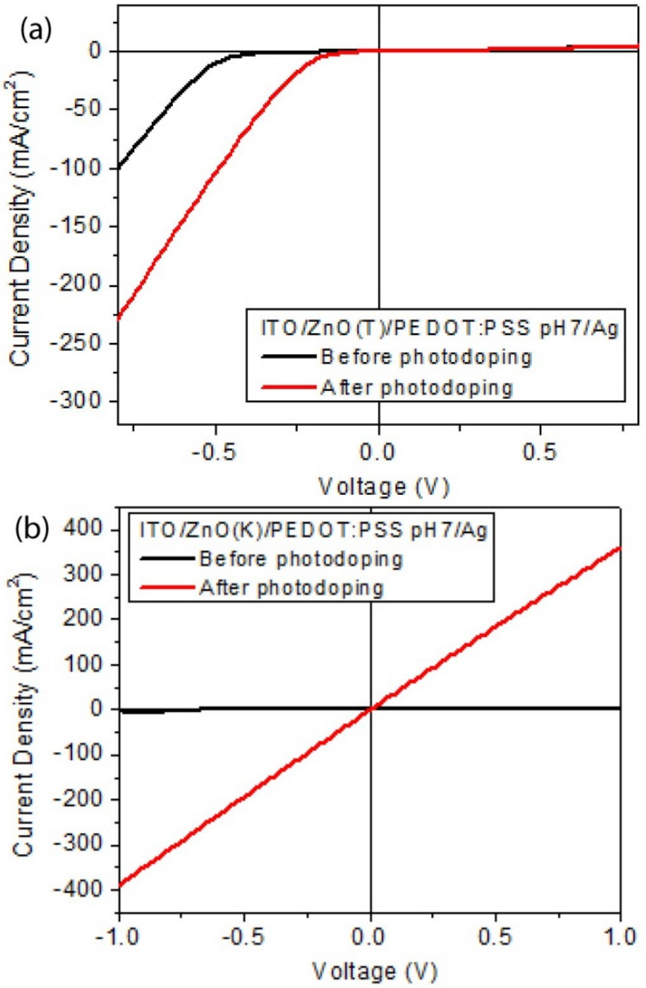

Figure B.8: (a) ZnO synthesized with tetramethyl ammonium hydroxide does not form an Ohmic junction with pH =7 PEDOT:PSS even after 1 hour of photo-doping. (b) ZnO synthesized with KOH, in contrast, forms an Ohmic junction with pH=7 PEDOT:PSS within one minute of photo-doping.

BIBLIOGRAPHY

[1] J. J. Choi, W. N. Wenger, R. S. Hoffman, Y.-F. Lim, J. Luria, J. Jasieniak, J. A. Marohn, T. Hanrath, Advanced Materials. **23**, 3144 (2011).

[2] M. A. Hines, G. D. Scholes, Advanced Materials. **15**, 1844 (2003).

[3] A. Wood, M. Giersig, M. Hilgendorff, A. Vilas-Campos, L. M. Liz-Marzán, P. Mulvaney, Aust. J. Chem. **56**, 1051 (2003).

APPENDIX C

SUPPLEMENTARY INFORMATION: INTER-NQD COUPLING INDUCED PHOTOGENERATED EXCITON DISSOCIATION[1]

C.1 NQD Synthesis

The synthesis procedure for 2.7 nm PbS NQDs was as follows. PbO (0.66g) and oleic acid (1.9 mL) were dissolved in 28 ml of 1-octadecence (ODE). The solution was then degassed and heated to 150 ^{o}C for 1 hour under flowing nitrogen to form a lead oleate precursor solution. In a glovebox, 380 µL of bis(trimethylsilyl)sulfide (TMS) was dissolved in 18 mL of ODE and stirred thoroughly. The lead oleate precursor solution was cooled to 90 ^{o}C prior to TMS solution injection. 15 mL of the TMS solution was rapidly injected into the vigorously stirred lead oleate solution. PbS NQDs formed immediately after injection and they were collected after 1 minute of reaction at 90 ^{o}C. Following the synthesis, the NQDs were washed several times by sequential precipitation with ethanol and redispersion in anhydrous hexane.

C.2 Close packed NQD assembly preparation

The samples were prepared inside a glovebox. As-synthesized NQDs were dissolved in hexane to make a 10 mg/mL solution. 100 µL of the NQD solution was drop-cast on a cleaned 25 mm by 25 mm by 1 mm glass slide. The glass slide with deposited

---

[1] The results presented in this chapter have been published in Ref [1].

NQD film was then put on a spin-coater. For EDT ligand treatment, 300 µL of 0.1 M EDT in acetonitrile solution was dispensed on top of the NQD film, and after a delay of 1 minute, we spun at 1000 rpm for 1 minute. The treated film was rinsed with pure acetonitrile and chlorobenzene. Cross-linking of NQDs by EDT prevents the NQD from dissolving into chlorobenzene. For BDT, DBDT and TBDT treatment, 0.01M of nBDT in a toluene solution was dispensed on top of the NQD film. After 1 minute, the nBDT solution was spun away at 1000 rpm for 1 minute. The treated films were rinsed with pure toluene. Cross-linking of NQDs by nBDT prevents the NQD from dissolving into toluene. The prepared PbS_nBDT films were then sealed by putting another cleaned 25 mm by 25 mm by 1 mm glass slide on top and sealing the sides with epoxy. Encapsulated samples were stable against oxidation for several months.

C.3 Chemical and structural characterization of the NQD assemblies

A Bruker Optics – Vertex80v FT-IR spectrometer was used for FTIR characterization of PbS_nBDT samples. GISAXS measurements were performed on beam line D1 of the Cornell High Energy Synchrotron Source (CHESS) using monochromatic radiation of wavelength $\lambda = 1.2373$ Å with a bandwidth $\Delta\lambda/\lambda$ of 1.5%. The X-ray beam was produced by a hardbent dipole magnet of the Cornell storage ring and monochromatized with Mo:B_4C synthetic multilayers with a period of 30 Å. The D1 area detector (MedOptics) is a fiber-coupled CCD camera with a pixel size of 46.9 µm by 46.9 µm and a total of 1024 × 1024 pixels with a 14-bit dynamical range per pixel. Typical read-out time per image was below 5 s. The images were dark-current corrected, distortion-corrected, and flat-field corrected by the acquisition software. The sample-to-detector distance was 660.2 mm, as determined using a silver behenate powder standard. The incident angle of the X-ray beam was at 0.25 degree. Typical exposure times ranged from 0.1 to 1.0 s. Scattering images were calibrated and integrated using the Fit2D software package.

C.4 Optical characterization of the NQD assemblies

Absorption spectra were recorded with an integrating sphere, a tungsten-halogen white-light source (Spectral Products ASTN-W-050), a monochromator and a Si photodiode. Emission spectra were recorded at room temperature with a fluorometer equipped with a 200-mm focal length monochromator, a single mode fiber coupled laser source (S1FC635PM, 635 nm, Thorlabs, Inc) as the excitation source, and a Si photodiode.

For tPL measurements, the samples were excited at a repetition rate of 1 kHz by frequency doubled (400 nm) femtosecond pulses of a Ti:sapphire laser system with a regenerative amplifier. The pump fluence was kept low so that the average number of exciton per NQD was ~ 0.1. Fluorescence was monitored with a Si avalanche photodiode (APD) single photon counting module (PerkinElmer, SPCM-AQRH-44-FC). For PbS_OA samples, the output was fed into a multichannel scalar (Stanford Research Systems, SR430), which provides an instrument response of a 5.2 nanoseconds, and adequate dynamic range to monitor decay times in the microsecond range. For PbS_nBDT samples with lifetimes in the sub-microsecond range, tPL measurements were performed in the time-correlated single photon counting (TCSPC) mode with a TCSPC board (PicoQuant, TimeHarp 200) and a digital delay generator (Stanford Research Systems, DG645) under right-angle sample geometry. The tPL curves were analyzed by means of iterative re-convolution using the FluoFit software package (version.4.4)

C.5 Electric Force Microscopy Measurement Method

Electric force microscope measurements were carried out in a custom-built vacuum apparatus operating at room temperature. We employed a Pt-Au coated cantilever (SPMtips model NSC18-Pt/Au) with a spring constant of k = 1 N/m, resonance frequency of f_0 = 80 kHz, and a quality factor of Q = 8000 (at a pressure of 10-6 mbar). Cantilever displacement was detected with a fiber-optic interferometer operating at 1310 nm [2]. Measurements were carried out using a cantilever peak-to-peak oscillation amplitude of ~325 nm and a tip-sample separation of 60 nm.

Simultaneous imaging of local electrostatic potential and capacitance was accomplished as follows. The tip voltage was modulated at frequency f_m = 200 Hz, deviations in cantilever frequency were detected using a commercial frequency demodulator (RHK PLLpro 1.0; bandwidth = 400 Hz), and lock-in detection was used to measure the Fourier components of the cantilever frequency deviation δf at the first (f_m) and second (2 f_m) harmonics of the modulation frequency [3]. The zero-to-peak amplitude of the voltage modulation V_m was between 1 and 3 V. A dc voltage was also applied to the tip and it was adjusted, via feedback, to keep the Fourier component $\delta\hat{f}(f_m)$ zero; the required tip voltage equals the local electrostatic potential. For these measurements we used a lock-in time constant of 30 ms and an analog PID controller with (typical) coefficients $P = 1$, $I = 2$ Hz, and $D = 3$ ms. The optimal PID coefficients were sensitive to the absolute capacitance, so the coefficients were adjusted for each sample to ensure a critically-damped response of the photo-potential; the measured capacitance was insensitive to the exact PID coefficients. The second derivative of tip-sample capacitance C with respect to tip-sample separation z displayed in Figure 5.3 was obtained from the measured second harmonic of the cantilever frequency deviation $\delta\hat{f}(2f_m)$ (lock-in time constant 50 ms) using

$$\frac{\partial^2 C}{\partial z^2} = \frac{9k\partial\hat{f}(2f_m)}{f_0 V_m^2} \qquad (\mathrm{C.1})$$

Samples were illuminated with an InGaN white LED (LiteOn model LTW-1KHC5). The LED was located approximately ~1 cm away from the cantilever tip and inclined at a forty five degree angle with respect to the sample surface. The LED spectrum had two peaks: a narrow emission centered at λ ~ 460 nm (FWHM ~ 25 nm; relative intensity ~ 1) and a broad emission at λ ~ 460 nm (FWHM ~ 100 nm; relative intensity ~ 0.45). The PbS_OA and PbS_nBDT thin films were drop-cast on interdigitated gold electrodes (thickness = 40 nm; channel length = 5 microns) fabricated by optical lithography, evaporation, and lift-off onto a glass substrate.

C.6 Density function theory calculation of nBDT molecule energy levels

All calculations were performed with the Gaussian 03 suite of programs [4]. Gradient corrected density functional theory (DFT) calculations with hybrid B3LYP [5, 6] (Beck's three-parameter nonlocal-exchange functional of Lee, Yang, and Parr) functional and the 6-31g(d) basis set were used for all geometry optimizations and energy calculations.

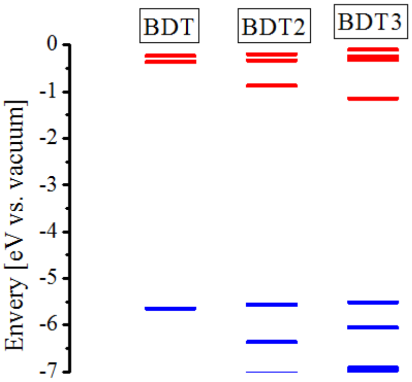

Figure C.1: Comparison of nBDT molecule energy levels calculated by DFT.

C.7 GISAXS scattering results

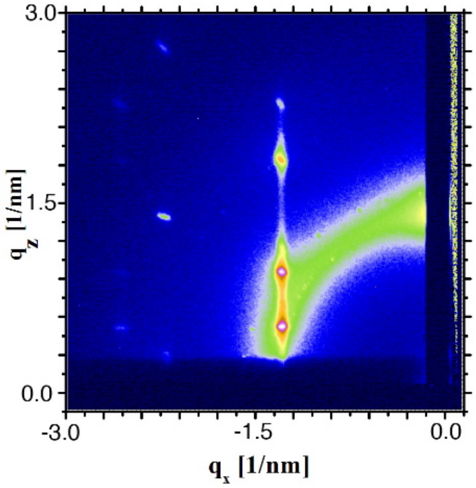

Figure C.2: The GISAXS scattering plot of the PbS_OA assembly is characteristic of a well ordered face centered cubic packing with close-packed $(111)_s$ planes parallel to the substrate**.**

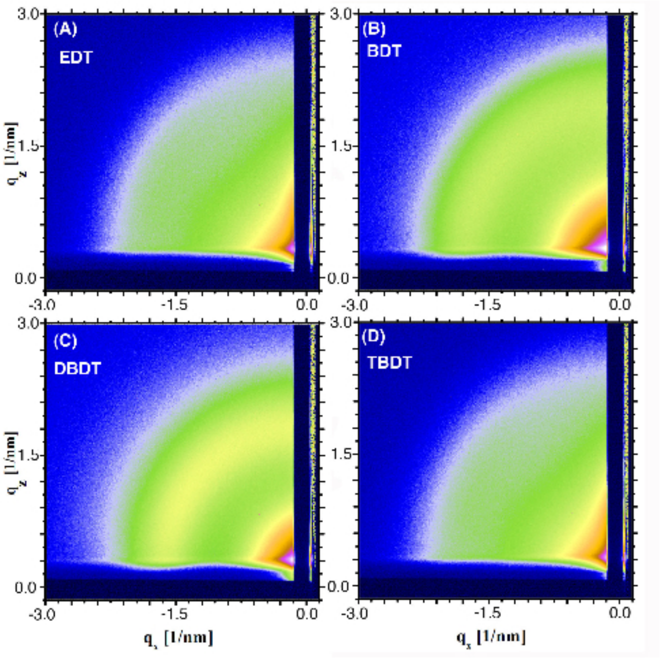

Figure C.3: The GISAXS scattering plot of the PbS_nBDT assemblies show an amorphous powder scattering pattern characteristic of a glassy NQD assembly without spatial coherence.

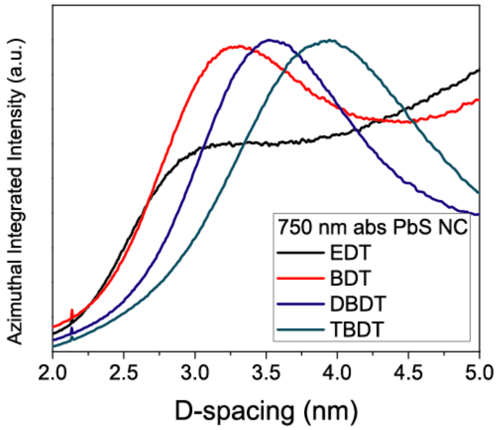

Figure C.4: Azimuthally integrated GISAXS intensity profiles of the NQD assemblies. The data shows a trend of longer inter-NQD distance with NQD assemblies treated with longer bi-linker molecule. Each additional benzene ring in the chain of bi-linker molecule results in ~0.3 nm larger average inter-nanocrystal distance.

C.8 Smaller amount of red-shift in bigger PbS NQDs

Red-shift in films prepared with bigger NQDs (6.5 nm diameter) than the NQDs discussed in the manuscript were measured to study the effect of NQD size on red-shift and inter-NQD electronic coupling. Consistent with previous observations [7, 8], a smaller amount of red-shift (20 meV) due to EDT treatment was observed with 6.5 nm PbS NQDs.

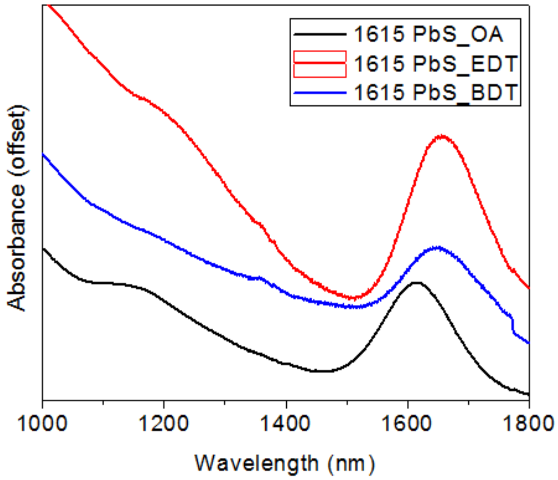

Figure C.5: Absorbance spectra of 6 nm PbS_OA, PbS_EDT, PbS_BDT assemblies. Compared to the 120 to 170 meV red-shift seen in smaller (2.7 nm) PbS NQD assemblies, a red-shift of only ~20 meV was observed with bigger PbS NQDs due to bi-linker treatment. Such red-shift values are consistent with values in the literature [7, 8].

C.9 Additional tPL results

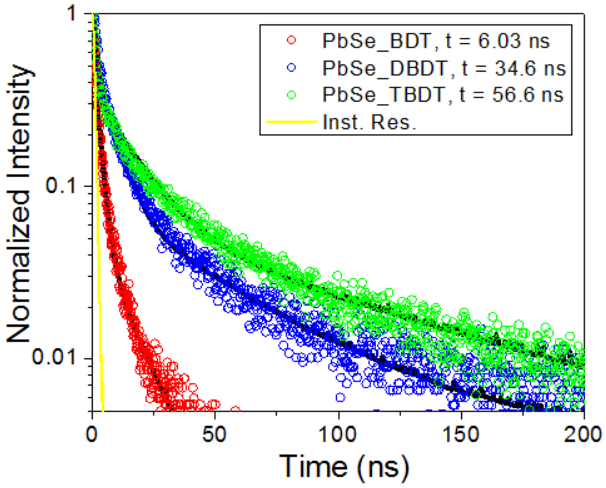

Figure C.6: Transient PL data from PbSe_nBDT samples. Similar to PbS_nBDT samples (Figure 5.1b) a trend of longer exciton lifetime with larger inter-NQD separation distance is seen.

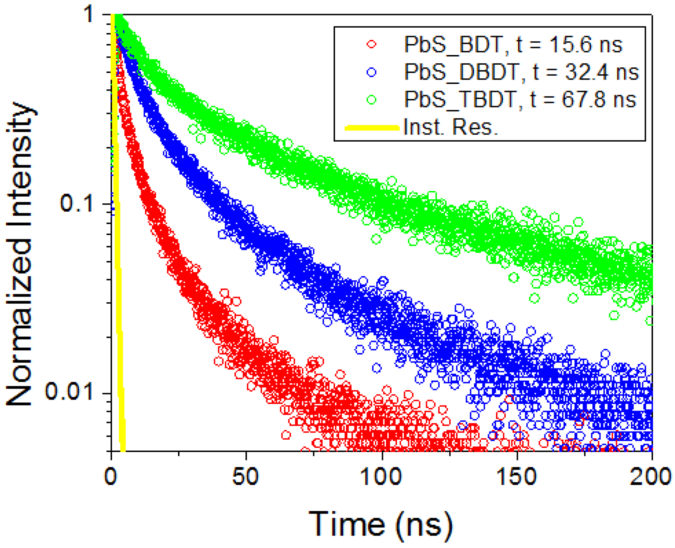

Figure C.7: Transient PL measurements of PbS_nBDT probed at the high wavelength tail of PL peak (1060 nm). No rise time in any of the PbS_nBDT samples indicate absence of resonant energy transfer.

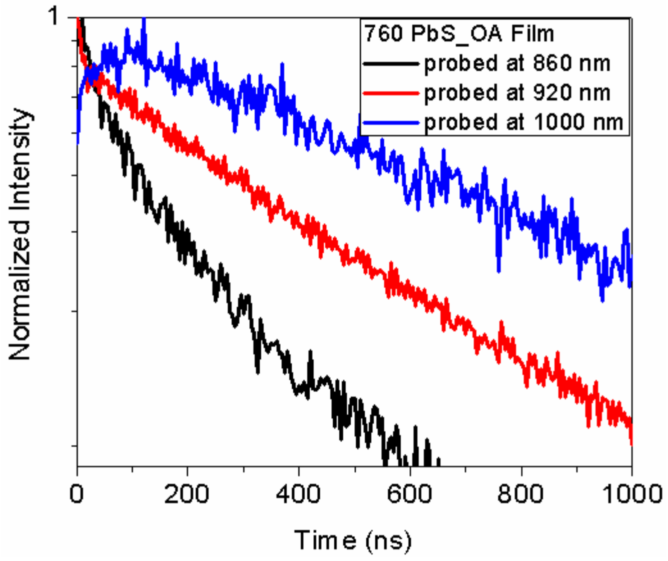

Figure C.8: Transient PL measurements of PbS_OA probed at the high wavelength tail of PL peak (1000 nm). Consistent with previous work by Clark et al. [9], a finite rise time was observed from the PbS_OA film when probed in the higher wavelength tail of the emission spectrum, indicating occurrence of Förster resonant energy transfer.

C.10 Comparison of exciton lifetimes of PbS_ethanethiol in colloidal solution and in close-packed assembly form

Following procedure reported previously [10], as-synthesized PbS NQDs dispersed in toluene were treated with ethanethiol to replace the long surface-capping oleic acid molecules while still maintaining a stable colloidal solution. The treated NQDs were precipitated, centrifuged, and redispersed in chloroform to remove displaced oleic acid molecules. Some of the solution was then drop cast on glass slides to form close-packed NQD assemblies and sealed with another glass slide and epoxy inside an N_2 atmosphere glovebox. Both PbS_ethanethiol colloidal solution sample and close packed array film sample were characterized with absorbance, time integrated PL, and time resolved PL.

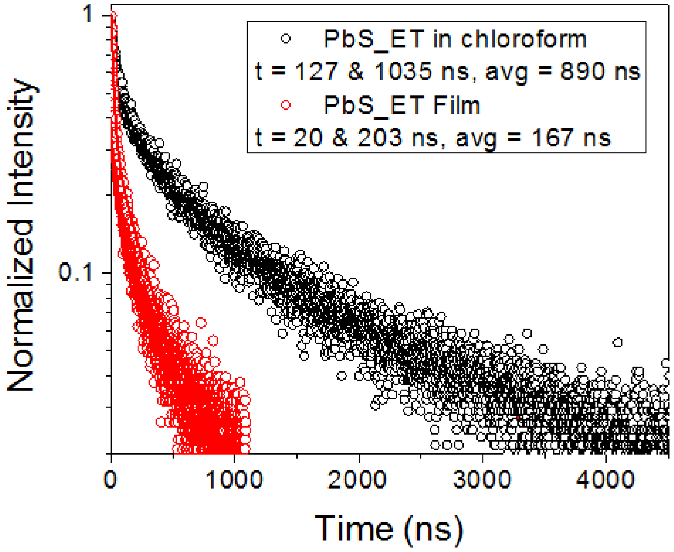

Figure C.9: Comparison of tPL data from PbS_ethanethiol in colloidal solution form and close packed assembly form. The long exciton lifetime of PbS_ethanethiol in colloidal solution form indicates that surface ligands with thiol functional groups do not quench excitons significantly. The drastic lifetime quenching observed in close-packed assembly form, still with same ligand, indicates that the proximity of NQDs is the cause of the lifetime quenching.

C.11 Long (~ 700 ns) lifetime from 4-chlorobenzenethiol treated PbS NQDs in colloidal solution form

To attach 4-chlorobenzenethiol (CBT) to PbS NQDs, 50 µL of 0.05 mM CBT solution in tetrachloroethylene (TCE) was added to 0.5 mL of 1 mg/mL PbS_OA solution in TCE. Some aggregation was observed upon adding CBT molecules and the CBT-treated NQDs could not be readily washed and redispersed. Nonetheless, time resolved PL measurements were performed on a PbS_CBT solution in TCE without any cleaning. Similar to the lifetime from PbS_ET NQDs discussed above, PbS_CBT NQDs give a long lifetime of 680 ns indicating that there is no charge transfer to the surface benzenethiol ligands on the time scale of few nanoseconds.

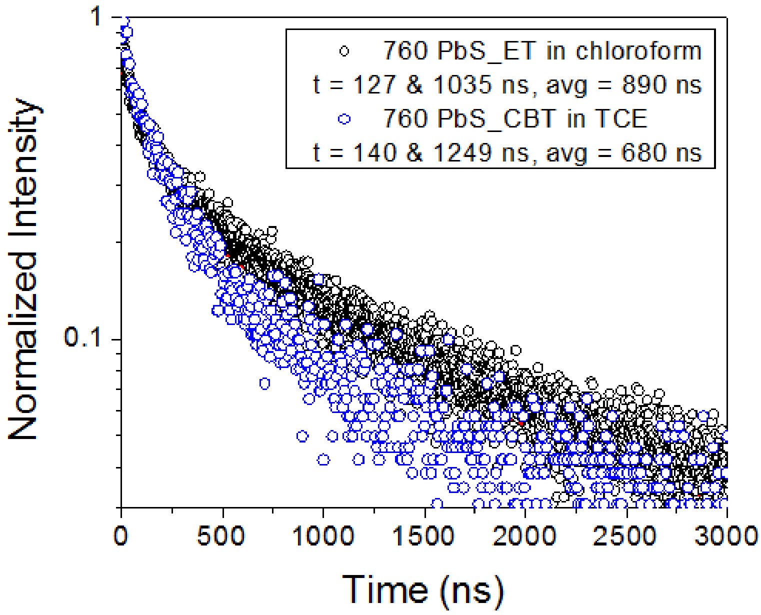

Figure C.10: Long (~ 700 ns) lifetime from 4-chlorobenzenethiol treated PbS NQDs in colloidal solution form. The Long exciton lifetime from PbS_chlorobenzenethiol in colloidal solution form indicates that benzenethiol surface ligands do not quench excitons significantly.

C.12 Details of EFM measurements

Figure C.11: Schematic of interdigitated gold electrode. The channels were 20 microns long and 5 microns wide. The thickness of the gold electrode was 40 nm.

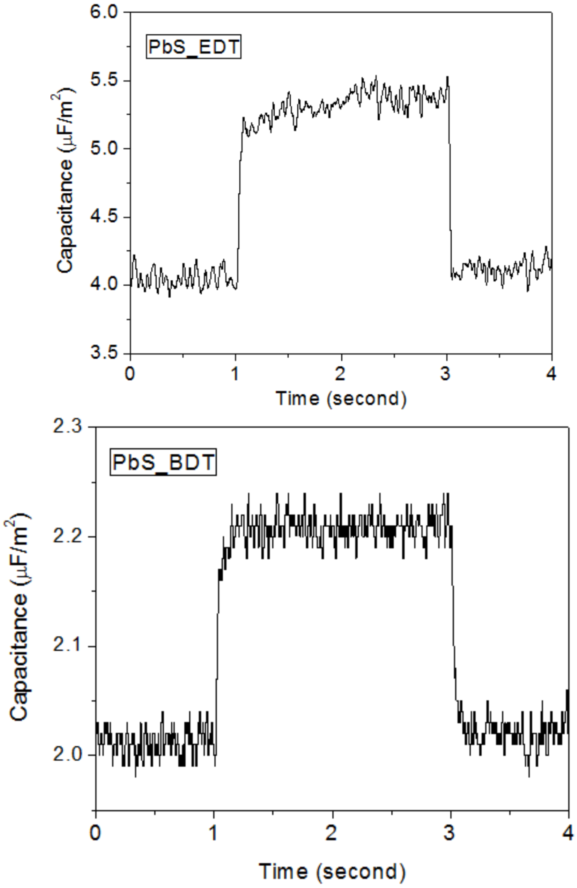

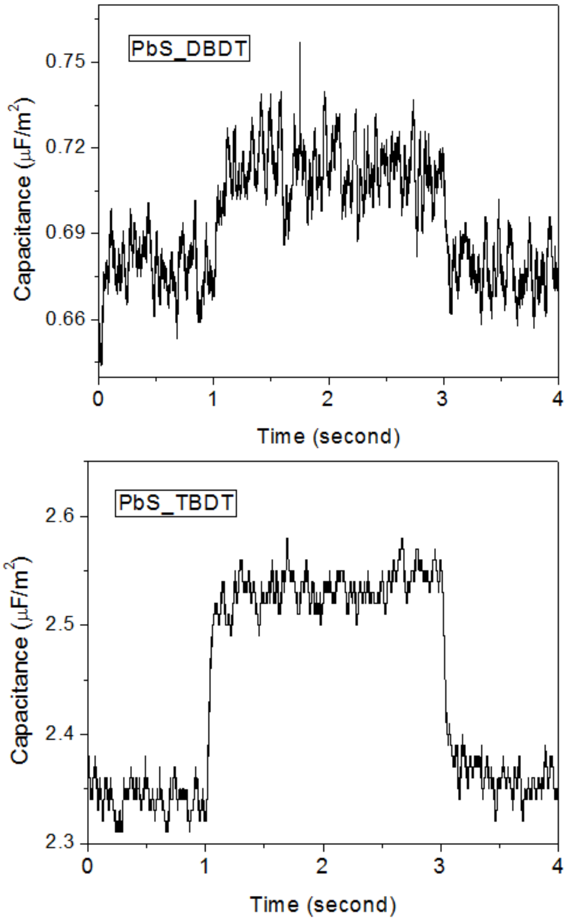

Figure C.12: PbS_nBDT film shows rapid increase in capacitance upon light illumination indicating photo-induced increase in free carrier density (light turned on at 1 second and off at 3 second for all samples). This result complements the optically observed exciton lifetime quenching shown in Figure 5.2 and serves as a direct evidence of dissociation of photogenerated excitons into free carriers in close packed NQD assembly *without* any heterojunction or external bias.

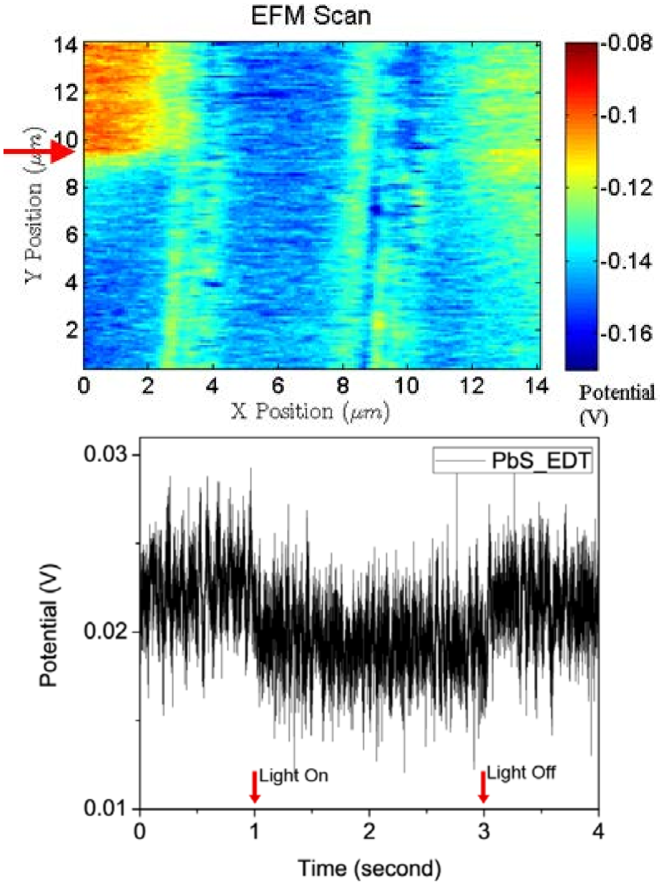

Figure C.13: EFM Potential map across the the 5 μm channel between gold electrode with PbS_EDT film (above) and a single point scan of potential response under illumination (below). The potential map was raster-scanned left to right, top to bottom. The red arrow indicates the point in the scan when sample was illuminated. No obvious trapping was observed, neither in the dark nor during illumination.

BIBLIOGRAPHY

[1] J. J. Choi, J. Luria, B.-R. Hyun, A. C. Bartnik, L. Sun, Y.-F. Lim, J. A. Marohn, F. W. Wise, T. Hanrath, Nano Letters. **10**, 1805 (2010).

[2] S. M. Yazdanian, J. A. Marohn, R. F. Loring, J. Chem. Phys. **128**, 224706 (2008).

[3] A. Kikukawa, S. Hosaka, R. Imura, Appl. Phys. Lett. **66**, 3510 (1995).

[4] G. W. T. M. J. Frisch, H. B. Schlegel, G. E. Scuseria, M. A. Robb, J. R. Cheeseman, J. A. Montgomery Jr., T. Vreven, K. N. Kudin, J. C. Burant, J. M. Millam, S. S. Iyengar, J. Tomasi, V. Barone, B. Mennucci, M. Cossi, G. Scalmani, N. Rega, G.A.Petersson, H. Nakatsuji, M.Hada, M. Ehara, K. Toyota, R.Fukuda, J. Hasegawa, M. Ishida, T. Nakajima, Y. Honda, R. O. Kitao, H. Nakai, M. Klene, X. Li, J.E. Knox, H.P. Hratchian,J.B. Cross, C. Adamo, Jaramillo, Gomperts, R. E. Stratmann, O. Yazyev, A. J. Austin, R. Cammi, C. Pomelli, J. W. Ochterski, P. Y. Ayala, K. Morokuma, G. A. Voth, P. Salvador, J. J. Dannenberg, V.G. Zakrzewski, S. Dapprich, A. D. Daniels, M. C. Strain, O. Farkas, D. K. Malick, A. D. Rabuck, K. Raghavachari, J. B. Foresman, J. V. Ortiz, Q. Cui, A. G. Baboul, S. Clifford, J. Cioslowski, B. B. Stefanov, G. Liu, A. Liashenko, P. Piskorz, I. Komaromi, R. L. Martin, D. J. Fox, T. Keith, M. A. Al-Laham, C. Y. Peng, A. Nanayakkara, M. Challacombe, P. M. W. Gill, B. Johnson, W. Chen, M. W. Wong, C. Gonzalez, and J. A. Pople, Gaussian 03, Revision D.01, Gaussian Inc., Pittsburgh, PA (2003).

[5] A. D. Becke, J. Chem. Phys. **98**, 5648 (1993).

[6] C. Lee, W. Yang, R. G. Parr, Phys. Rev. B. **37**, 785 (1988).

[7] M. C. Beard, A. G. Midgett, M. Law, O. E. Semonin, R. J. Ellingson, A. J. Nozik, Nano Lett. **9**, 836 (2009).

[8] J. M. Luther, M. Law, Q. Song, C. L. Perkins, M. C. Beard, A. J. Nozik, ACS Nano. **2**, 271 (2008).

[9] S. W. Clark, J. M. Harbold, F. W. Wise, J. Phys. Chem. C. **111**, 7302 (2007).

[10] S. Hinds, L. Levina, E. J. D. Klem, G. Konstantatos, V. Sukhovatkin, E. H. Sargent, Adv. Mater. **20**, 4398 (2008).

APPENDIX D

SUPPLEMENTARY INFORMATION: NANOCRYSTAL QUANTUM DOT LIGHT-EMITTING DIODES WITH CONTROLLED INTER-DOT SPACING[1]

D.1 Metal-oxide nanoparticle synthesis

The ZnO was synthesized in ambient air using an adaptation of a previously published method [2]. 1.76 g of zinc acetate dihydrate was dissolved in 150 mL of ethanol with vigorous stirring and heated to 60 ^{o}C for 1 hour. Parafilm was used to block solvent evaporation during the heating and the entire duration of the reaction. In a separate container, 6.4 mL of a tetramethyl ammonium hydroxide (TMAH) solution (28% in MeOH) was added to 50 mL of ethanol. Over 10 minutes, the TMAH solution was slowly added to the zinc acetate solution at regular intervals. During this time the temperature of the zinc acetate solution was maintained at 60 ^{o}C with continuous stirring. Subsequently, the solution was heated at 60 ^{o}C for 30 minutes after which the heater and stirrer were removed. After cooling to room temperature, the solution was kept refrigerated at ~ 5 ^{o}C. This mother-liquor solution was stable for over ~5 months. ZnO nanoparticles were collected from the refrigerated solution immediately before device fabrication. To prepare devices, 5 mL of the solution was typically mixed with 20 mL of hexane to precipitate the ZnO particles. After centrifugation, the supernatant was removed and the white precipitate was dissolved in a 1:2 by volume

---

[1] The results presented in this chapter have been published in Ref [1].

chlorobenzene:methanol mixture.

D.2 Light-emitting diode device fabrication method

Pre-patterned indium tin oxide (ITO)-coated glass substrates (Kintec, Hong Kong) were cleaned and treated with UV-ozone for 10 minutes. PEDOT:PSS (Product No. AI4083, H.C. Starck) was filtered through a 0.45 μm PVDF syringe filter and spin-cast onto the cleaned ITO substrate at 6000 rpm for 1 minute and baked on a hot plate at 170 °C for 4 minutes. PbS quantum dots were spin-cast from a 30 mg/mL chlorobenzene solution at 1000 rpm for 30 seconds. The quantum dot film was then treated with a 1:9 (by volume) solution of MXA (X = P, H, O) in acetonitrile (for MUA solution, powder MUA were dissolved in acetonitrile at room temperature to saturation and filtered through 0.2 μm PVDF syringe filter) and rinsed with pure acetonitrile and chlorobenzene by dispensing the solution on top of the film and spin-casting at 1000 rpm for 30 seconds. The rinsing procedure was repeated six times to ensure complete removal of free ligand molecules. This protocol constituted one cycle of the quantum dot layer deposition. For all devices, three cycles of depositions were performed. After deposition of the quantum dot film, 20 mg/mL of a ZnO nanoparticle solution was spin-cast at 1000 rpm for 1 minute. Three such depositions of ZnO nanoparticles were carried out to ensure complete coverage. Following ZnO deposition, 600 Å of aluminum was deposited *via* thermal evaporation in vacuum (~10^{-6} Torr). The entire device fabrication sequence, except for the metal evaporation step, was performed in ambient air. Each 25 mm x 25 mm substrate was patterned to yield 6 devices, each with an area of 0.03 cm^2.

D.3 Device characterization method

Current–voltage characteristics were recorded using a computer-controlled Keithley 236 source measurement unit. To calculate the EQEs, the electroluminescence from the front face of the device was detected using a calibrated Newport 918D-IR-OD3 germanium photodetector at the same time that the J–V characteristics were measured. Lambertian emission is assumed. The correction factor was calculated according to the detector position relative to the LED and the size of the active area of the detector (solid angle subtended by the detector). As verification, we used a NIST-traceable integrating sphere to measure the electroluminescence power from a quantum-dot LED that emits near 900 nm. We found the electroluminescence power obtained by each method is the same.

Electroluminescence spectra were measured with a Princeton Instruments SP2300 monochromator and IR detectors (including an IR Femtowatt photoreceiver, New Focus 2153, and a TE-cooled InGaAs detector from Judson Technologies) with bias applied to the device using a SourceMeter instrument (Keithley 2400). Photoluminescence spectra were measured in the same experimental setup; a green laser (wavelength 532 nm, µFlare OEM laser system, Lumanova GmbH) was used as the exciting source instead of applying a bias on the device.

The EQE was calculated by dividing the number of emitted photons (calculated from electroluminescence power and wavelength) by the number of injected electron-hole pairs (calculated from the current). The IQE is calculated through relation [3] IQE = 2 n^2 EQE, where n is the refractive index of the materials between the emitters and air. We chose the refractive index of glass (1.45) for n since glass comprises the largest volume of a quantum-dot LED. Thus, the conversion factor from EQE to IQE is calculated to be 4. Alternatively, we estimate the conversion factor to be in the range 3-6 by following Reference 3, where the quantum-dot LEDs have the same structure at the light exit side: PEDOD:PSS/ITO/glass. This estimate takes into account the effects of the PEDOT:PSS and ITO layers.

D.4 X-ray scattering characterization method

The samples for grazing incidence small angle X-ray scattering (GISAXS) measurements were prepared by spin coating PEDOT:PSS layer on top of cleaned silicon wafer at 6000 rpm for 1 minute. After baking the PEDOT:PSS film at 170 ^{o}C for 4 minutes, quantum dot films with variable length linkers were deposited in identical manner as the LED device film preparation. The GISAXS measurements were performed on beam line D1 of the Cornell High Energy Synchrotron Source (CHESS) using monochromatic radiation of wavelength λ = 1.264 Å with a bandwidth $\Delta\lambda/\lambda$ of 1.5%. The X-ray beam was produced by a hardbent dipole magnet of the Cornell storage ring and monochromatized with Mo:B_4C synthetic multilayers with a period of 30 Å. The D1 area detector (MedOptics) is a fiber-coupled CCD camera with a pixel size of 46.9 μm by 46.9 μm and a total of 1024 × 1024 pixels with a 14-bit dynamical range per pixel. Typical read-out time per image was below 5 s. The images were dark current corrected, distortion-corrected, and flat-field corrected by the acquisition software. The sample to detector distance was 910.5 mm, as determined using a silver behenate powder standard. The incident angle of the X-ray beam was 0.25° i.e., slightly above the silicon critical angle. Typical exposure times ranged from 0.1 to 3.0 s. Scattering images were calibrated and integrated using the Fit2D software.

D.5 Additional device characterization results

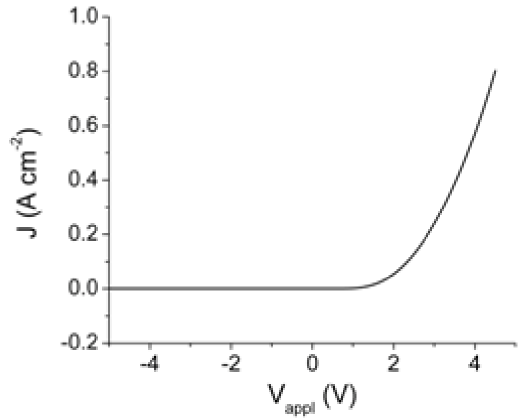

Figure D.1: Current density - applied voltage characteristic of a typical NQD-LED. The current density increase sharply when the applied voltage is larger than 1 V, but is negligible at inverse bias.

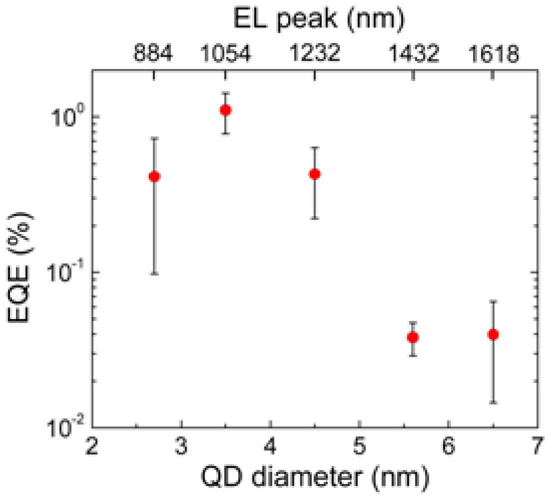

Figure D.2: EQE of the NQD-LEDs reaches the maximum when the diameter of the NQD is 3.5 nm. All the NQDs are capped by MOA linkers. The error bars indicate the EQE fluctuation in a broad range of bias (0 ~ 11 V), and from diode to diode.

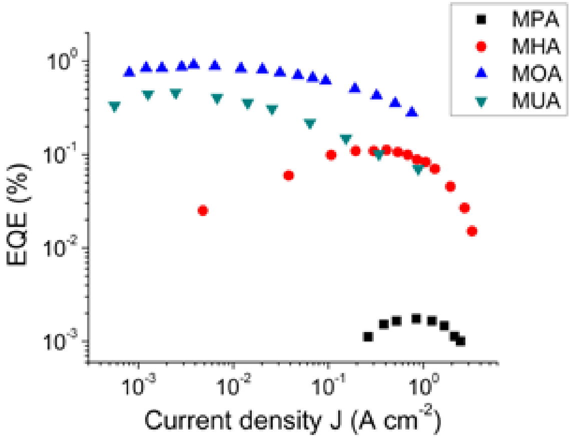

Figure D.3: The EQE for each device increases slightly, and then decreases with current density. It reaches to a maximum at certain current density which depends on the linker molecules (MPA, MHA, MOA and MUA).

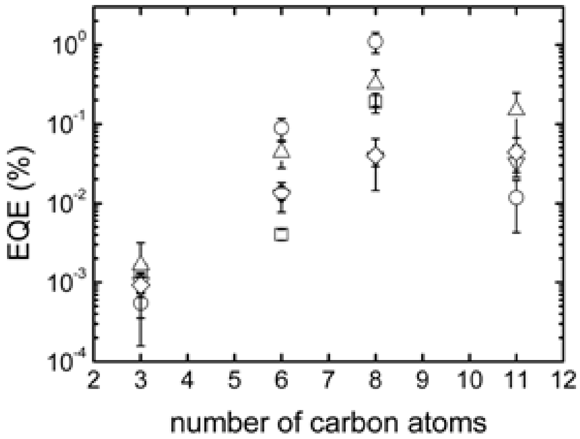

Figure D.4: Dependence of EQE from the NQD-LEDs made of 2.7 nm (squares), 3.5 nm (circles), 4.5 nm (up triangles), 5.6 nm (down triangles) and 6.5 nm (diamonds) diameter NQDs on the number of carbon atoms in the the ligands (MPA[3], MHA[6], MOA[8] and MUA[11]).

D.6 Size-dependent energy levels of the NQDs and turn-on voltages of the NQD-LEDs

The size–tunable energy levels in NQDs provide several advantageous experimental degrees of freedom. Quantum confinement can be exploited to systematically adjust the energy level offsets as well as to tune the emission wavelength. As mentioned above, the built-in potential between the ZnO and PEDOT:PSS prevents direct charge injection into the NQDs [4]. In addition, there are potential differences between the NQD layer and the carrier-transport layers, and these differences depend on the size of the NQDs. The variation of the NQD energy levels is shown in Figure 6.10A. Based on this energy level alignment, we expect the LED will not turn on until the applied bias is enough to overcome all potential barriers. The expected trend is validated in Figure S13B, which shows the relationship between NQD size and the turn-on voltage (arbitrarily defined as the voltage that produces electroluminescent power greater than 100 nW). We observe two distinct performance domains: for NQDs with diameter above 5.5 nm, the barrier for electron (hole) injection at the interface between the ZnO and the NQDs (PEDOT:PSS and NQDs) is negligible, and the turn-on voltage is mainly determined by the built-in potential (Figure 6.10B). For diameters below 5.5 nm, the turn-on voltage increases as the size of the NQDs decreases, since the barriers for electron and hole injection increase as NQD size decreases. An analogous trend between open circuit voltage and NQD diameter was observed in PbSe NQD solar cells [5].

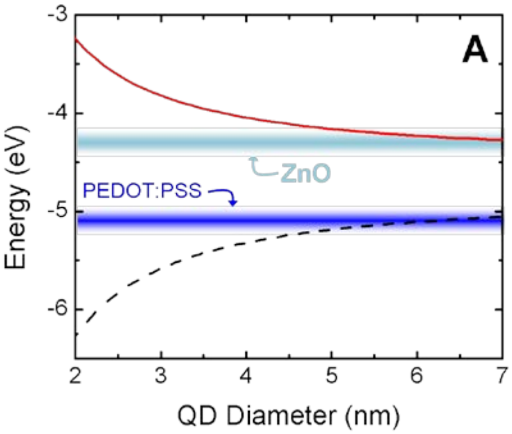

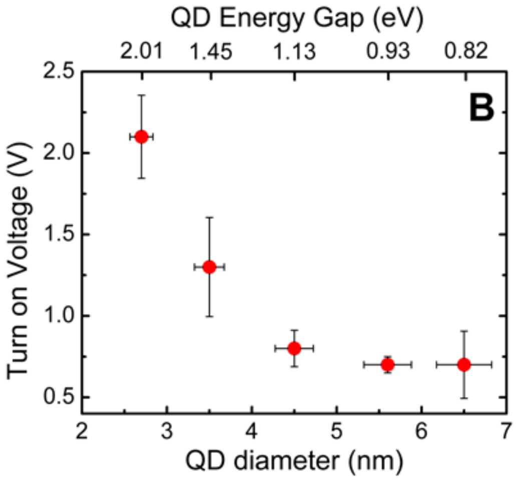

Figure D.5: (A) Calculated ionization potential (dash line) and electron affinity (solid line) levels of PbS NQDs. The fuzzy bars represent the electron affinity of ZnO nanoparticles and the ionization potential of PEDOT:PSS film. (B) Dependence of the turn-on voltage on the quantum-dot size. The NQD energy gap is calculated by subtracting the ionization potential from the electron affinity for each NQD diameter. The horizontal error bars indicate the size distributions of the NQDs, the vertical error bars indicate the fluctuation of the turn-on voltage over the different linker molecules and from diode to diode.

D.7 Inter-NQD distance measurements with GISAXS

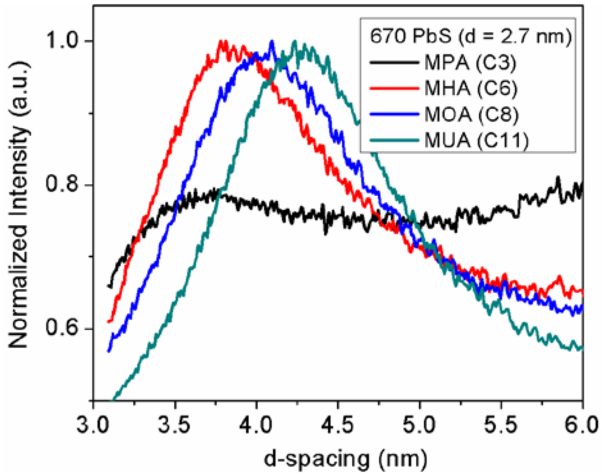

Figure D.6: D-spacing data from GISAXS measurements show a trend of longer inter-NQD spacing with longer ligands between PbS NQDs with absorption peak at 670 nm.

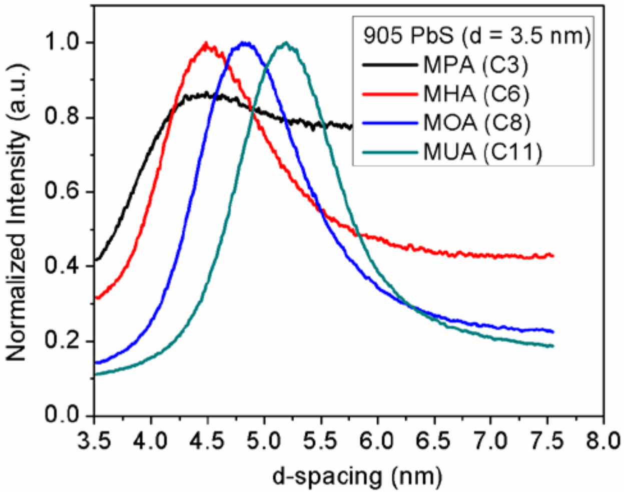

Figure D.7: D-spacing data from GISAXS measurements show a trend of longer inter-NQD spacing with longer ligands between PbS NQDs with absorption peak at 905 nm.

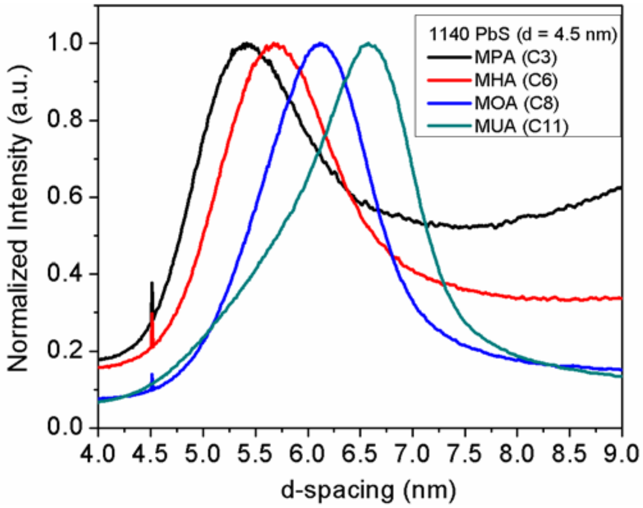

Figure D.8: D-spacing data from GISAXS measurements show a trend of longer inter-NQD spacing with longer ligands between PbS NQDs with absorption peak at 1140 nm.

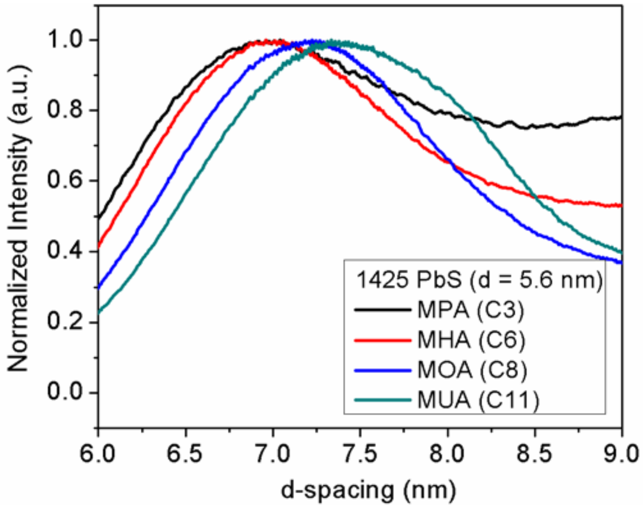

Figure D.9: D-spacing data from GISAXS measurements show a trend of longer inter-NQD spacing with longer ligands between PbS NQDs with absorption peak at 1425 nm.

D.8 Conductivity of ZnO film before and after photodoping

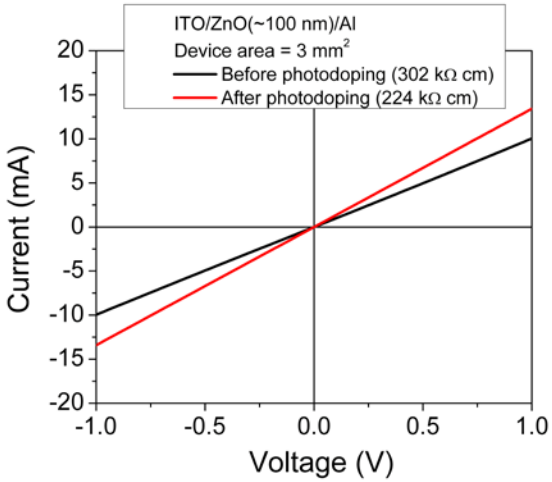

Figure D.10: The current-voltage curve shows that illumination with AM1.5 light increases the conductivity of ZnO film (about 100 nm) sandwiched in between ITO and aluminum electrode. This effect was previously attributed to increased concentration of mobile electrons due to UV photodoping [6].

D.9 Optical characterization of NQD films

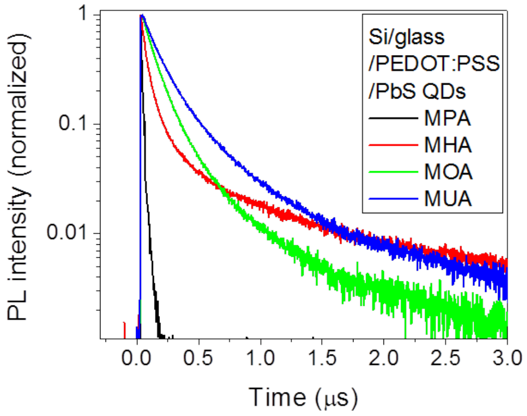

Figure D.11: Time-resolved photoluminescence from PbS NQDs films on top of PEDOT:PSS films coated on a silicon wafer. The NQDs are treated with MPA, MHA, MOA and MUA ligands respectively. The PL lifetimes (after deconvolution from the system response) defined as the times to decay to 10% of the initial are 20 ns (MPA), 168 ns (MHA), 324 ns (MOA) and 468 ns (MUA), respectively. The ratios of integrated PL (proportional to PL QE) values for the different films are MPA : MHA : MOA : MUA = 0.06 : 0.50: 0.70 : 1.

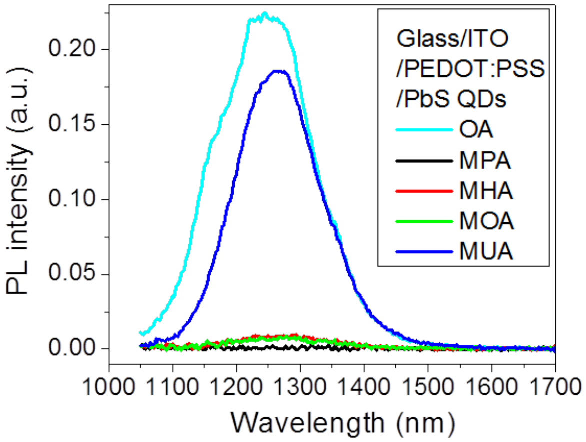

Figure D.12: PL spectra from PbS NQDs (diameter 4.5 nm) capped by OA (cyan), MPA (black), MHA (red), MOA (green) and MUA (blue) ligands. The NQDs were spin-coated on top of PEDOT:PSS/ITO/glass. Ligands exchange was followed by treating four samples with MPA, MHA, MOA and MUA solutions respectively.

BIBLIOGRAPHY

[1] L. Sun, J. J. Choi, D. Stachnik, A. C. Bartnik, B.-R. Hyun, G. G. Malliaras, T. Hanrath, F. W. Wise, Nature Nanotechnology doi:10.1038/nnano.2012.63 (2012).

[2] A. Wood, M. Giersig, M. Hilgendorff, A. Vilas-Campos, L. M. Liz-Marz 찼 n, P. Mulvaney, Aust. J. Chem. **56**, 1051 (2003).

[3] N. C. Greenham, R. H. Friend, D. D. C. Bradley, Advanced Materials. **6**, 491 (1994).

[4] G. G. Malliaras, J. R. Salem, P. J. Brock, C. Scott, Physical Review B. **58**, R13411 (1998).

[5] J. J. Choi, Y.-F. Lim, M. B. Santiago-Berrios, M. Oh, B.-R. Hyun, L. Sun, A. C. Bartnik, A. Goedhart, G. G. Malliaras, H. c. D. Abruna, F. W. Wise, T. Hanrath, Nano Lett. **9**, 3749 (2009).

[6] G. Lakhwani, R. F. H. Roijmans, A. J. Kronemeijer, J. Gilot, R. A. J. Janssen, S. C. J. Meskers, The Journal of Physical Chemistry C. **114**, 14804 (2010).

APPENDIX E

SUPPLEMENTARY INFORMATION: CONTROLLING NANOCRYSTAL QUANTUM DOT SUPERLATTICE SYMMETRY THROUGH SURFACE LIGAND INTERACTIONS[1]

E.1 NQD synthesis method

The PbS synthesis was adopted from the work by Hines and Scholes [2]. PbO (1 mmol) and oleic acid (25 mmol) were dissolved in approximately 2 mL ODE to yield a solution with a total volume of 10 mL. The solution was then degassed by heating to 150°C for 1 hour under flowing nitrogen. In a glovebox, 0.6 mol of bis(trimethylsilyl)sulfide (TMS) was dissolved in 6 mL of ODE and stirred thoroughly. 5 mL of the TMS solution was rapidly injected into the vigorously stirred, hot lead oleate solution. PbS NQDs formed immediately after injection and, after 1 minute of reaction at 150°C, the reaction solution was cooled to room temperature and collected. Following the synthesis the NQDs were washed several times by sequential precipitation with ethanol and redisperson in anhydrous hexane.

E.2 NQD superlattice formation method

---

[1] The results presented in this chapter have been published in Ref [1].

Silicon substrates were cleaned by sequential sonication in deionized water and acetone followed by ozone plasma treatment for 10 minutes. NQD films were prepared by drop-casting 50 µL of 5 mg/mL NQD suspension in hexane onto a cleaned 10 x 10 mm silicon substrate and drying the film in a controlled vapor environment. Our experimental setup was designed to minimize the impact of dynamic artifacts as far as possible.(Figure 7.5). Drop-cast films were allowed to evaporate over longer than ~10 hours in either a dry environment or in controlled saturated vapor environment.

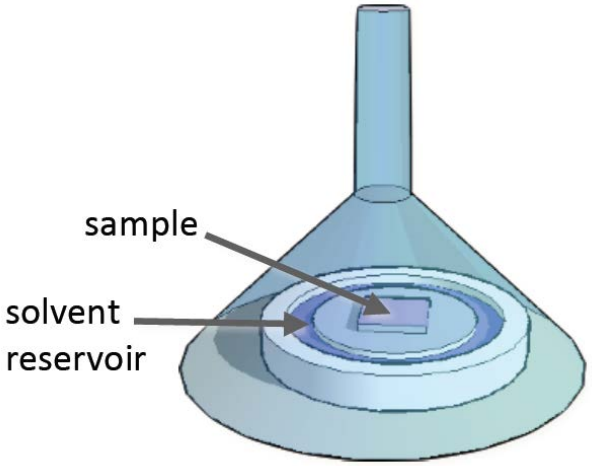

Figure E.1: X-ray scattering sample preparation experimental set-up.

E.3 X-ray scattering characterization method

Grazing incidence small angle X-ray scattering (GISAXS) measurements were performed on beam line D1 of the Cornell High Energy Synchrotron Source (CHESS) using monochromatic radiation of wavelength $\lambda = 1.211$ Å with a bandwidth $\Delta\lambda/\lambda$ of 1.5%. The X-ray beam was produced by a hardbent dipole magnet of the Cornell storage ring and monochromatized with Mo:B_4C synthetic multilayers with a period of 30 Å. The D1 area detector (MedOptics) is a fiber-coupled CCD camera with a pixel size of 46.9 μm by 46.9 μm and a total of 1024 × 1024 pixels with a 14-bit dynamical range per pixel. Typical read-out time per image was below 5 s. The images were dark current corrected, distortion-corrected, and flat-field corrected by the acquisition software. The sample to detector distance was 1015 mm, as determined using a silver behenate powder standard. The incident angle of the X-ray beam was 0.25° i.e., slightly above the silicon critical angle. Typical exposure times ranged from 0.1 to 1.0 s. Scattering images were calibrated and integrated using the Fit2D software. GISAXS diffraction peaks were indexed and fitted using in-house software [3].

E.4 TEM and FTIR characterization methods

TEM samples were prepared by drop casting diluted NQD solutions onto carbon coated 300 mesh Cu TEM grids. TEM images were taken on either an FEI Tecnai 20 (type Sphera) operated with a 200 kV LaB_6 filament or an FEI Titan equipped with a 300 kV field emission gun. Fourier transform infrared (FTIR) spectra were measured to probe the density of organic ligand bound to the NQD surface. NQD dispersions in tetrachloroethylene were put in a 3 mm path length quartz cuvette and FTIR spectra were taken with Bruker Optics - Vertex80v in vacuum mode.

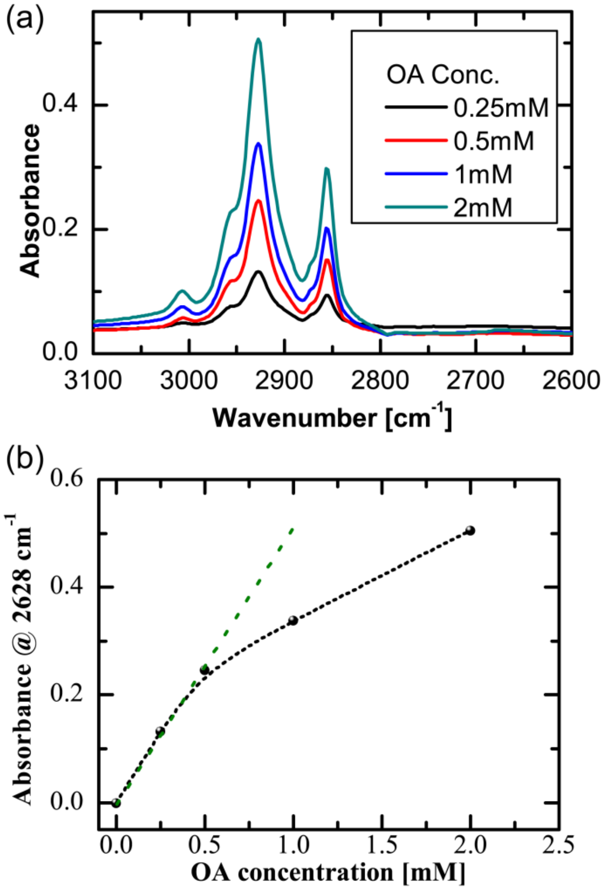

Figure E.2: FTIR calibration data with known concentration of oleic acid molecules in tetrachloroethylene.

We determined the NQD ligand coverage through direct quantitative comparison of the C-H stretching signature of the ligand and the NQD core exciton absorption. We first calibrated the OA signature by measuring the peak absorbance, Abs_{OA}, (2925 cm^{-1}) for standardized solutions of OA in tetrachloroethylene. The concentration of NQD was calculated from the NQD excitonic peak height by using Beer-Lambert law, $Abs_{NQD} = \varepsilon cl$ where size dependent extinction coefficient of PbS NQD, ε, was calculated from formula ε = $19600r^{2.32}$ reported by Cardemartiri *et al*. The cuvette path length, *l*, was 0.3 cm.

We then determined the ligand coverage per NQD from the ratio $\phi = \frac{Abs_{OA}/\varepsilon_{OA}}{Abs_{NC}/\varepsilon_{NC}}$.

The area ligand coverage was then calculated by dividing the ratio, ϕ, by the surface area of the NQD (SA_{NQD}). The calculated area ligand coverage depends on the actual shape of the NQD core. For simplicity and consistency, we compared the area ligand coverage by assuming a spherical surface area. For example, ‘aged’ PbS NQD sample had 0.36 mM of OA and 1.7 μM of NQDs. Thus it had 218 OA molecules per NQD which translates to 1.8 OA molecules per nm^2.

Error estimate of coverage was calculated by using,

$$\left(\frac{\delta\Gamma}{\Gamma}\right)^2 = \left(\frac{\delta\phi}{\phi}\right)^2 + \left(\frac{\delta SA_{NC}}{SA_{NC}}\right)^2 \qquad (E.1)$$

Beyond the ‘spherical NQD’ assumption, we can approximate the 6.7 nm NQD as a cuboctahedra.

$$A_{CO} = 6A_{100} + 8A_{111} = \left(3 + \sqrt{3}\right)(na)^2 \qquad (E.2)$$

Where A_{CO} = cuboctahera area, A_{100} = {100} facet area, A_{111} = {111} facet area , n = number of unit cells, a = unit cell parameter.For 6.5 nm PbS NQD, n = 11, a=5.9 and A_{CO}=199 nm^2 where as the area calculated with spherical assumption is 132 nm^2.

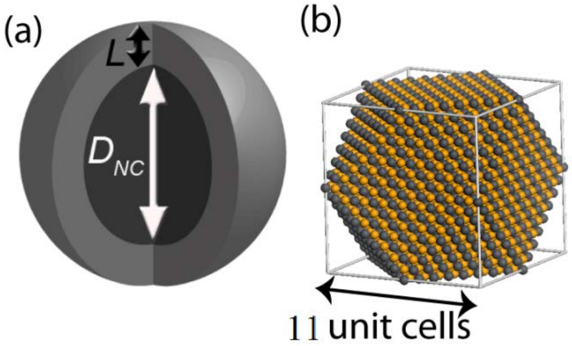

Figure E.3: (a) Spherical NQD assumption. (b) Model of cuboctahedra shape of PbS NQD. Depending on the relative sizes of the facets, the spherical assumption can give a significantly lower estimation of the real surface area.

E.5 XPS characterization method

X-ray photoelectron spectroscopy was applied to probe the nature of the inorganic NQD surface. XPS data was collected using an Omicron Sphera U5 concentric hemispherical electron energy analyzer (Omicron Nanotechnology USA, Eden Prairie, MN), operated at a constant pass energy of 50 eV. Non-monochromated Mg Kα x-rays (1253.6 eV excitation energy) were produced using an Omicron DAR 400 twin anode source operated at 300 W (15 kV anode potential x 20 mA emission current). Pb(4f) spectra were fit assuming a spin-orbit doublet separation of 4.9 eV [4-6] with a fixed ratio of 3:4 for the $4f_{5/2}$ to $4f_{7/2}$ peak area. The fwhm of all peaks was set to 1.58 eV, based on earlier measurements of a pure PbSe substrate (unpublished result). Error values given in the text refer to error originating from the fitting of XPS data only. Additional sources of error include uncertainty in the atomic sensitivity as well as photoelectron attenuation effects, which are complicated in the case of a highly 3-d film structure. These effects are expected to be similar for both films, so while although the absolute uncertainty of the atomic ratios may be high, the relative uncertainty is low, and is reflected in the error values given in the text. Atomic ratios were calculated using atomic sensitivity values published previously [7].

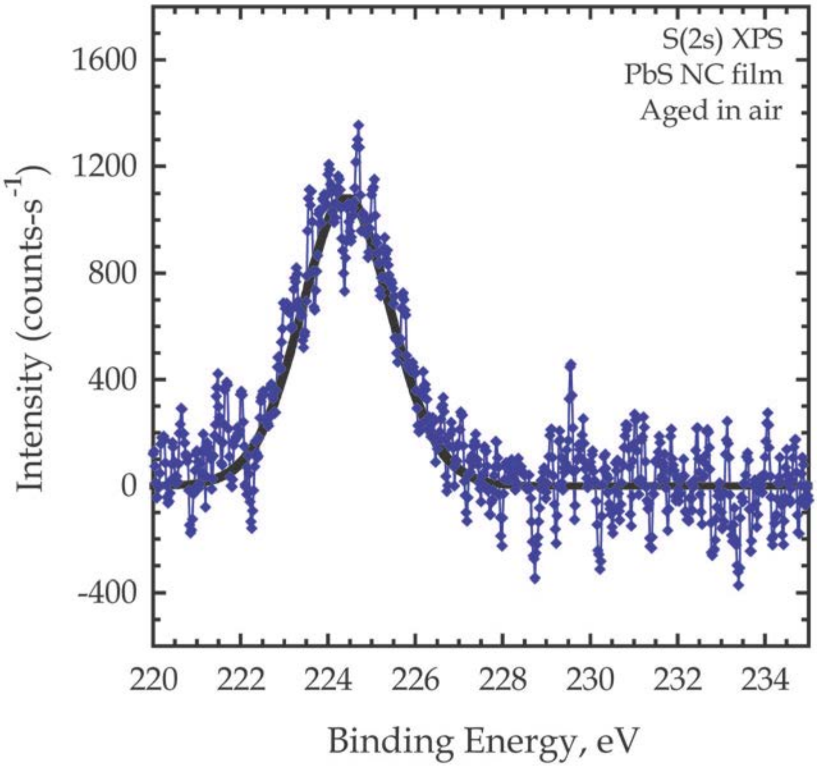

Figure E.4: XP spectrum of the S(2s) feature from a film composed of PbS NQDs aged in air. The absence of detectable peaks shifted 5-7 eV higher than the main PbS peak indicates that $PbSO_x$ species are not present at a significant level.

E.6 Computational model of ligand bound to NQD surface.

Total energy calculations were carried out using the Vienna Ab-initio Simulation Package (VASP) [8-11], within the framework of the density functional theory (DFT). The gradient-corrected PBE exchange-correlation functional was employed [12], along with the Projector Augmented Wave (PAW) method [13, 14]. The lattice constant for PbS, bonded according to the rock salt (RS) structure, was calculated as 6.00 Å, close to the experimental value of 5.95 Å [15]. The calculations were carried out using periodic boundary conditions, and the vacuum slab thickness (i.e. the distance in the c-direction between periodic images of the slab) was varied between 12 and 32 Å. K-point sampling of the Brillouin zone was performed using special k-points generated using the method of Monkhorst and Pack [16]; k-point meshes consisting of 5×10×1 and 8×8×1 grids were employed, for the orthorhombic cell containing the $\{0\ 0\ 1\}_{\mathrm{RS}}$ terminating slab and the hexagonal cell containing the $\{1\ 1\ 1\}_{\mathrm{RS}}$-terminating slab, respectively.

The wave functions were expanded on a plane-wave basis set up to kinetic energy cutoffs of 384.62 eV, and cutoff energies for the augmentation functions were set to 580.84 eV. Increasing both the wave and augmentation function cutoffs by 30% was found to alter the binding energies by ~2 meV; similarly for finer k-point meshes; binding energies did not change by more than this amount when finer k-point meshes were used. Binding energies for lead-acetate (Pb(AA)2) molecules adsorbed to a PbS surface of type {h k l}RS were calculated as

$$\mathrm{E_b} = \mathrm{E}_{\frac{\mathrm{Pb(AA)2}}{\mathrm{PbS\{hkl\}}}} - \left(\mathrm{E}_{\ \mathrm{Pb(AA)2}} + \ \mathrm{E}_{\mathrm{PbS\{hkl\}}}\right) \qquad (\mathrm{E.3})$$

where $E_{Pb(AA)2/PbS\{hkl\}}$ denotes the relaxed energy of the composite system, and $E_{Pb(AA)2}$ and $E_{PbS\{hkl\}}$ refer to the relaxed energies of the gas-phase $Pb(AA)_2$ molecule and the $PbS_{\{hkl\}}$ surface, respectively.

Modeling PbS Surfaces: Surfaces were modeled as slabs consisting of four layers; only the atoms in the topmost layer were allowed to move during the relaxation. Two PbS slabs were used for this study, the first consisting of $\{0\ 0\ 1\}_{RS}$ layers, and the second $\{1\ 1\ 1\}_{RS}$ layers; these are referred to from here on as the $\{0\ 0\ 1\}_{RS}$ slab and the $\{1\ 1\ 1\}_{RS}$ slab. The $\{0\ 0\ 1\}_{RS}$ slab was orthorhombic, with $|a| = 12.00$ Å $= 2|b|$, and contained a total of 16 cations and 16 anions. After relaxation, all the cations and anions in the $\{0\ 0\ 1\}_{RS}$-terminating surface had moved slightly closer to the remainder of the slab, such that the inter-ion distance between the topmost and second layers was ~ 2.82 Å rather than the 3.00 Å separating all other $\{0\ 0\ 1\}_{RS}$ layers. Unreconstructed $\{1\ 1\ 1\}_{RS}$ surfaces are extremely high-energy [17], as $\{1\ 1\ 1\}_{RS}$ layers each contain two flat sheets, one of cations, and the other of anions, and consequently there exists a dipole moment perpendicular to the plane. Recently, Fang *et al.* showed that the surface energy of $\{1\ 1\ 1\}_{RS}$-terminating PbSe surfaces can be reduced by more than an order of magnitude if alternating cations in the topmost layer are shifted perpendicular to the surface, so that they sit in positions directly below the layer of anions in which the opposing surface terminates [18]. As such, each surface terminates in half a monolayer of cations above a full layer of anions; this approach to the reconstruction (referred to here as the {1 1 1}-1/2-Pb reconstruction) has long been known to drastically reduce the surface energy of polar ionic crystal surfaces [19]. Rutherford backscattering experiments suggest that real PbSe $\{1\ 1\ 1\}_{RS}$ surfaces may be reconstructed along these lines; epitaxially grown PbSe was seen to terminate in a Pb layer which had an atomic density of ~40% [20]. Since the surface energy of the unreconstructed $\{1\ 1\ 1\}_{RS}$ surface is much too high to be energetically competitive with the $\{0\ 0\ 1\}_{RS}$ surface, the surfaces (both frozen and unfrozen) of the $\{1\ 1\ 1\}_{RS}$ PbS slab were modeled according to the {1 1 1}-1/2-Pb reconstruction. The $\{1\ 1\ 1\}_{RS}$ slab had hexagonal symmetry within the a-b plane, with $|a| = |b| = 12/2^{1/2}$ Å, and the slab contained a total of 16 cations and 16 anions. As a result of the reconstruction, $\{1\ 1\ 1\}_{RS}$ surfaces exhibit “trenches” in-between rows of Pb atoms. After relaxation, the Pb atoms in the terminating layer have shifted slightly closer to the remainder of the slab, such that the separation between the surface Pb atoms and the neighboring S atoms is between 2.6 and 2.8 Å.

Lead-Acetate as the Ligand: Lead-oleate ($Pb(OA)_2$) is often used as a precursor in the synthesis of lead-salt nanocrystals (NQDs); such NQDs have been observed to exhibit Pb-rich surfaces. Furthermore, Pb atoms as well as oleate ligands have been observed to detach from the NQD surface upon oxidation [21]. Since each OA molecule has a charge of -e, a ligand consisting of a Pb^{2+} cation attached to two OA molecules allows a NQD to remain charge neutral despite the presence of many oleate anions at the surface of the inorganic core. These observations suggest that we may consider PbS NQDs to consist of $Pb(OA)_2$ molecules adsorbed at the surface facets of the PbS core. To increase computational efficiency, acetate was substituted for oleate, and the binding energy of $Pb(AA)_2$ to PbS $\{0\ 0\ 1\}_{RS}$ and $\{1\ 1\ 1\}_{RS}$ surfaces was calculated. Placing one $Pb(AA)_2$ molecule above each of the $\{0\ 0\ 1\}_{RS}$ and $\{1\ 1\ 1\}_{RS}$ slabs leads to acetate coverages of 2.78 and 3.21 nm^2, respectively, which are comparable to the experimentally determined oleate coverages. For the $\{1\ 1\ 1\}_{RS}$ slab, the Pb of the $Pb(AA)_2$ was positioned inside the "trench" resulting from the surface reconstruction, while for the $\{0\ 0\ 1\}_{RS}$ slab, the Pb of the $Pb(AA)_2$ was placed above a surface S atom. In both cases a number of initial geometries for the AA atoms were attempted, in order to find the geometry with the strongest binding energy in each case.

Results: Fig. SI-5 shows the $\{0\ 0\ 1\}_{RS}$ and $\{1\ 1\ 1\}_{RS}$ surfaces, with the $Pb(AA)_2$ molecule adsorbed, after the system has been relaxed using DFT. For the $\{0\ 0\ 1\}_{RS}$ surface, the Pb atom of the $Pb(AA)_2$ was found to sit not directly above the S atom in the layer underneath, but shifted somewhat in the b direction, so that the angle made by the Pb-S bond with the vector pointing normal to the surface from the S atom was 20.2°. The height of the Pb atom above the surface was 2.97 Å, slightly larger than the average separation between the atoms in the surface layer and the atoms in the layer below of ~ 2.85 Å. The two O atoms of each acetate molecule were each separated from the Pb atom by between 2.35 and 2.50 Å, and the acetate molecules were oriented such that the angle C-Pb-C = 100.7°, where Pb is the adsorbed atom, and C refers to the carbon atom in the carboxyl group for each acetate. The C-C bonds of the acetate molecules make an angle with the vector normal to the surface of 65.2° and 64.0°; longer molecules such as oleate may be expected to twist away from the surface, such that the long carbon chains in such molecules are close to normal to the surface. Hence at high coverages, we may expect the radius of the region of the NQD outside of the inorganic core to be roughly equal to the length of the oleate molecule. The binding energy of this conformation was calculated to be -0.45 ± 0.00 eV. The Pb atom of the $Pb(AA)_2$ molecule sat in the trench of the reconstructed $\{1\ 1\ 1\}_{RS}$ surface, taking roughly the position that would be occupied by a Pb atom in the unreconstructed {1 1 1}$_{RS}$ surface, but at a distance from the remainder of the slab ~34% greater than the other Pb atoms in the terminating layer. The O atoms in each acetate were separated from the Pb atom by between 2.50 and 2.63 Å, and the angle C-Pb-C was found to be 100.0°. The C-C bonds of the acetate molecules make an angle with the vector normal to the surface of 51.9° and 58.1°. The binding energy for this conformation was calculated as -0.98 ± 0.04 eV, over twice as strong as for the {1 0 0}$_{RS}$ surface.

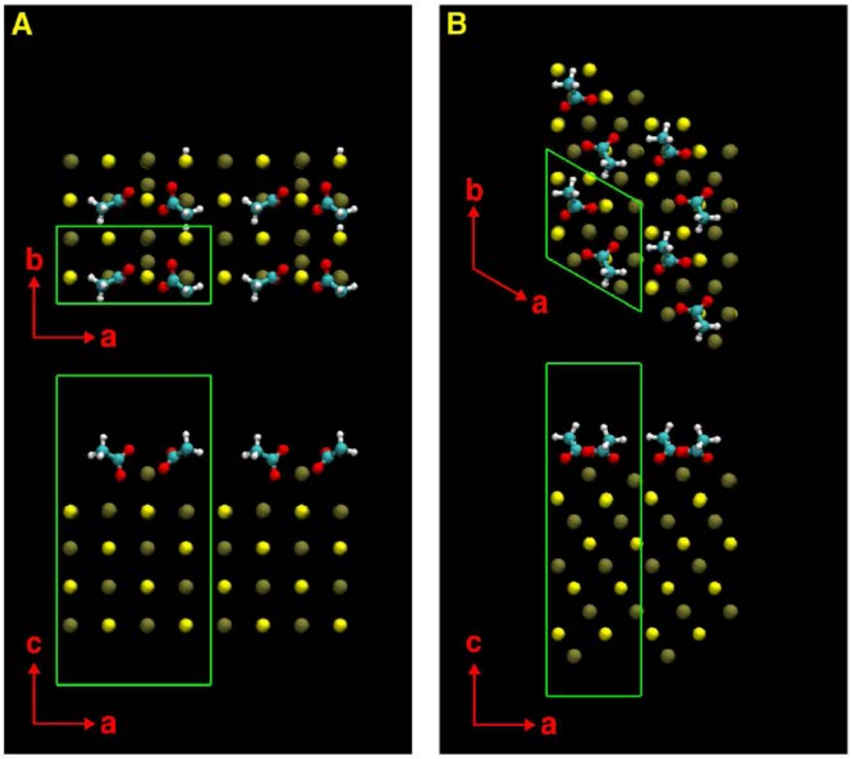

Figure E.5: DFT models for the adsorption of a Pb(AA)$_2$ molecule to the PbS {0 0 1}$_{RS}$ surface (A), and {1 1 1}$_{RS}$ surface (B). Pb atom are indicated by the green balls, S atoms by the yellow balls. The unit cells used for the calculations are outlined in green

E.7 Ligand loss due to filtering and methanol treatment

Repeated cycles of precipitating the NQD suspension, by adding anti-solvent, followed by redispersing the NQDs in fresh solvent will decrease the surface ligand coverage and ultimately destabilize the NQD suspension. Using an approach similar to the one reported by Law et al., [22] we treated PbS NQDs with methanol - 50 µL of 30 mg/mL PbS NQD solution in hexane was drop casted on top of cleaned 1 cm x 1 cm silicon substrate inside glovebox. The NQD film was then immersed in methanol. After 6 hours, the NQD film was taken out of methanol and dissolved in hexane and was put through one cycle of washing step with addition of ethanol and centrifuging inside the glovebox. FTIR measurement showed ~35% loss of surface ligands due to the methanol treatment. Interestingly, superlattice formed with those NQDs showed *fcc* symmetry despite the lower surface ligand coverage. This indicates either that the ~35% loss of surface ligands is not enough to cause anisotropic interaction between NQDs or the nature of ligand loss due to air exposure and methanol treatment are different. We believe that it is the latter case as the air exposure causes the loss of surface lead oleate [21] whereas the ligand loss due to methanol is most likely due to the nucleophilic addition of ethoxide to the carboxylate group, followed by protonation, transfer of ethoxide to the NQD surface, and loss of oleic acid. [22]

Filtration method: Ligand detachment can also be achieved through the application of shear force, e.g. by filtering cooled NQD suspension.[23] We have investigated NQD suspensions subjected to up to six filtering cycles. These NQDs also showed less pronounced ligand loss (~10% loss) than in air-aged NQD suspensions and assembled into *fcc* superlattice. PbS NQDs in 5mg/mL hexane solution, syringes and 0.45 µm pore size teflon filters were cooled down to -10 °C. The PbS NQD solution was quickly filtered through 6 teflon filters. The filtered NQD solution was then put through a washing step involving addition of 15 mL of ethanol and centrifuging to remove free floating oleic acid molecules and keep the number of washing cycle consistent with the air-aged and N_2-aged NQDs discussed in the main text.

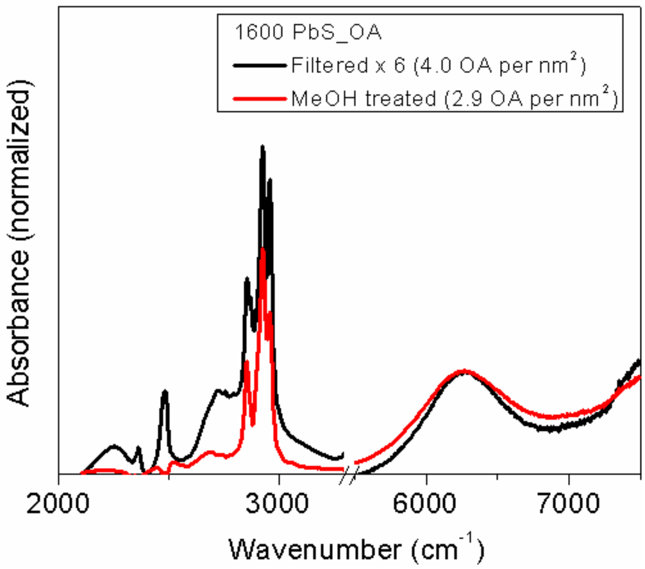

Figure E.6: FTIR characterization of surface ligand density of 'filtered' and 'methanol treated' PbS NQDs.

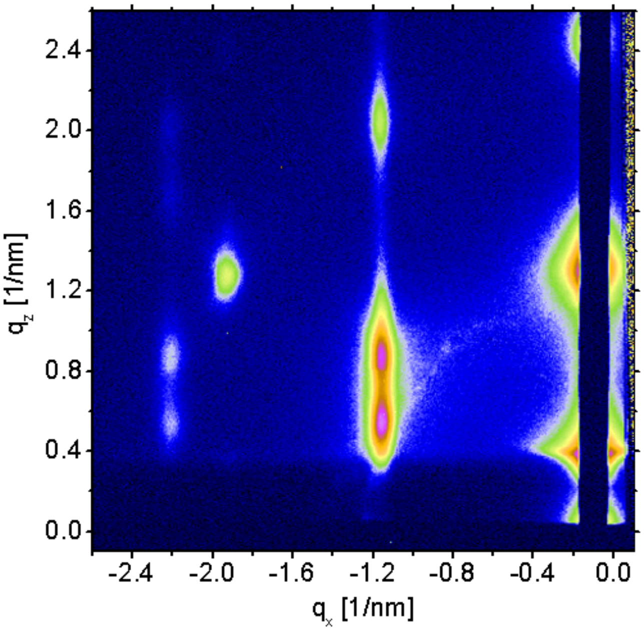

Figure E.7: GISAXS plot of ‘filtered’ NQDs shows *fcc* packing.

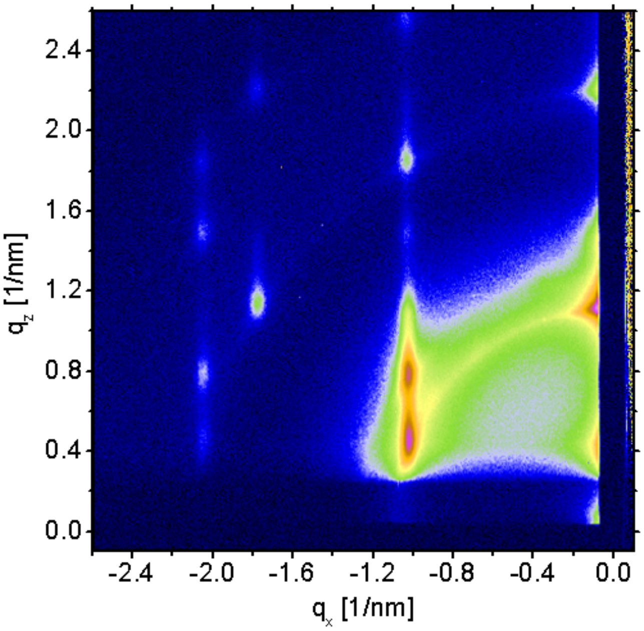

Figure E.8: GISAXS plot of ‘methanol treated’ NQDs shows *fcc* packing.

BIBLIOGRAPHY

[1] J. J. Choi, C. R. Bealing, K. Bian, K. J. Hughes, W. Zhang, D.-M. Smilgies, R. G. Hennig, J. R. Engstrom, T. Hanrath, J. Am. Chem. Soc. **133**, 3131 (2011).

[2] M. A. Hines, G. D. Scholes, Advanced Materials. **15**, 1844 (2003).

[3] D.-M. Smilgies, D. R. Blasini, Journal of Applied Crystallography. **40**, 716 (2007).

[4] J. F. McGilp, et al., Journal of Physics C: Solid State Physics. **10**, 3445 (1977).

[5] R. Nyholm, et al., Journal of Physics C: Solid State Physics. **13**, L1091 (1980).

[6] R. B. Shalvoy, G. B. Fisher, P. J. Stiles, Physical Review B. **15**, 1680 (1977).

[7] C. D. Wagner, L. E. Davis, M. V. Zeller, J. A. Taylor, R. H. Raymond, L. H. Gale, Surface and Interface Analysis. **3**, 211 (1981).

[8] G. Kresse, J. Furthmuller, Computational Materials Science. **6**, 15 (1996).

[9] G. Kresse, J. Furthmuller, Physical Review B. **54**, 11169 (1996).

[10] G. Kresse, J. Hafner, Physical Review B. **47**, 558 (1993).

[11] G. Kresse, J. Hafner, Physical Review B. **49**, 14251 (1994).

[12] J. P. Perdew, K. Burke, M. Ernzerhof, Physical Review Letters. **77**, 3865 (1996).

[13] P. E. Blochl, Physical Review B. **50**, 17953 (1994).

[14] G. Kresse, D. Joubert, Physical Review B. **59**, 1758 (1999).

[15] O. Madelung, U. R¨ossler, M. Schulz. **41C**, (1986).

[16] H. J. Monkhorst, J. D. Pack, Physical Review B. **13**, 5188 (1976).

[17] P. W. Tasker, Journal of Physics C: Solid State Physics. **12**, 4977 (1979).

[18] C. Fang, M. A. van Huis, D. l. Vanmaekelbergh, H. W. Zandbergen, ACS Nano. **4**, 211 (2009).

[19] J. T. Kummer, Y.-F. Y. Yao, Canadian Journal of Chemistry. **45**, 421 (1967).

[20] K. Kimura, K. Nakajima, Y. Fujii, M.-h. Mannami, Surface Science. **318**, 363 (1994).

[21] I. Moreels, B. Fritzinger, J. C. Martins, Z. Hens, Journal of the American Chemical Society. **130**, 15081 (2008).

[22] M. Law, J. M. Luther, Q. Song, B. K. Hughes, C. L. Perkins, A. J. Nozik, Journal of the American Chemical Society. **130**, 5974 (2008).

[23] D. Talapin, C. Murray, Science. **310**, 86 (2005).